ISSN 0352-9045

Informacije MIDEM

Journal of Microelectronics, Electronic Components and Materials
Vol. 52, No. 4(2022), December 2022

Revija za mikroelektroniko, elektronske sestavne dele in materiale
letnik 52, številka 4(2022), December 2022

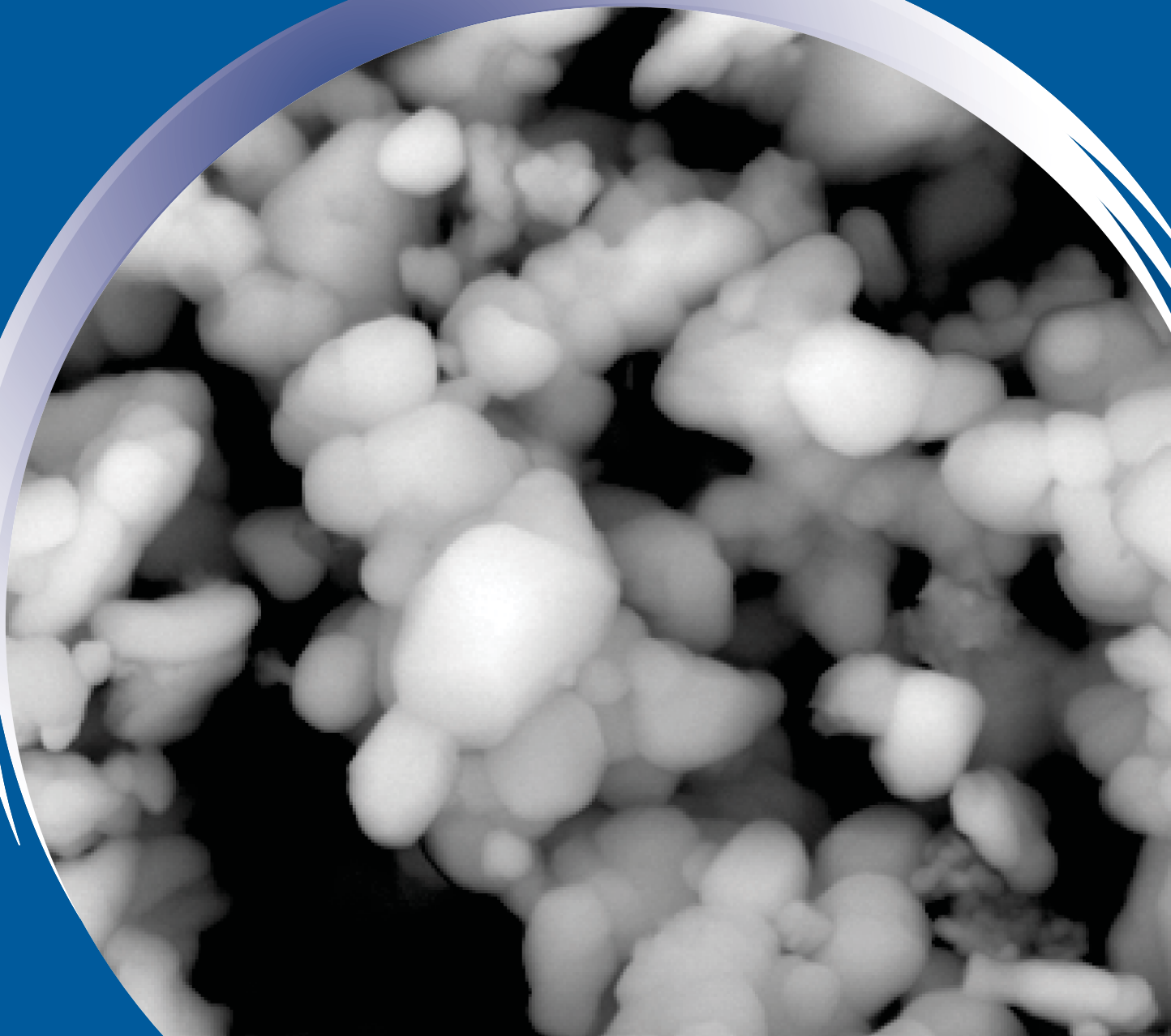

UDK 621.3:(53+54+621+66)(05)(497.1)=00 ISSN 0352-9045

Informacije MIDEM *4-2022*

Journal of Microelectronics, Electronic Components and Materials

VOLUME 52, NO. 4(184), LJUBLJANA, DECEMBER 2022 | LETNIK 52, NO. 4(184), LJUBLJANA, DECEMBER 2022

Published quarterly (March, June, September, December) by Society for Microelectronics, Electronic Components and Materials - MIDEM.

Headquarters | Naslov uredništva
Uredništvo Informacije MIDEM
MIDEM pri MIKROIKS
Stegne 11, 1521 Ljubljana, Slovenia
T. +386 (0)1 513 37 68
F. + 386 (0)1 513 37 71
E. info@midem-drustvo.si
www.midem-drustvo.si

Annual subscription rate is 160 EUR, separate issue is 40 EUR. MIDEM members and Society sponsors receive current issues for free. Scientific Council for Technical Sciences of Slovenian Research Agency has recognized Informacije MIDEM as scientific Journal for microelectronics, electronic components and materials. Publishing of the Journal is cofinanced by Slovenian Research Agency and by Society sponsors. Scientific and professional papers published in the journal are indexed and abstracted in COBISS and INSPEC databases. The Journal is indexed by ISI® for Sci Search®, Research Alert® and Material Science Citation Index™. |
Letna naročnina je 160 EUR, cena posamezne številke pa 40 EUR. Člani in sponzorji MIDEM prejemajo posamezne številke brezplačno. Znanstveni svet za tehnične vede je podal pozitivno mnenje o reviji kot znanstveno-strokovni reviji za mikroelektroniko, elektronske sestavne dele in materiale. Izdajo revije sofinancirajo ARRS in sponzorji društva. Znanstveno-strokovne prispevke objavljene v Informacijah MIDEM zajemamo v podatkovne baze COBISS in INSPEC. Prispevke iz revije zajema ISI® v naslednje svoje produkte: Sci Search®, Research Alert® in Materials Science Citation Index™.

Design | Oblikovanje: Snežana Madić Lešnik; Printed by | tisk: Biro M, Ljubljana; Circulation | Naklada: 1000 issues | izvodov; Slovenia Taxe Percue | Poštnina plačana pri pošti 1102 Ljubljana

Informacije MIDEM
Journal of Microelectronics,
Electronic Components and Materials
vol. 52, No. 4(2022)

Content | Vsebina

Original scientific papers | Izvirni znanstveni članki

Original scientific paper
https://doi.org/10.33180/InfMIDEM2022.401

Informacije MIDEM
Journal of Microelectronics,
Electronic Components and Materials
Vol. 52, No. 4(2022), 205 – 214

Electronically Tunable Multifunction Current Mode Filter Employing Grounded Capacitors

Rani Fathima[1], Srideviponmalar Perumal[2], Vadivel Muniyappan[3], Mohammad Faseehuddin[4], Worapong Tangsrirat[5]

[1]Electrical Engineering Program, EDICT Department, Bahrain Polytechnic, Bahrain.
[2]Department of Computational Intelligence, School of computing, SRM Institute of Science and Technology, India
[3]Department of Electronics and Communication, Vidya Jyoti Institute of Technology, India
[4]Department of Electronics and Telcommunication, Symbiosis Institute of Technology (SIT), Symbiosis International (Deemed) University (SIU), India
[5]Department of Instrumentation and Control Engineering, School of Engineering, King Mongkut's Institute of Technology Ladkrabang (KMITL), Bangkok, Thailand

Abstract: In this paper, a new single input multi output (SIMO) filter is presented that works in current mode (CM). The universal filter is designed using a recently proposed highly versatile active building block the extra X current conveyor transconductance amplifier (EXCCTA). The design employs two EXCCTAs, two capacitors and one resistor. The designed filter uses grounded passive elements which is advantageous for fabrication. The design can provide all the five responses i.e., high-pass (HP), band-pass (BP), low-pass (LP), all-pass (AP), and band-stop (BS) simultaneously. In addition, it provides an independent electronic tunability of angular frequency (ω) and quality factor (Q). Moreover, there is no requirement of passive component matching. The non-ideal and sensitivity analysis of the filter is done to get a measure of the effect of the process and components variation on the functioning of the filter. The simulation results are obtained using Cadence software employing 0.18 µm CMOS technology parameters from Silterra Malaysia at a supply voltage of ±1.25 V also the layout of the EXCCTA is designed. The proposed filter is validated by designing it for a frequency of 16. 07MHz. Additionally, the Spice macro model of the commercially available integrated circuits (ICs) AD844 and LM13700 are used to further test the feasibility of the proposed filter.

Keywords: current mode; filter; current conveyor; universal filter; analog

Elektronsko nastavljiv večfunkcijski filter v tokovnem načinu z ozemljenimi kondenzatorji

Izvleček: V članku je predstavljen nov enovhodni večizhodni filter (SIMO), ki deluje v tokovnem načinu (CM). Univerzalni filter je zasnovan z uporabo nedavno predlaganega zelo vsestranskega aktivnega gradnika - transkondukcijskega ojačevalnika z dodatnim tokom X (EXCCTA). Zasnova uporablja dva EXCCTA, dva kondenzatorja in en upor. Zasnovani filter uporablja ozemljene pasivne elemente, kar je ugodno za izdelavo. Zasnova lahko hkrati zagotavlja vseh pet odzivov, tj. visokoprepustni (HP), pasovni (BP), nizkoprepustni (LP), vseprepustni (AP) in pasovno zaporo (BS). Poleg tega omogoča neodvisno elektronsko nastavitev kotne frekvence (ω) in faktorja kakovosti (Q). Poleg tega ni potrebe po usklajevanju pasivnih komponent. Vplivi sprememb procesa in komponent na delovanje filtra so bili izmerjeni s pomočjo neidealne analize in analize občutljivosti filtra. Rezultati simulacije so pridobljeni s programsko opremo Cadence, pri čemer so uporabljeni parametri tehnologije CMOS 0,18 µm podjetja Silterra Malaysia pri napajalni napetosti ±1,25 V. Zasnovana je tudi postavitev EXCCTA. Predlagani filter je potrjen za frekvenco 16,07 MHz. Poleg tega sta za nadaljnje testiranje izvedljivosti predlaganega filtra uporabjena makro modela Spice komercialno dostopnih integriranih vezij (IC) AD844 in LM13700.

Ključne besede: tokovni način; filter; tokovni transporter; univerzalni filter; analogni

** Corresponding Author's e-mail: sridevip@srmist.edu.in*

How to cite:
R. Fathima et al., "Electronically Tunable Multifunction Current Mode Filter Employing Grounded Capacitors", Inf. Midem-J. Microelectron. Electron. Compon. Mater., Vol. 52, No. 4(2022), pp. 205–214

1 Introduction

From the last few decades, the designing of current mode (CM) analog filters has gained popularity among researchers due to their versatility and wide applicability. Their applications can be easily found in high-speed communication, instrumentation, sound system, control engineering, and electroacoustic etc.[1-4]. Presently universal filters designed using low voltage low power (LVLP) techniques are in demand because of the emergence of portable battery-operated devices. A universal filter circuit provides all the five filter responses, i.e. high-pass (HP), low-pass (LP), band-pass (BP), band-stop (BS), and all-pass (AP), from the same topology[3]. Furthermore, universal filters can be categorized as single input multi output (SIMO)[1, 3], multi-input multi output (MIMO)[1, 5] and multi input single output (MISO) [6, 7] filters. Second order filters have wider range of applications, so their design is an important area of research. Considering the benefits current mode (CM) circuits have in terms of higher bandwidth, good dynamic range and low power dissipation, the proposed universal filter is designed using the CM active block. Several SIMO universal filters were designed employing different CM active blocks by researchers in the literature[2, 4, 5, 8-30]. Some of these active blocks are differential voltage current conveyor (DVCC) [2, 8], current conveyor transconductance amplifier (CCTA) [9], current follower transconductance amplifier (CFTA) [11], operational floating current conveyor (OFCC) [24], third generation current conveyor (CCIII)[10], second generation current conveyor (DOCCII) [8, 9, 13], four terminal floating nullor transconductance amplifier (FTFNTA) [21], and extra x current conveyor transconductance amplifier[27], voltage differencing current conveyor. A comparative study of some exemplary designs of CM SIMO filters is done based on the following parameters (i) Number of analog building blocks required (ABBs) (ii) Number of Passive Components employed (iii) Grounded passive components used in the design (iv) the filter has low input impedance (v) all responses are available through explicit high impedance terminals (vi) responses available (vii) electronic tunability feature present (viii) independent control of quality factor and pole frequency (ix) design frequency. The Table 1 presents the comparative analysis. The available designs have some limitations in terms of cascading feature, number of passive elements, number of floating passive components, independent tunability of frequency and quality factor and simultaneous availability of all five filter responses as mentioned below.

- Low output impedance due to which cascading is not possible [9, 10, 26, 27].
- High input impedance which is undesirable for cascading [8-10, 12, 18, 14-26, 30].
- More than two active elements are employed for the design [8, 11, 12, 13, 15, 17, 19, 28, 30].
- Angular frequency and quality factor are not independently tunable [8-10, 12, 16, 17, 19, 24, 26-28].
- Fabrication is difficult due to the availability of floating passive elements [10, 12].

***Table 1**: Comparative studey of the CM SIMO universal filters*

References	(i)	(ii)	(iii)	(iv)	(v)	(vi)	(vii)	(viii)	(ix)
[8]	DVCC (3)	4R+2C	Yes	No	Yes	All five	No	No	22.5MHz
[9]	CCTA (1)	2R+2C	Yes	No	No	All five	Yes	No	1MHz
[10]	CCIII (1)	2R+2C	No	No	No	LP, BP	No	No	562.7kHz
[11]	CFTA (4)	2C	Yes	Yes	Yes	All five	Yes	Yes	153kHz
[12]	MOCCII (3)	5R+2C	No	No	Yes	All five	No	No	281.35kHz
[13]	CCII (3)	3R+2C	Yes	Yes	Yes	All five	No	Yes	1MHz
[15]	ZC-CFTA (4)	2C	Yes	Yes	Yes	All five	Yes	Yes	159kHz
[16]	ZC-CITA (2)	2C	Yes	Yes	Yes	All five	Yes	No	1.026MHz
[17]	MOCCII (3)	2R+2C	Yes	Yes	Yes	All five	No	No	1kHz
[18]	VDCC (2)	2R+2C	Yes	No	Yes	All five	Yes	Yes	1.06MHz
[19]	MOCCII (3)	2R+2C	Yes	Yes	Yes	All five	No	No	436.2kHz
[24]	MO-OFC (2)	2R+2C	Yes	No	Yes	All five	No	No	1.5MHz
[25]	DXMOCCII (2)	2R+2C	Yes	No	Yes	All five	Yes	Yes	2.65MHz
[25]	DXMOCCII (2)	1R+2C	Yes	No	Yes	All five	Yes	Yes	2.65MHz
[26]	VDCC (1)	2R+2C	Yes	No	No	All five	Yes	No	8.91MHz
[27]	EXCCTA (1)	1R+2C	Yes	Yes	No	All five	Yes	No	2.054MHz
[28]	CFTA (3)	2C	Yes	Yes	Yes	All five	Yes	No	6.4MHz
[29]	DXMOCCII (2)	3R+2C	Yes	Yes	Yes	All five	No	Yes	1.203MHz
[30]	MOCCII (3)	3R+2C	Yes	No	Yes	All five	No	Yes	100MHz
Proposed	EXCCTA (2)	1R+2C	Yes	Yes	Yes	All five	Yes	Yes	16.07MHz

- All five responses of filters are missing [10].
- Capacitor is connected to low impedance node which will degrade high frequency performance [25].

This paper describes the design of a SIMO filter by making use of two EXCCTA, two grounded capacitors and one resistor. It provides all five responses concurrently and it features independent control of angular frequency (ω) and quality factor (Q) via transconductance of the EXCCTA. Another important advantage of the filter is that the outputs are available explicitly from high impedance terminals which are essential for cascading point of view. The design is validated using Cadence design software and the simulations results are found to be in closely following the expected theoretical results.

2 Extra X Current Conveyor Transconductance Amplifier (EXCCTA)

The Extra X current conveyor transconductance amplifier (EXCCTA) is functionally an improved and more versatile version of extra x current conveyor (EXCCII) [31]. The EXCCTA[27] includes features of current and voltage followers and operational transconductance amplifier (OTA) making it more versatile. The voltage current (V-I) characteristics of the developed EXCCTA are given in Equations (1-5) and the block diagram is presented in Figure 1.

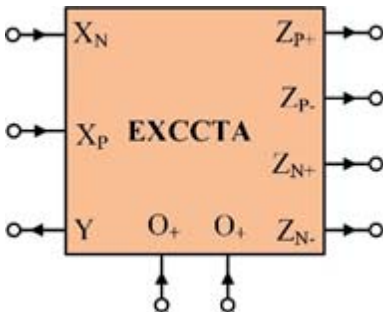

Figure 1: Block Diagram of EXCCTA

$$V_{XP} = V_{XN} = V_Y \tag{1}$$

$$I_{XP} = I_{ZP+} = -I_{ZP-} \tag{2}$$

$$I_{XN} = I_{ZN+} = -I_{ZN-} \tag{3}$$

$$I_{O+} = g_m\left(V_{ZP+}\right) \tag{4}$$

The expression for transconductance (g_m) is given in Equation 5.

$$g_m = \sqrt{\mu_n C_{OX} \frac{W}{L} I_B} \tag{5}$$

Where C_{OX} is the gate oxide capacitance, μ_n is the mobility of electrons in NMOS, g_m denotes the transconductance of OTA set via bias current I_B and W/L is the aspect ratio of the transistors.

The CMOS implementation of the EXCCTA as proposed in[27] is presented in Figure 2. The Y terminal is high impedance voltage input node and X_P & X_N low impedance voltage output/current input nodes. The O_+, Z_{P+} & Z_{N+} terminals are high impedance current output nodes. The number of current output terminals (I_{ZP+}, I_{ZP-}, I_{ZN+}, I_{ZN-}, O_+, O_-) can be increased by simply adding two MOS transistors.

3 Proposed EXCCTA based CM SIMO filter

The proposed current mode SIMO filter is shown in Figure 2. It employs two EXCCTA, one grounded resistor and two grounded capacitors which is advantageous for fabrication point of view. The filter is fully cascadable having low input impedance and high output impedance. Additionally, the pole frequency and quality factor of the filter can be independently tuned via bias current of the OTA. Another important design feature

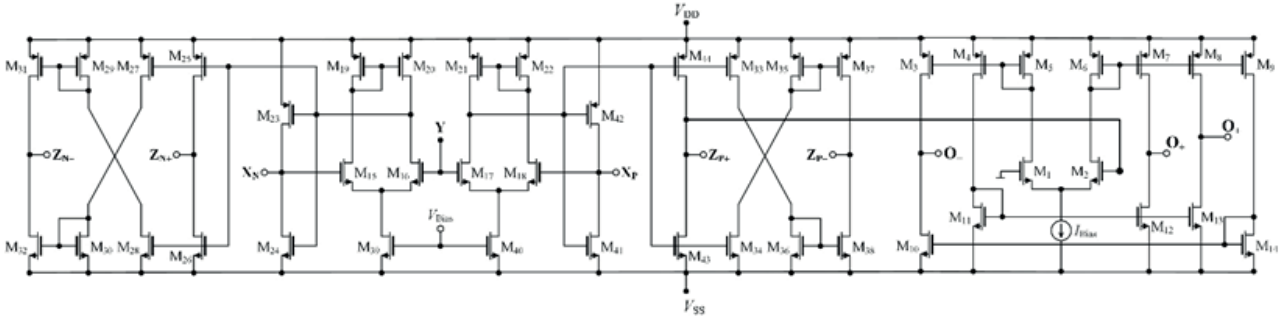

Figure 2: CMOS implementation of EXCCTA

is the use of only positive current output terminals as it avoids the use of additional MOS transistors for current reversal and improves accuracy.

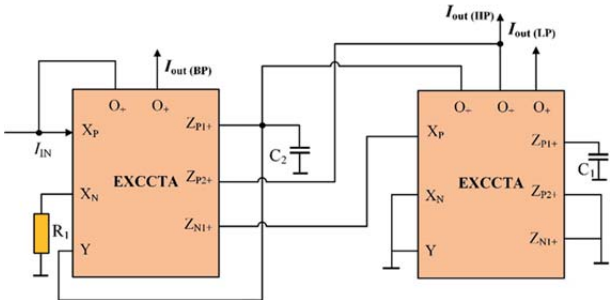

Figure 3: Proposed SIMO universal filter

The analysis of the filter circuit yields the transfer functions of all the five filter responses as given in Equations (6-10). The expression of quality factor and pole frequency of the filter are presented in Equations (11-13).

$$\frac{I_{HP}}{I_{IN}} = -\frac{S^2C_1C_2R_1}{S^2C_1C_2R_1 + SC_1R_1g_{m2} + g_{m1}} \tag{6}$$

$$\frac{I_{LP}}{I_{IN}} = -\frac{g_{m1}}{S^2C_1C_2R_1 + SC_1R_1g_{m2} + g_{m1}} \tag{7}$$

$$\frac{I_{BP}}{I_{IN}} = +\frac{SC_1R_1g_{m2}}{S^2C_1C_2R_1 + SC_1R_1g_{m2} + g_{m1}} \tag{8}$$

$$\frac{I_{NP}}{I_{IN}} = \frac{-S^2C_1C_2R_1 - g_{m1}}{S^2C_1C_2R_1 + SC_1R_1g_{m2} + g_{m1}} \tag{9}$$

$$\frac{I_{AP}}{I_{IN}} = \frac{-S^2C_1C_2R_1 - g_{m1} + SC_1R_1gm_2}{S^2C_1C_2R_1 + SC_1R_1gm_2 + g_{m1}} \tag{10}$$

$$f_o = \frac{1}{2\pi}\sqrt{\frac{g_{m1}}{C_1C_2R_1}} \tag{11}$$

$$Q = \frac{1}{g_{m2}}\sqrt{\frac{g_{m1}C_2}{C_1R_1}} \tag{12}$$

$$BW = \frac{1}{2\pi}\frac{g_{m2}}{C_2} \tag{13}$$

From equation (11) to (12), it is very clear that we can independently tune the quality factor of the filter without affecting the frequency (*f*) which means that *f* and Q are orthogonally tunable.

4 Non - ideal and sensitivity analysis

The imperfections present in the MOS transistors leads to improper transfer of current and voltage signals which leads to a shift in the V-I transfer characteristics of the EXCCTA from the ideal one. This results in the shift in the frequency and quality factor of the designed filter. The frequency dependent current, voltage and transconductance transfer gains are considered for the analysis as they are the major contributor. Considering the non-ideal gains the V-I relations of the EXCCTA will be modified to I_Y=0, $V_{XP} = \beta_p(s)V_Y$, $V_{XN} = \beta_N(s)V_Y$, $I_{ZP+} = \alpha_p(s)I_{XP}$, $I_{ZN+} = \alpha_N(s)I_{XN}$, $I_{0+} = \gamma g_m V_{ZP+}$, where $\beta_{P/N}$ is non-ideal voltage transfer gain, $\alpha_{P/N}$ is non-ideal current transfer gain and γ is non-ideal transconductance transfer gain. Ideally $\beta_{P/N} = \alpha_{P/N} = \gamma = 1$.

By considering the effect of EXCCTA non-idealities on the designed filter the expression of quality factor and angular frequency are modified as given in Equations 14-15.

$$f_o = \frac{1}{2\pi}\sqrt{\frac{\alpha_N\alpha_P\beta_P\gamma g_{m1}}{C_1C_2R_1}} \tag{14}$$

$$Q = \frac{1}{g_{m2}}\sqrt{\frac{\alpha_N\beta_P g_{m1}C_2}{\alpha_P\gamma C_1R_1}} \tag{15}$$

The active and passive sensitivities of the proposed are evaluated and presented below.

$$-S^{\omega}_{C_1} = -S^{\omega}_{C_2} = -S^{\omega}_{R_1} = S^{\omega}_{\gamma} = S^{\omega}_{\beta_P} = S^{\omega}_{\alpha_N} = S^{\omega}_{\alpha_P} = S^{\omega}_{g_1} = \frac{1}{2},$$

$$S^{Q}_{C_2} = -S^{Q}_{C_1} = -S^{Q}_{R_1} = -S^{Q}_{\gamma} = -S^{Q}_{\alpha_P} = -S^{Q}_{\gamma} = S^{Q}_{\beta_P} = S^{Q}_{g_1} = S^{Q}_{\alpha_N} = \frac{1}{2}$$

$$S^{Q}_{g_2} = -1$$

It is clear from analysis that all the sensitivities are unity or below which is the required condition. Hence the proposed filter has good performance in terms of sensitivity.

5 Parasitic study

The effect of EXCCTA parasitic elements on the performance of the filter is carried out in this section. The EXCCTA parasitic elements are shown in Figure 4. At Y terminal the parasitic resistance and capacitance appear in parallel (R_Y\\$C_Y$), same is the case with parasitic elements at Z_P, Z_N and O+ terminals where the parasitic elements appear in parallel as follows: (R_{ZP}\\$C_{ZP}$), ($R_{ZN}$\\

C_{ZN}), and (R_{O+}\\C_{O+}). The parasitic associated with low impedance X_P and X_N terminals appear as a resistors R_{XP} and R_{XN} in series with an inductor. The inductive effect is dominant at a very high frequency so it is ignored in this analysis.

Adding the EXCCTA parasitic elements in the proposed filter the node capacitance and resistance will me modified as $C_2' = (C_2 \backslash\backslash C_Y \backslash\backslash C_{ZP1+} \backslash\backslash C_{O+})$, $C_1' = (C_1 \backslash\backslash C_{ZP1+})$, $R_1' = (R_1 \backslash\backslash R_{XN})$. The modified tranfer functions of the filter including the parasitics are presented in Equations 16-22. The change in the total node capacitance and resistance majorly result in the deviation.One advantage of this topology is that the capacitors are connected with the high impedance nodes and the resistor is connected with the low impedance node. The capacitors will absorb the parasitic capacitance and the connected resistance will absorb the parasitic series resistance they by reducing the effect on the performance.

$$\frac{I_{HP}}{I_{IN}} = -\frac{S^2 R_1' C_1' C_2'}{S^2 R_1' C_1' C_2' + S R_1' C_1' g_{m2} + g_{m1}} \tag{16}$$

$$\frac{I_{LP}}{I_{IN}} = -\frac{g_{m1}}{S^2 R_1' C_1' C_2' + S R_1' C_1' g_{m2} + g_{m1}} \tag{17}$$

$$\frac{I_{BP}}{I_{IN}} = +\frac{S R_1' C_1' g_{m2}}{S^2 R_1' C_1' C_2' + S R_1' C_1' g_{m2} + g_{m1}} \tag{18}$$

$$\frac{I_{NP}}{I_{IN}} = \frac{-S^2 R_1' C_2' C_1' - g_{m1}}{S^2 R_1' C_1' C_2' + S R_1' C_1' g_{m2} + g_{m1}} \tag{19}$$

$$\frac{I_{AP}}{I_{IN}} = \frac{-S^2 R_1' C_2' C_1' - g_{m1} + S R_1' C_1' g m_2}{S^2 R_1' C_1' C_2' + S R_1' C_1' g_{m2} + g_{m1}} \tag{20}$$

$$f_o = \frac{1}{2\pi}\sqrt{\frac{g_{m1}}{R_1' C_1' C_2'}} \tag{21}$$

$$Q = \frac{1}{g_{m2}}\sqrt{\frac{g_{m1} C_2'}{R_1' C_1'}} \tag{22}$$

6 Simulation results

To validate the proposed resistor less CM SIMO filter it is designed and simulated in Cadence virtuoso design software. The EXCCTA is designed in 0.18 µm Silterra Malaysia technology at a supply voltage of ±1.25V. The width and length of the transistors used are given in

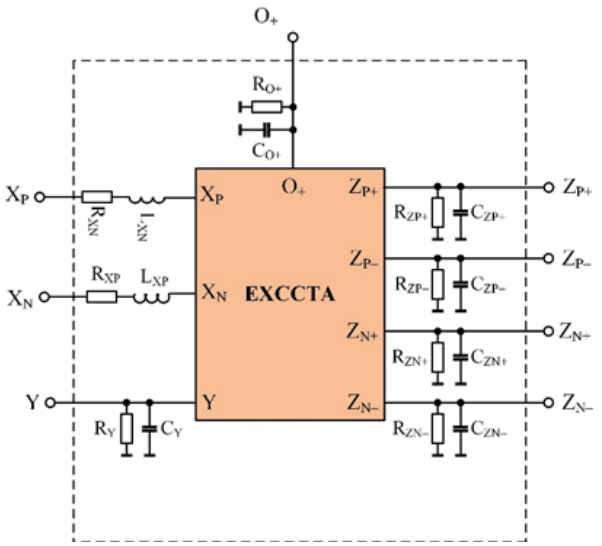

Figure 4: Non-ideal equivalent circuit model of the EXCCTA

Table 2. The transconductance of the OTA was fixed 1.02 mS by selection the bias current I_{bias} = 120 µA. The layout of the EXCCTA is presented in Fig. 5. It is drawn using the nhp and php high performance MOS transistors from the Silterra library and occupies chip area of 65*26µm^2.

Table 2: Width and Length of the MOS transistors

Transistors	Width (µm)	Length (µm)
M1-M2, M5-M6	1.8	0.36
M3, M4, M7, M8, M9	5.4	0.36
M10-M14	1.8	0.72
M15-M18	3.06	0.36
M19-M22	10	0.36
M23, M25, M27, M29, M31, M35, M37, M33, M42, M44	2.16	0.36
M24, M25, M28, M41, M43, M34	0.72	0.72
M30, M32, M36, M38	1.08	0.72

The pole frequency of the filter is fixed at 16.07 MHz and quality factor to 1.2 by setting passive component values as R_1 = 1kΩ, $C_1 = C_2$ = 10 pF and g_m = 1.02 µS. The LP, HP, BP and NP responses of the CM SIMO filter are presented in Fig. 6. The AP gain and phase response is given in Fig. 7. The simulated frequency for CM-AP is found to be 15.75 MHz leading to 2% error. The power dissipation of the filter is found to be 3.29mW.

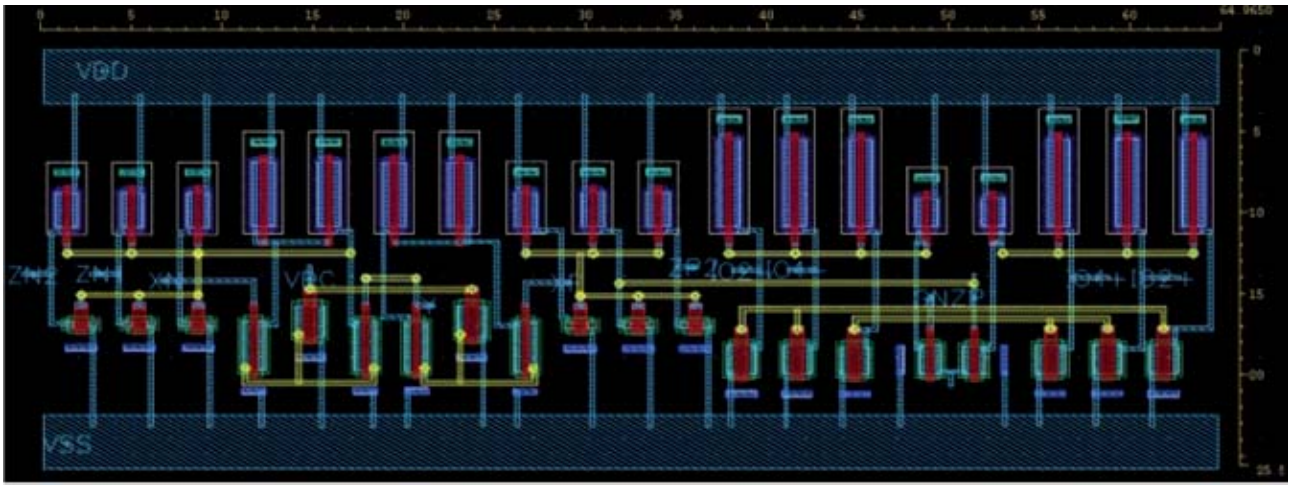

Figure 5: Layout of the EXCCTA

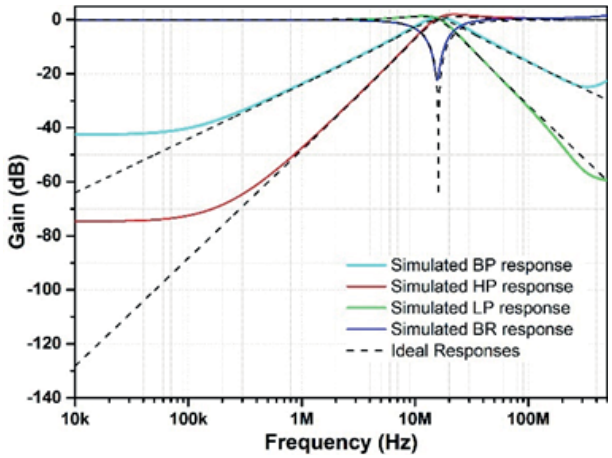

Figure 6: The ideal and simulated results of the SIMO filter

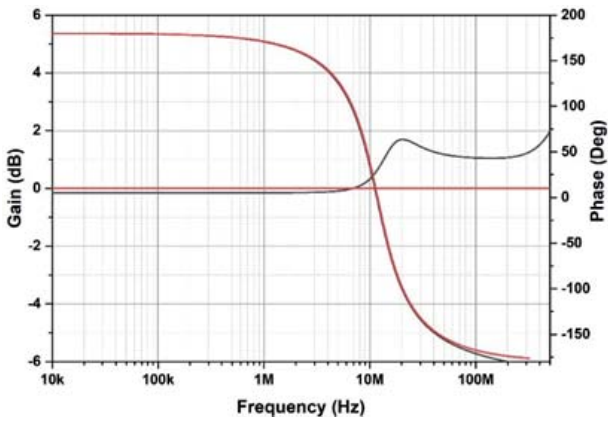

Figure 7: The AP gain and phase response of the SIMO filter

To establish the signal processing capability of the proposed filter a sine wave of frequency 16.07MHz and 100μA(p-p) amplitude is applied and the BP response of the filter is monitored as presented in Fig.8. It can be seen the filter output is accurate in terms of phase and magnitude. The Monte Carlo analysis is performed to measure the effect of device parameter variations and process spread on the performance of the filter. The Monte Carlo analysis is done for 200 runs using the mismatch models provided in the PDK for MOSFETs. As can be seen from Figure 8 the mean frequency is found to be 15.79 MHz which is close to designed frequency. Also, the frequency spread is small for majority of the samples so it can be concluded that the filter exhibits acceptable performance with minimum deviation under process variations. It can also be seen from the plot in Fig. 9 that minimum and the maximum frequency are 14.9MHz and 16.81MHz respectively. The phase plot of the all-pass response for the Monte Carlo analysis is presented in Fig. 10.

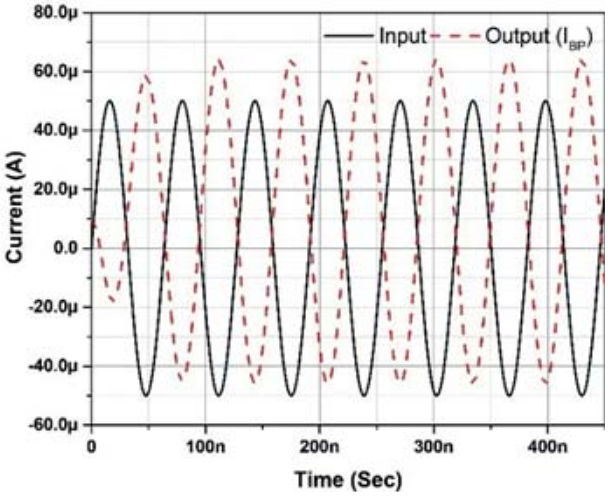

Figure 8: Time domain results for BP configuartion

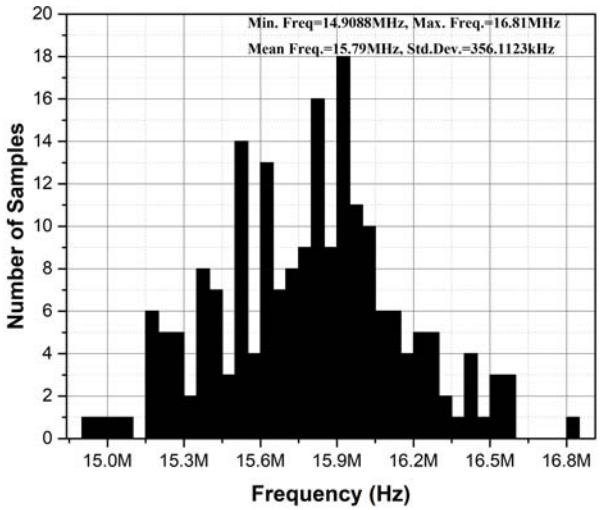

Figure 9: The Monte Carlo analysis results for AP confoguartion

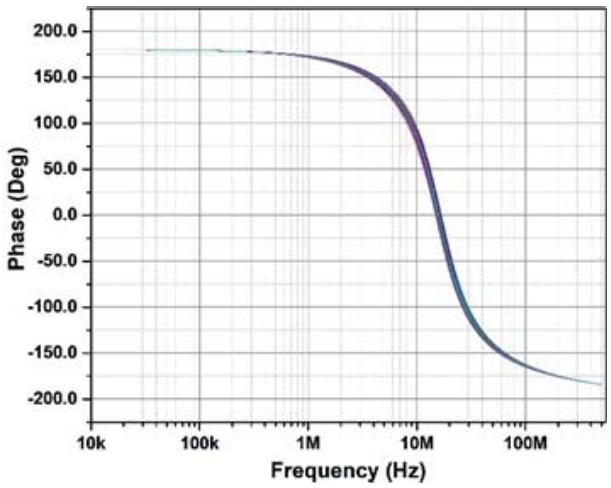

Figure 10: The Monte Carlo analysis plot of the phase response of AP configuartion

The variation of the quality factor independent of the pole frequency is examined for different values of I_{Bias2} ranging from I_{Bias2} =20μA(g_{m2} = 463μ*S*), I_{Bias2} =50μA(g_{m2} = 681μ*S*), I_{Bias2} =80μA(g_{m2} = 910μ*S*) and I_{Bias2} =120μA(g_{m2} = 1.02μ*S*) while keeping I_{Bias1} constant as presented in Fig. 11. The quality factor of the filter chages as per Equation 12 due to the change in the transcoducatnnce (g_{m2}). The effect of temperature variation on the functioning of the filter is examined by analysing the BP response under different temperature values ranging from 0° to 100°C. It can be inferred for the graph in Fig. 12(a-b) that although the filter frequency decreases with increase in temperature it is close to theoretical value within 20° to 60°C. Theoretically, the frequency of the filter should not change with temperature, but the frequency of the filter decreases due to rise in temperature because of the decrease in OTA transconductance (g_m). Two main contributing factors that influence the transconductance are the threshold voltage (V_t) and carrier mobility.The total harmonic distortion (THD) of the filter is measured for different input current amplitudes as presented in Fig. 13. The THD remains within acceptable limit of 5% for significant input current range.

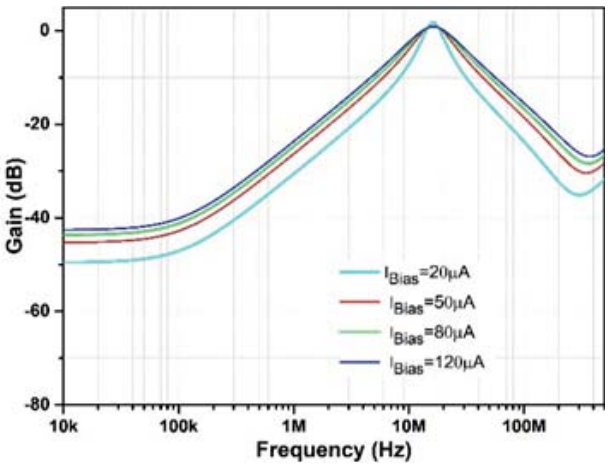

Figure 11: BP quality factor tuning

(a)

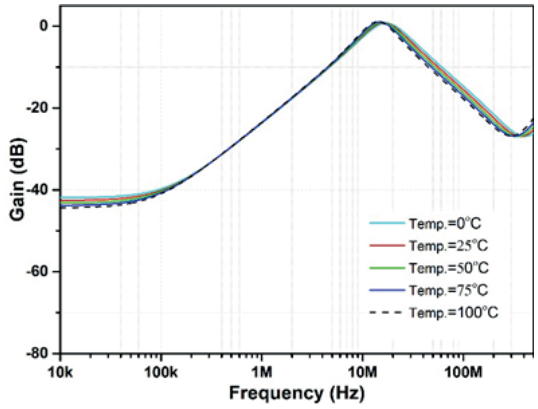

(b)

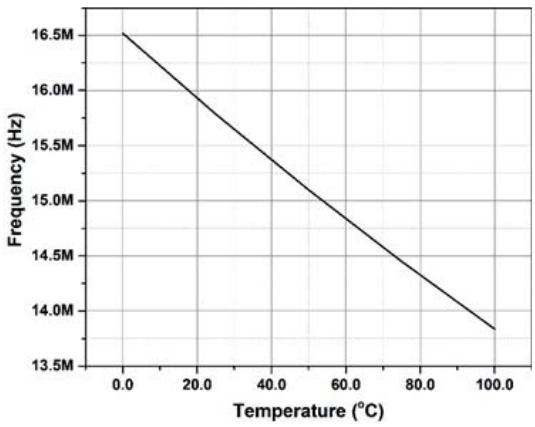

Figure 12: Effect of temperature on the filter performance (a) BP response (b) BP frequency variation

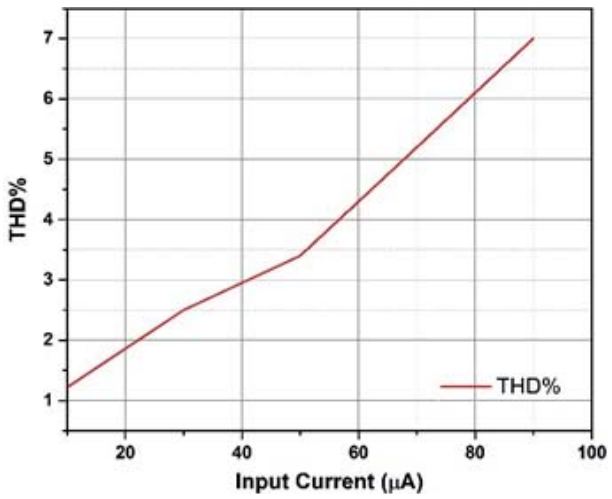

Figure 13: Variation of total harmonic distortion with applied input current

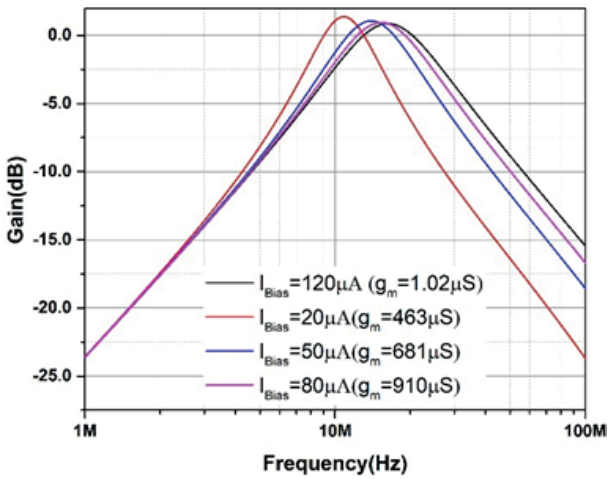

Figure 14: Variation of filter frequency with bias currents of the OTA

The frequency tunability of the filter is shown by varying the bias currents (I_{Bias1} and I_{Bias2}) of the OTAs simultaneously. It can be seen from Figure 14 that the filter frequency changes with change in the bias currentss also it is observed that there is slight change in the quality factor of filter due to change in the transconductnace (g_{m2}). The change in the quality factor can be nullified by accordingly setting the value of R_1 or setting the value of g_{m2}.

7 Implementation using commercially ICs

To further investigate the workability of the filter it is designed using commercially available ICs. The behavioural models of the current feedback operational amplifier (AD844) and OTA (LM13700) provided by the manufacturer are used in the study. The PSPICE software is used for the analysis. The authors want to mention that the IC based implementation is done for the proof of concept as the fabricated chip is not available for experimental validation. The Figure 15 presents the implementation of the filter.

The filter frequency is set at 225kHz by setting OTA transconductance at 2mS and passive component values at R_1 = 1 kΩ, $C_1 = C_2$ = 1nF. The frequency domain analysis of the filter is done as presented in Figure 16. The close relationship between the ideal and simulated results verify the feasibility of the proposed design.

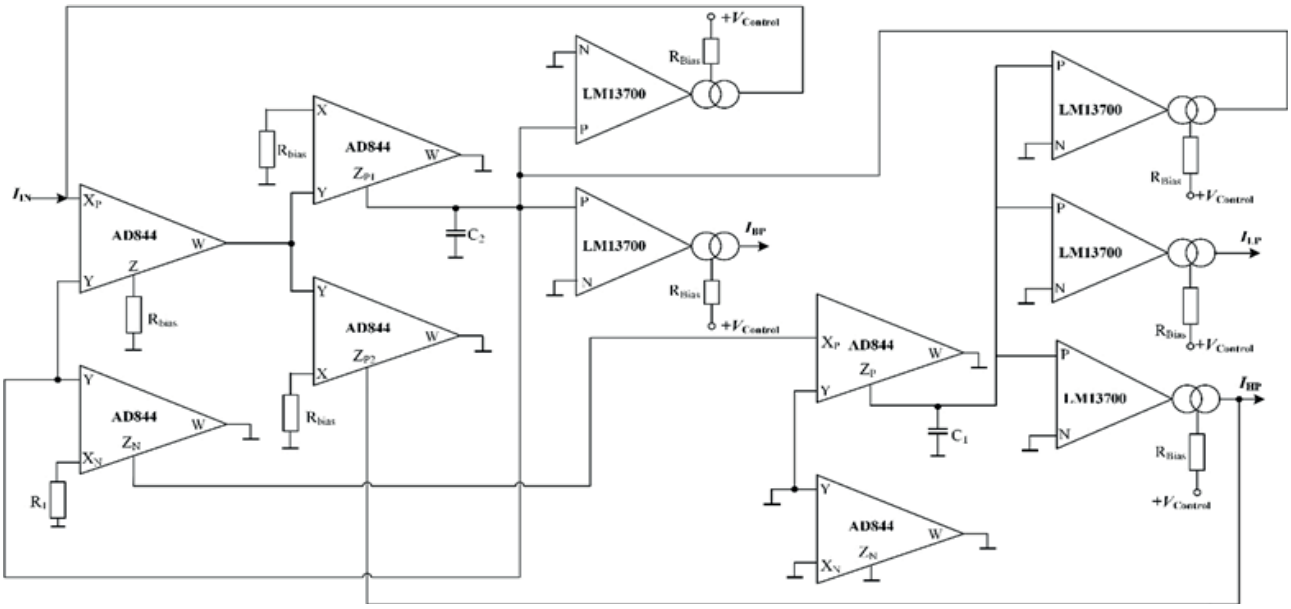

Figure 14: Implementation of the proposed filter using commercially available ICs AD844 and LM13700

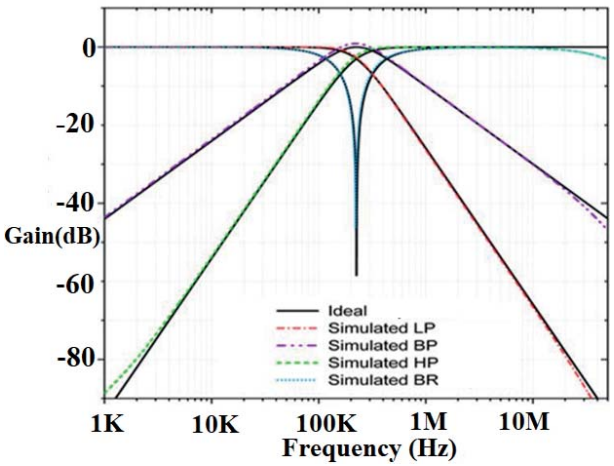

Figure 16: Frequency response of the filter obtained using AD844 and LM13700

8 Conclusion

This paper presents a new EXCCTA based electronically tunable SIMO filter. The filter employs two EXCCTA, one resistor and two grounded capacitors. Presented SIMO filter has inbuilt tunability and can realize all five filter responses simultaneously. The EXCCTA is designed in Cadence Virtuoso software and extensive simulations are carried out to examine and validate the proposed filter. The proposed filter has all the advantages mentioned in Table 1.The filter is designed for a frequency of 16.07 MHz at ±1.25 V supply. The Monte Carlo analysis shows that the frequency deviation is within acceptable limits. Furthermore, the THD is within 5% for considerable current input signal range. The simulation results are found consistent with the theoretical predictions.

9 Conflicts of interest

The authors declare no conflict of interest.

10 Acknowledgement

This work was supported by King Mongkut's Institute of Technology Ladkrabang (KMITL).

11 References

1. R. Senani, D. Bhaskar, and A. Singh, *Current conveyors: variants, applications and hardware implementations* vol. 560: Springer, 2015. https://doi.org/10.1007/978-3-319-08684-2.
2. J.-W. Horng and Z.-Y. Jhao, "Voltage-mode universal biquadratic filter using single DVCC," *International Scholarly Research Notices,* vol. 2013, 2013. https://doi.org/10.1155/2013/125746.
3. P. A. Mohan, *Current-mode VLSI analog filters: design and applications*: Springer Science & Business Media, 2003. https://doi.org/10.1007/978-1-4612-0033-8.
4. A. M. Soliman, "Current-mode universal filters using current conveyors: classification and review," *Circuits, Systems & Signal Processing,* vol. 27, pp. 405-427, 2008. https://doi.org/10.1007/s00034-008-9034-y
5. S. V. Singh, S. Maheshwari, and D. Chauhan, "Current-processing current-controlled universal biquad filter," *Radioengineering,* vol. 21, pp. 317-323, 2012. https://doi.org/10.1007/s00034-008-9034-y.
6. H.-P. Chen, "Versatile current-mode universal biquadratic filter using DO-CCIIs," *International journal of electronics,* vol. 100, pp. 1010-1031, 2013. https://doi.org/10.1080/00207217.2012.731370.
7. H. P. Chen, "Current-mode dual-output ICCII-based tunable universal biquadratic filter with low-input and high-output impedances," *International Journal of Circuit Theory and Applications,* vol. 42, pp. 376-393, 2014. https://doi.org/10.1002/cta.1858.
8. M. A. Ibrahim, S. Minaei, and H. Kuntman, "A 22.5 MHz current-mode KHN-biquad using differential voltage current conveyor and grounded passive elements," *AEU-International Journal of Electronics and Communications,* vol. 59, pp. 311-318, 2005. https://doi.org/10.1016/j.aeue.2004.11.027.
9. N. Herencsar, J. Koton, and K. Vrba, "Single CCTA-Based Universal BiquadraticFilters Employing Minimum Components," *International Journal of Computer and Electrical Engineering,* vol. 1, p. 307, 2009. https://doi.org/10.7763/IJCEE.2009.V1.48.
10. E. Yuce, B. Metin, and O. Cicekoglu, "Current-mode biquadratic filters using single CCIII and minimum number of passive elements," *Frequenz,* vol. 58, pp. 225-227, 2004. https://doi.org/10.1515/FREQ.2004.58.9-10.225.
11. W. Tangsrirat, "Single-input three-output electronically tunable universal current-mode filter using current follower transconductance amplifiers," *AEU-International Journal of Electronics and Communications,* vol. 65, pp. 783-787, 2011. https://doi.org/10.1016/j.aeue.2011.01.002.
12. J.-W. Horng, "Current-mode and transimpedance-mode universal biquadratic filter using multiple outputs CCIIs," 2010.

13. K. K. Abdalla, D. R. Bhaskar, and R. Senani, "Configuration for realising a current-mode universal filter and dual-mode quadrature single resistor controlled oscillator," *IET circuits, devices & systems,* vol. 6, pp. 159-167, 2012. https://doi.org/10.1049/iet-cds.2011.0160.
14. A. Qadir and T. Altaf, "Current mode canonic OTA-C universal filter with single input and multiple outputs," in *2010 2nd International Conference on Electronic Computer Technology*, 2010, pp. 32-34. https://doi.org/10.1109/ICECTECH.2010.5479995.
15. J. Satansup and W. Tangsrirat, "Single-input five-output electronically tunable current-mode biquad consisting of only ZC-CFTAs and grounded capacitors," *Radioengineering,* vol. 20, pp. 650-655, 2011.
16. D. Biolek, V. Biolkova, Z. Kolka, and J. Bajer, "Single-input multi-output resistorless current-mode biquad," in *2009 European Conference on Circuit Theory and Design*, 2009, pp. 225-228. https://doi.org/10.1109/ECCTD.2009.5274928.
17. R. Senani and A. Singh, "A new universal current-mode biquad filter," *Frequenz,* vol. 56, pp. 55-59, 2002. https://doi.org/10.1515/FREQ.2002.56.1 -2.55.
18. M. Gupta, P. Dogra, and T. S. Arora, "Novel current mode universal filter and dual-mode quadrature oscillator using VDCC and all grounded passive elements," *Australian Journal of Electrical and Electronics Engineering,* vol. 16, pp. 220-236, 2019. https://doi.org/10.1080/1448837X.2019.1648134.
19. M. Sagbas and M. Koksal, "Current-mode state-variable filter," *Frequenz,* vol. 62, pp. 37-42, 2008. https://doi.org/10.1515/FREQ.2008.62.1 -2.37.
20. J. Jerabek, R. Sotner, and K. Vrba, "Comparison of the SITO current-mode universal filters using multiple-output current followers," in *2012 35th International Conference on Telecommunications and Signal Processing (TSP)*, 2012, pp. 406-410. https://doi.org/10.1109/TSP.2012.6256325.
21. R. Singh and D. Prasad, "Electronically Tunable SIMO type Mixed-mode Biquadratic Filter using Single FTFNTA," *Indian Journal of Pure & Applied Physics (IJPAP),* vol. 59, pp. 629-637, 2021.
22. L. Safari, G. Barile, G. Ferri, and V. Stornelli, "A new low-voltage low-power dual-mode VCII-based SIMO universal filter," *Electronics,* vol. 8, p. 765, 2019. https://doi.org/10.3390/electronics8070765.
23. A. Abaci and E. Yuce, "A new DVCC+ based second-order current-mode universal filter consisting of only grounded capacitors," *Journal of Circuits, Systems and Computers,* vol. 26, p. 1750130, 2017. https://doi.org/10.1142/S0218126617501304.
24. T. Parveen, "OFC based high output impedance current mode simo universal biquadratic filter," in *2011 International Conference on Multimedia, Signal Processing and Communication Technologies*, 2011, pp. 134-136. https://doi.org/10.1109/MSPCT.2011.6150456.
25. A. Kumar, A. K. Kushwaha, and N. Chander, "Current-mode SIMO universal filter realization using dual-X multi output current conveyor," in *TENCON 2019-2019 IEEE Region 10 Conference (TENCON)*, 2019, pp. 2179-2183. https://doi.org/10.1109/TENCON.2019.8929631.
26. S. Roy, T. K. Paul, S. Maiti, and R. R. Pal, "Voltage Differencing Current Conveyor Based Voltage-Mode and Current-Mode Universal Biquad Filters with Electronic Tuning Facility," *International Journal of Engineering and Technology Innovation,* vol. 11, p. 146, 2021. https://doi.org/10.46604/ijeti.2021.6821.
27. M. Faseehuddin, J. Sampe, S. Shireen, and S. H. M. Ali, "Lossy and lossless inductance simulators and universal filters employing a new versatile active block," *Informacije MIDEM,* vol. 48, pp. 97-114, 2018.
28. S. Singh, R. Tomar, and D. Chauhan, "A new current tunable current input current output biquad using CFTAs," *Journal of Engineering Science and Technology,* vol. 12, pp. 2268-2282, 2017.
29. A. Kumar and S. K. Paul, "DX-MOCCII based fully cascadable second order current-mode universal filter," *Journal of Circuits, Systems and Computers,* vol. 27, p. 1850113, 2018. https://doi.org/10.1142/S021812661850113X.
30. T. Ettaghzouti, N. Hassen, K. Garradhi, and K. Besbes, "SIMO high frequency active universal current mode filter with independent control of pole frequency and quality factor," in *2017 18th International Conference on Sciences and Techniques of Automatic Control and Computer Engineering (STA)*, 2017, pp. 157-162. https://doi.org/10.1109/STA.2017.8314934.
31. S. Maheshwari, "Current conveyor all-pass sections: brief review and novel solution," *The Scientific World Journal,* vol. 2013, 2013. https://doi.org/10.1155/2013/429391.

Arrived: 19. 06. 2022
Accepted: 08. 11. 2022

Original scientific paper
https://doi.org/10.33180/InfMIDEM2022.402

Informacije MIDEM
Journal of Microelectronics,
Electronic Components and Materials
Vol. 52, No. 4(2022), 215 – 226

Influence of Trace Eelements on the Electrical Properties of ZnO-based Multilayer Varistors

Slavko Bernik[1], Nana Brguljan[1], Marija Ercegovac[2], Zoran Samardžija[1]

[1]Department for Nanostructured Materials, Jožef Stefan Institute, Ljubljana, Slovenia
[2]Bourns, d.o.o., Žužemberk, Slovenia

Abstract: Nonlinear current-voltage (I-U) characteristics and stability after an I_{MAX} test of two types of multilayer varistors (MLVs), each type fabricated in two series, were analysed in terms of their structure, microstructure and the presence of trace (i.e., impurity) elements. The structural and microstructural features showed nothing significant that could justify the very different I_{MAX} characteristics of the MLVs of the same type from the two series. In the larger MLVs, declared for I_{MAX} 1000A, the most critical factor was found to be the amount of Fe, the source of which was the starting Cr_2O_3 powder; one batch of Cr_2O_3 used for their fabrication contained an about 5-times-larger amount of Fe than the other, while the amounts of the other impurity elements (i.e., Al, Si, Mg, Ca, Ti, Na, K) were similar in both. The MLV1000 samples prepared with the Fe-rich Cr_2O_3 powder failed after a current impulse of 900A, while the samples using the Fe-low Cr_2O_3 powder withstood even 1400A. In the smaller MLVs, declared for 200A, prepared from Fe-low Cr_2O_3 and added in half the amount as in the MLV1000 samples, the critical factor was the large addition of SiO_2 in the starting composition and the samples failed after a current impulse of 30 A. Amending the composition with the addition of several 100 ppm of Al resulted in an enhancement of I_{MAX} to 420A, demonstrating the positive effects of Al. The results indicated the need to control the presence of trace elements and showed the complexity of an issue that requires a thorough consideration for each type of MLV to achieve the required electrical characteristics.

Keywords: ZnO; multilayer varistors; trace elements; microstructure; electrical characteristics

Vpliv elementov v sledovih na električne lastnosti večplastnih varistorjev na osnovi ZnO

Izvleček: Nelinearne tokovno-napetostne (I-U) karakteristike in stabilnost po testu I_{MAX} dveh vrst večslojnih varistorjev (MLV), od katerih je bila vsaka izdelana v dveh serijah, smo analizirali glede na njihovo strukturo, mikrostrukturo in prisotnost elementov v sledovih (tj. nečistoč). Strukturne in mikrostrukturne značilnosti niso pokazale nič pomembnega, kar bi lahko pojasnilo zelo različne značilnosti I_{MAX} med MLV vzorci istega tipa iz obeh serij. Pri večjih MLV, deklariranih za I_{MAX} 1000A, se je izkazalo, da je najbolj kritičen dejavnik količina Fe, katerega vir je bil začetni prah Cr_2O_3; prah Cr_2O_3 ene serije, uporabljen za njihovo izdelavo, je vseboval približno 5-krat večjo količino Fe kot prah druge serije, medtem ko so bile količine ostalih nečistoč (tj. Al, Si, Mg, Ca, Ti, Na, K) v obeh podobne. Vzorci MLV1000, izdelani s prahom Cr_2O_3, bogatim s Fe, so odpovedali že po tokovnem impulzu 900 A, medtem ko so vzorci, pripravljeni s prahom Cr_2O_3 z malo Fe, zdržali celo 1400 A. Pri manjših MLV, deklariranih za 200 A, pripravljenih iz Cr_2O_3 z nižjo vsebnostjo Fe, ki je bil dodan v polovični količini kot pri vzorcih MLV1000, je bil kritičen dejavnik visok dodatek SiO_2 v začetni sestavi, tako da so vzorci odpovedali že po tokovnem impulzu 30 A. Sprememba sestave z dodatkom več 100 ppm Al je povzročila izboljšanje I_{MAX} na 420A, kar dokazuje pozitivne učinke Al. Rezultati so pokazali na pomembnost nadzora prisotnosti elementov v sledovih in na kompleksnost problematike, ki zahteva temeljit premislek za vsako vrsto MLV, da bi dosegli zahtevane električne karakteristike.

Ključne besede: ZnO; večplastni varistorji; nečistoče; mikrostruktura; električne lastnosti

** Corresponding Author's e-mail: slavko.bernik@ijs.si*

1 Introduction

Varistors, i.e., variable resistors are core elements of surge protection devices (SPDs), complying with a broad range of operating voltages for electrical devices and electronics, as well as for the stabilisation of low-, medium, and high-voltage electric power lines.

How to cite:
Slavko Bernik et al., "Influence of Trace Eelements on the Electrical Properties of ZnO-based Multilayer Varistors", Inf. Midem-J. Microelectron. Electron. Compon. Mater., Vol. 52, No. 4(2022), pp. 215–226

The varistors are made of ZnO-based varistor ceramics, which are characterised by an exceptional current-voltage (I-U) nonlinearity and a high energy-absorption capability. Accordingly, at the breakdown voltage the varistor switches from a highly resistive to a highly conductive state in a matter of nanoseconds and the current through the varistors increases by several orders of magnitude for a minimum change in voltage. Thus, a varistor connected in parallel effectively diverts the transient surge from the protected device to the ground and absorbs the excess harmful energy, ensuring the undisturbed and safe operation of the device, while preventing its damage or even destruction. The possibilities to tailor the break-down voltage of varistor ceramics from a few volts up to several kilo-volts enables suitable dimensions of varistors for applications across a broad range of voltages, a superior response time to transient surges, a high energy-absorption capability and a long-term operating stability and reliability. These advantages of varistors mean that they are effectively unmatched by any other surge-protection device. Hence, varistors dominate the worldwide, multi-billion euro business of overvoltage-protection applications [1-3].

The breakdown voltage of a varistor is proportional to the thickness of the ceramic and the energy-absorption capability is proportional to its volume. Hence, so-called bulk or disc varistors are predominantly used for medium- and high-voltage applications, which are also related to higher energies. For breakdown voltages below about 60V, thicknesses below 1 mm are required and the fabrication of such thin ceramic discs without any shape deformation during high-temperature sintering can be difficult, and there is a problem with their low fracture strength. With an increasing thickness-to-diameter ratio of the discs to increase their volume, and hence the energy-absorption capability, the problem of their low fracture strength further increases. The solution for low-voltage applications is multilayer varistors (MLV), which were developed in the 1980s as an answer to problems in low-voltage circuits, accompanied by a rapid trend for their miniaturisation and a constant demand for an enhanced integration scale in electronic circuits. The miniaturisation of electronic circuits increases their sensitivity to external interference and MLVs are used for low-voltage protection against transient surges caused by electrostatic discharge, atmospheric discharge and transient overvoltages generated for other reasons in integrated circuits, hybrid circuits and surface-mounted circuits [4-7]. Accordingly, MLVs also have key role in automotive-circuit protection as modern vehicles employ a variety of electronics for safety, assisted driving, self-driving, cameras, engine-performance optimisation with an engine-control unit, communications and navigation. Many of these systems require multiple processors as well as high-current sensors and actuators. Nowadays vehicles contain over 40 motors and actuators to drive windows, doors, seats, pumps, windshield wipers and other components. At the standard operating voltages of personal cars and trucks, i.e., 12V and 24V, respectively, the automotive MLVs with nominal voltages from 20 to 40V are exposed to extremely heavy loads that occur for instance when turning on or off the engine, or when any other power user is switched on (i.e., electrical adjustment of a seat, opening a window, etc.), which can cause transient voltage surges up to several 100 V lasting for several 100 ms and energy loads of more than 100 J. However, in hybrid electric vehicles using 48 V systems and plug-in electric cars using high-voltage systems (i.e., 400V and even higher) because the high voltage boosts efficiency and allows lower current for the same power (wattage), the requirements for MLVs are even greater. It should also be mentioned that MLVs have to show no deterioration in performance in the temperature range from – 55°C to 175°C. Accordingly, a great deal of attention has to be given to any detail of the fabrication technology for MLVs to comply with the rigorous performance requirements [8].

MLVs or "chip" varistors are composed from layers of fine-grained ZnO-based varistor ceramics with thicknesses typically in the range from 20 to 100 μm, internal electrodes connected in parallel and terminal outer electrodes, and are manufactured using multilayer fabrication technology. Flexible green ceramic tapes are prepared with tape-casting technology. Several green sheets with screen-printed inner electrodes (typically AgPd,) are stacked, isostatically laminated, diced into individual varistors, and co-sintered, typically at temperatures around 1000°C. The layers are laminated in a way that the inner electrodes form alternating connections between the two terminal electrodes; accordingly, every other layer connects to the same terminal electrode. Such a configuration allows for higher resistances at lower voltages with faster response times than the bulk metal oxide varistors (MOV). Basically, the breakdown or nominal voltage of MLVs is determined by the thickness of the ceramic layer between the two inner electrodes, while their energy-absorption capability can be adjusted with the number of layers (i.e., the thickness of MLV) and the area of MLV, i.e., by adjusting its volume [5, 9].

Among the generally well-known types of the ZnO-based varistor ceramics, i.e., ZnO-Bi_2O_3-based, ZnO-Pr_6O_{11}-bazed, and ZnO-V_2O_5-based, the ZnO-Bi_2O_3-based ones are the most widely used for bulk varistors and MLVs. ZnO is an n-type, wide-band-gap semiconductor. The current-voltage (I-U) nonlinearity, which is typically described with the expression (0)

$$I = kU^{a} \quad (0)$$

(k – constant, α – coefficient of nonlinearity), is induced to ZnO by the addition of varistor formers like Bi_2O_3; it segregates at the ZnO grain boundaries and results in the formation of electrostatic Schottky barriers so that the non-ohmic (i.e., varistor) grain boundary has a breakdown voltage U_{GB} of about 3.2V. Varistor formers facilitate the formation of acceptor states at the grain boundaries, i.e., oxygen interstitials (O_i'') and zinc vacancies (V_{Zn}', V_{Zn}''), which act as electron traps, while in the vicinity of grain boundaries, in the ZnO grain, a positively charged depletion layer of oxygen vacancies ($V_O^{\cdot}$, $V_O^{\cdot\cdot}$) and zinc interstitials ($Zn_i^{\cdot}$, $Zn_i^{\cdot\cdot}$) is formed. The weak nonlinearity of Bi_2O_3-doped ZnO with α of about 3 is further enhanced by the addition of dopants like Sb_2O_3, Co_3O_4, Mn_3O_4, NiO and Cr_2O_3 to values of α from 20 to 80. While some of these dopants are essential to increase the electrical conductivity of the ZnO grains (Co, Mn, Ni), the other (Sb, Cr) affect the growth of the ZnO grains and thus enable tailoring of the breakdown voltage (U_B) of varistor ceramics via grain size (G) in accordance with the expression (1)

$$U_B = \frac{U_{GB} * t}{G} = U_{GB} * N_{GB} \quad (1)$$

where *t* is thickness of ceramics and N_{GB} number of grain boundaries. Although the varistor dopants added to ZnO typically account in total for less than 10 wt.%, such a composition results in a rather complex microstructure of the varistor ceramics. It contains the ZnO phase and secondary phases of the ZnO-Bi_2O_3-Sb_2O_3 system, i.e., a Bi_2O_3-rich phase, a $Zn_7Sb_2O_{12}$-type spinel phase and a $Bi_3Zn_2Sb_3O_{14}$-type pyrochlore phase, while the other varistor dopants (i.e., Co, Mn, Ni, Cr) are incorporated into these phases. The electrical characteristics of the varistor ceramics, i.e., breakdown voltage (U_B), coefficient of nonlinearity (α) and leakage current (I_L), are primarily affected by the ZnO phase, which must be highly conductive, and the Bi_2O_3-rich phase at the grain boundaries for their non-ohmic varistor characteristic (highly resistive at voltages below U_B). It is also important that the Bi_2O_3 forms a liquid phase during sintering and, besides the ZnO, dissolves all the other varistor dopants, thus greatly affecting their distribution in the microstructure as well as the sintering and the grain-growth process. Accordingly, all the dopants in equilibrium amounts are incorporated into the Bi_2O_3-rich phase, thus affecting the electronic states at the grain boundaries and consequently also their electrical characteristics [1, 2, 6, 7].

Some elements can greatly affect the electrical characteristics of the varistor ceramics in very small amounts of up to only several 100ppm. They can act as donors, acceptors, or both, depending on the nature, concentration and location in the host crystal lattice. In the microstructure they can be grain boundary or grain specific and accordingly they affect the current-voltage (I-U) characteristics in the "pre-breakdown" region at low currents or in the "upturn" region at high currents, or both. The controlled addition of such carefully selected elements can be used for a targeted improvement of the electrical and energy characteristics of varistor ceramics. For example, fine doping with Al is generally used for the enhanced stability of varistor ceramics at high currents due to the improved electrical conductivity of the ZnO grains; however, it also increases the leakage current. In contrast, the fine addition of Si increases the resistivity of the grain boundaries, thus it is often used to decrease the leakage current of varistor ceramics. Unfortunately, elements that strongly affect the functional properties of varistor ceramics, even in very small quantities, can also be added unintentionally as impurities of the standard varistor dopants, which represents a serious problem. Hence, it is important to control the presence of impurity elements in the oxide powders used for the fabrication of varistor ceramics [10-12].

In this work two types of the multilayer varistors (MLV) from two fabrication series were analysed and their current-voltage (I-U) and energy characteristics are discussed in terms of their structure, microstructure and the presence of impurity (i.e., trace) elements, the primary source of which was confirmed to be the starting Cr_2O_3 powder. In the larger type of MLVs, used for maximum current impulses of I_{MAX}=1000A, the most critical for the stability against high current impulses was the amount of Fe impurity present. At a much lower amount of Fe (< 10 ppm) and a similar amount of other impurities (i.e., Al, Si, Mg, Ca, Ti, Na, K) the characteristics of this type of MLV were excellent with an I_{MAX} of 1400A, while MLVs prepared from Fe-rich Cr_2O_3 and thus containing about 40 ppm of Fe failed at current impulses of 900A. In the case of smaller MLVs, declared for I_{MAX}=200A, too much SiO_2 added in the starting composition was found to be critical and they failed at 30A. However, amending their starting composition with the addition of Al resulted in significantly improved energy characteristics, raising their I_{MAX} to 420A. The results indicated the importance of controlling the presence of trace elements, which can critically affect the performance of MLVs.

2 Materials and methods

Two types of MLVs, i.e., the larger, declared for a maximum impulse current (I_{MAX}) of 1000A (labelled MLV1000) and the smaller, declared for an I_{MAX} of 200A (labelled

MLV200), were prepared with standard multilayer fabrication technology in the Bourns company [4, 13]. In all the MLVs the same reagent grade powders of oxides of Zn, Bi, Sb, Co, Mn, Cr and Si were used; however, in the case of Cr_2O_3, powders from the same producer but from two different batches were used, both having the same composition according to the supplier, and are here labelled Cr1 and Cr2. For the MLV1000, ceramic tapes with the composition 97.9ZnO + 2.1(Bi_2O_3, Sb_2O_3, Co_3O_4, Mn_3O_4, Cr_2O_3) were used. One series of this type was prepared from tapes with Cr1 (series MLV1000-Cr1) and the other series from ceramic tapes with Cr2 (series MLV1000-Cr2). The smaller MLVs were prepared from ceramic tapes with the composition 98.0ZnO + 2.0(Bi_2O_3, Sb_2O_3, Co_3O_4, Mn_3O_4, Cr_2O_3, SiO_2); in one series the tapes containing Cr2 (series MLV200-Cr2) and in the other series the ceramic tapes also contained Cr2 but with their composition altered with addition of several 100 ppm of Al as solution of $Al(NO_3)_3 \cdot 9H_2O$ (series MLV200-Cr2Al). It should be mentioned that in the MLV1000 the amount of added Cr_2O_3 was twice the amount added in the MLV200. In the MLV200 samples, however, also a large amount of about 0.1mol.% of SiO_2 was added to the starting composition of the ceramic tapes, which was not added to the MLV1000. All the series of MLVs were co-sintered with AgPd electrodes in air at about 1000°C for the same duration, the series MLV200 at about 20 to 30°C lower temperature than the series of MLV1000 samples.

The current-voltage (I-U) characteristics of the MLV samples were measured using a Keithley 2410 Source Meter, i.e., nominal voltage (i.e., breakdown voltage), U_N, was determined at a current of 1 mA, leakage current, I_L, at $0.75U_N$, and the coefficient of nonlinearity, α, was determined in accordance with the equation (2)

$$a = \frac{\log\left(\frac{I_2}{I_1}\right)}{l\log\left(\frac{U_2}{U_1}\right)} \quad (2)$$

where U2 and U1 are voltages measured at I1 = 1 mA and I2 = 10 mA, respectively. The high current stability was determined by the maximum impulse current (I_{MAX}) at which the U_N of the MLVs changes by less than 10%. The I_{MAX} of the samples was analysed using an AMC MIG0606 impulse generator with current impulses of shape 8/20 (i.e., rising time 8 μs, duration 20 μs) to simulate impulses caused by a lightning strike) at current intensities from 200A to 500A for series MLV200 and from 900A to 1500A for series MLV1000. The I-U characteristics of the samples were measured before and after the current impulse test and their average values determined based on measurements of at least 10 samples per test.

Microstructures in the cross-section of the MLVs, perpendicular to the plane of the internal electrodes, were prepared and analysed in the scanning electron microscope (SEM) JEOL JSM-7600F equipped with an energy-dispersive spectrometer (EDS) Oxford Instruments INCA. The integrity of the inner electrodes, the distance between them and their connectivity to the terminal electrodes was examined. Also, the microstructure of the varistor ceramics was analysed with regard to the phase composition, phase homogeneity of the microstructure, porosity, grain size and grain size distribution. The phase composition of the ceramics was also determined with a powder x-ray diffraction analysis (XRD).

Furthermore, starting oxide powders used for the preparation of the foils of varistor ceramic using tape-casting technology were examined for their crystal structure (XRD), grain size and grain size distribution (particle size analyser HORIBA), morphology of the particles (SEM analysis), and the chemical composition (SEM/EDS). Finally, for all the used oxide powders, a precise quantitative analysis of the trace impurity elements was also made using the inductively coupled plasma - optical emission spectrometry method (ICP-OES).

3 Results and discussion

The average current-voltage (I-U) characteristics of the MLV1000 samples before and after the I_{MAX} current impulse test are presented in Tables 1 and 2. For this type of MLV an I_{MAX} of at least 1000A is required, and as can be seen in Table 1 none of the MLV samples from the series MLV1000-Cr1 complied with this requirement. In the first line of the table (i.e., shaded grey) the average I-U characteristics of all the MLV samples from this series measured before the I_{MAX} test are given. In comparison to these reference values, already after current impulse of 900A the I-U characteristics deteriorated, as indicated by a decrease of the nominal voltage (U_N) and the coefficient of nonlinearity (α), while the leakage current (I_L) significantly increased. The degradation of the I-U characteristics of the MLVs from this series further increased with a rising of the current impulse's intensity so that after an impulse of 1200A the average U_N decreased by 34 %, the α decreased by 50% from 34 to 17, and the I_L increased strongly. In contrast, the samples from the series MLV1000-Cr2 (Table 2) showed excellent stability even after current impulses of 1300A and 1400A, and failed only after tests at 1500A.

Table 1: Current-voltage characteristics (I-U) of MLV1000 samples from series MLV1000-Cr1 before and after I_{MAX} test.

I_{MAX} /A	U_N/V (±σ/%)	α (±σ/%)	I_L/μA (±σ/%)	ΔU_N /%
Ref.	35.1 (3)	34 (6)	1.6 (70)	/
900	29.1 (54)	25 (57)	201 (223)	-17
1000	30.5 (38)	22 (61)	202 (221)	-13
1100	24.3 (61)	16 (89)	403 (135)	-30
1200	23.0 (74)	17 (88)	438 (119)	-34

Such drastically different I_{MAX} characteristics between the MLV1000 samples from two series could result from some failure in their fabrication, which would show in their microstructure. Accordingly, their microstructures were examined for possible defects to the internal electrodes, like not being whole or continuous, but with interruptions, uniformity of the distance between internal electrodes, number of internal electrodes, poor or failed connection of the internal electrodes with terminal electrodes, and also in regard to the microstructure and phase composition of the varistor ceramics. The microstructures of several MLV1000 samples from each series were examined on the SEM and nothing significant that could explain the different electrical characteristics was found. Typical microstructures of the MLV1000 samples in the cross-section direction are presented in Fig. 1.

Table 2: Current-voltage characteristics (I-U) of MLV1000 samples from series MLV1000-Cr_2 before and after I_{MAX} test.

I_{MAX} /A	U_N/V (±σ/%)	α (±σ/%)	I_L/μA (±σ/%)	ΔU_N /%
Ref.	33.0 (2)	33 (4)	1.4 (36)	/
1300	32.9 (4)	32 (4)	2.9 (70)	1
1400	33.4 (1)	32 (3)	3.9 (54)	1
1500	24.6 (58)	20 (81)	402 (136)	-27

The internal electrodes, 7 in total, were found in all the analysed samples from both series to be continuous, at a uniform distance of about 104 μm, and all well in contact with the terminal electrodes. Also, the SEM analysis of the varistor ceramics showed no difference in the microstructure of the MLV1000 samples from both series in terms of porosity, phase composition and homogeneity in the distribution of secondary phases among the ZnO grains. In all the samples, besides the matrix ZnO phase, also a secondary Bi_2O_3-rich liquid phase, a $Zn_7Sb_2O_{12}$-type spinel phase, and a $Bi_3Zn_2Sb_3O_{14}$-type pyrochlore phase were determined by the EDS analysis. In Fig. 2, typical microstructures and phase compositions of the samples MLV1000-Cr1

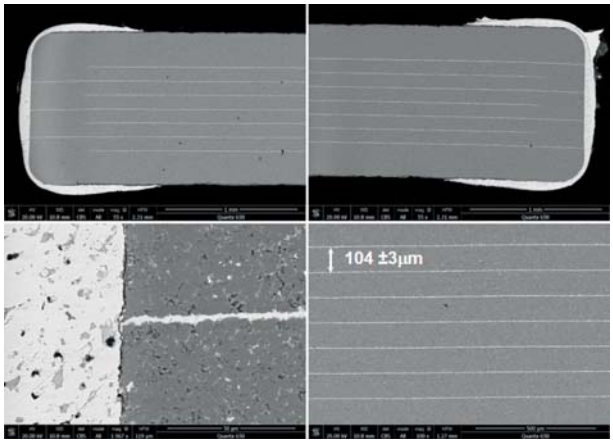

Figure 1: Typical microstructure of MLV1000 samples in cross-section showing internal electrodes and their connection to the terminal electrodes.

(2.a-b) and MLV1000-Cr2 (1.c-d) are shown. SEM analysis of the etched microstructures (Fig. 3) showed that the samples MLV1000 from both series also have similar ZnO grain sizes and size distributions (Fig. 3).

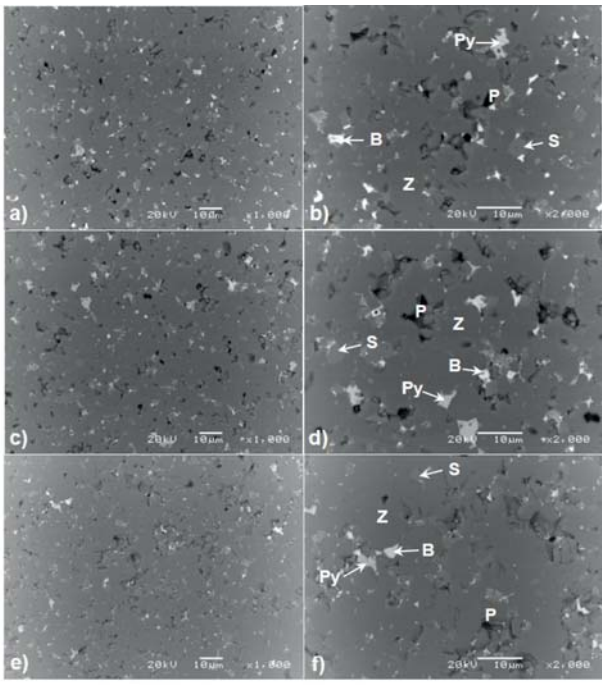

Figure 2: SEM images in backscattered mode (BE) of the microstructures of the MLV samples; (a,b) MLV1000-Cr1, (c,d) MLV1000-Cr2, and (e,f) MLV200-Cr2. Phase labelling: Z – ZnO phase, B – Bi_2O_3-rich phase, Py – $Bi_3Zn_2Sb_3O_{14}$-type pyrochlore phase, S – $Zn_7Sb_2O_{12}$-type phase, P – pore.

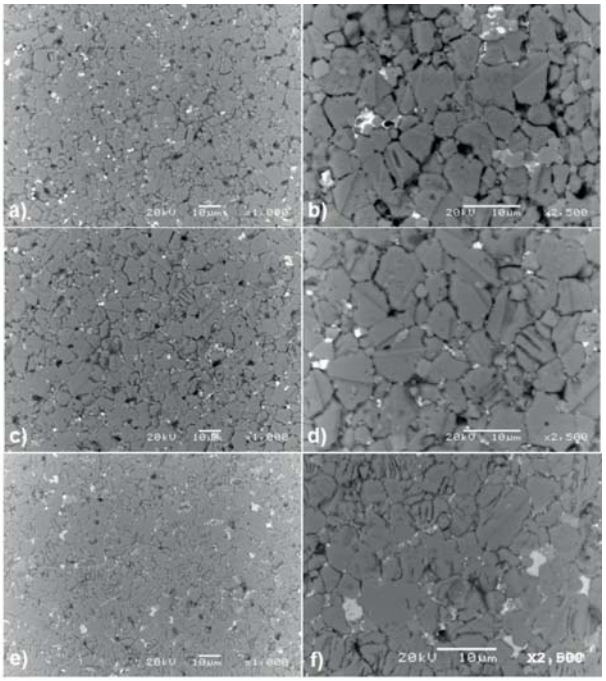

Figure 3: SEM/BE images of the etched microstructures of the MLV samples; (a,b) MLV1000-Cr1, (c,d) MLV1000-Cr2, and (e,f) MLV200-Cr2.

The XRD analysis also confirmed the same phase composition of the MLV1000 samples from both series, showing besides the ZnO phase also a Bi_2O_3-rich liquid phase as a γ-Bi_2O_3 modification and a $Zn_7Sb_2O_{12}$-type spinel phase. The XRD peaks of the $Bi_3Zn_2Sb_3O_{14}$-type pyrochlore phase, which was found by the SEM/EDS analysis in the microstructures of the MLV1000 samples, strongly overlap with the other phases present. Hence, it is difficult to detect pyrochlore phase in the varistor ceramics by the XRD analysis. The typical XRD pattern of the varistor ceramics in the analysed MLV samples is shown in Fig. 4.

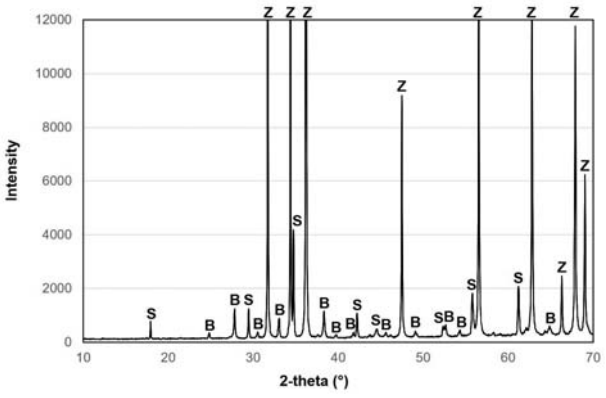

Figure 4: Typical XRD pattern of the varistor ceramics in the analysed MLV samples. Phase labelling: Z – ZnO phase, B – γ-Bi_2O_3 phase, S - $Zn_7Sb_2O_{12}$-type phase.

The average I-U characteristics of the smaller MLV200 samples before (i.e., reference values) and after the current impulse test are given in Tables 3 and 4. The samples of the series MLV200-Cr2 showed extremely poor I_{MAX} characteristics (Table 3); while they should withstand a current impulse of 200A with a change in the U_N of less than 10% at a preserved coefficient of nonlinearity (α) and a low leakage current (I_L), even a current impulse of just 30A resulted in a significant decrease of U_N by 18%, accompanied with a decrease in α and a significant increase in I_L.

Table 3: Current-voltage characteristics (I-U) of the MLV200 samples from the series MLV200-Cr2 before (reference values) and after I_{MAX} test.

I_{MAX} /A	U_N/V (±σ/%)	α (±σ/%)	I_L/µA (±σ/%)	ΔU_N /%
Ref.	28.1 (3)	29 (6)	0.2 (106)	/
30	23.0 (53)	24 (53)	200 (224)	-18
50	23.4 (51)	24 (53)	200 (224)	-17
100	12.9 (61)	13 (121)	600 (91)	-30

The samples from the series MLV200-Cr2Al (Table 4), however, showed excellent stability for current impulses, even up to 420A, while after a load with 440 A their I-U characteristics significantly decreased and even more after a current impulse of 500A.

Table 4: Current-voltage characteristics (I-U) of the MLV200 samples from the series MLV200-Cr2Al before (reference values) and after I_{MAX} test.

I_{MAX} /A	U_N/V (±σ/%)	α (±σ/%)	I_L/µA (±σ/%)	ΔU_N /%
Ref.	26.9 (4)	32 (8)	1.5 (109)	/
200	28.1 (2)	33 (10)	0.6 (24)	1
260	28.7 (2)	31 (9)	0.4 (28)	1
300	27.1 (4)	31 (8)	1.5 (121)	1
340	27.1 (3)	31 (19)	1.4 (11)	1
380	26.5 (3)	26 (14)	1.7 (38)	2
400	26.7 (2)	28 (31)	1.9 (68)	2
420	26.8 (1)	30 (4)	2.3 (31)	1
440	19.4 (56)	18 (80)	402 (136)	-27
500	11.5 (119)	10 (121)	647 (76)	-56

Microstructural analysis of the MLV200 samples from both series showed that all six internal electrodes have a similar thickness and are continuous, even at a distance of about 80 µm, and well connected to the terminal electrodes (Fig. 5). Also, the SEM/EDS analysis of the varistor ceramics showed similar microstructures in terms of the phase composition and the grain size (Figs. 2.e-f, and 3.e-f). The same phase composition of

the varistor ceramics in the MLV200 samples from both series was also confirmed by the XRD analysis (Fig. 4).

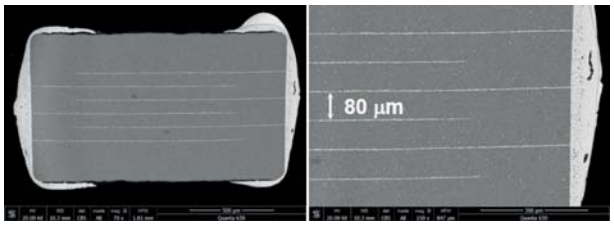

Figure 5: SEM/BE images showing typical cross-section microstructure of the samples MLV200.

The results showed that in both types of MLVs, the MLV1000 and MLV200 of both series, varistor ceramics have similar microstructures and phase compositions according to the SEM/EDS and XRD analysis. Actually, these analyses revealed nothing related to the microstructure of the ceramics and the structure of the MLVs, including possible technical errors in their fabrication, that could explain such drastically different stabilities in the I-U characteristics after the current impulse tests (IMAX test) between the same type of MLVs from two fabrication series. However, such results indicated that attention should be given to know the differences in the preparation of the MLV samples, i.e., in the case of the MLV1000 samples the use of Cr_2O_3 from different batches and in the case of MLV200 samples an alteration of the composition with the addition of Al in one fabrication series as compared to the other, while in both the Fe-low Cr_2O_3 from the same batch was used. Accordingly, the Cr_2O_3 powders used for the preparation of the MLV samples were thoroughly analysed.

Granulometric analyses of the Cr_2O_3 powders from both batches showed that they have similar average particle sizes of about 2.1 μm and also similar particle size distributions in the range from 0.2 μm to 10 μm, as shown in Fig. 6. The typical morphology of the used Cr_2O_3 powders is shown in Fig. 7 and compliments the results of the granulometric analysis.

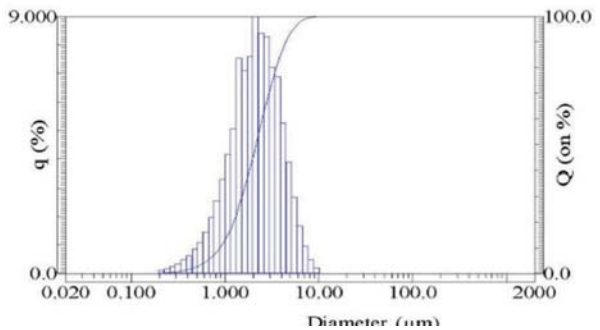

Figure 6: Histogram of the particle size distribution in the Cr_2O_3 powder.

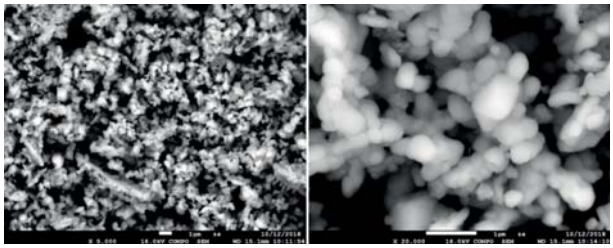

Figure 7: SEM images showing typical morphology of the Cr_2O_3 powders used for the fabrication of the MLV samples.

The XRD patterns of both powders are very similar (Fig. 8) and can be identified using the reference pattern for Cr_2O_3 JCPDF 00-038-1479. However, in the Cr1 powder additional minor peaks indicate the presence of some SiO_2 secondary phase (JCPDF01-082-1556).

Detailed SEM/EDS analyses revealed, in both Cr_2O_3 powders, the presence of a significant amount of secondary phases as coarse-grained inclusions containing impurity elements, primarily Si, Al and Fe, and also K, Na, Ca and Ti (Fig. 9). Hence, a quantitative chemical ICP-OES analysis was made to determine the content of trace impurity elements in the Cr_2O_3 powders. The results of the ICP-OES analysis of the Cr_2O_3 from both batches are presented in Table 5.

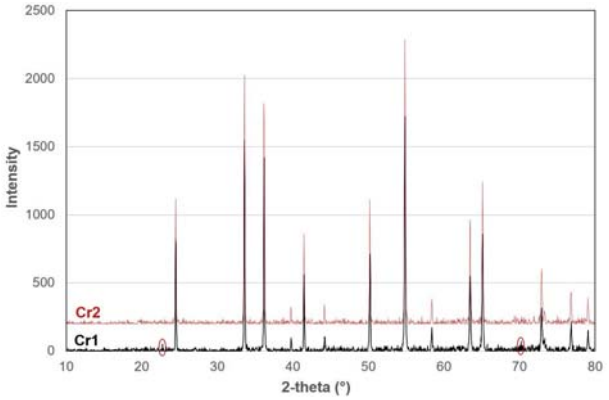

Figure 8: XRD patterns of the Cr_2O_3 powders; in the Cr1, additional to the peaks of Cr_2O_3, also additional minor peaks indicate the presence of the SiO_2 secondary phase.

The quantitative ICP-OES analysis of all the other oxides used for the fabrication of the studied MLV samples (i.e., ZnO, Sb_2O_3, Co_3O_4, and Mn_3O_4) showed the presence of the impurity elements below 50 ppm, confirming that the main source of impurities is Cr_2O_3.

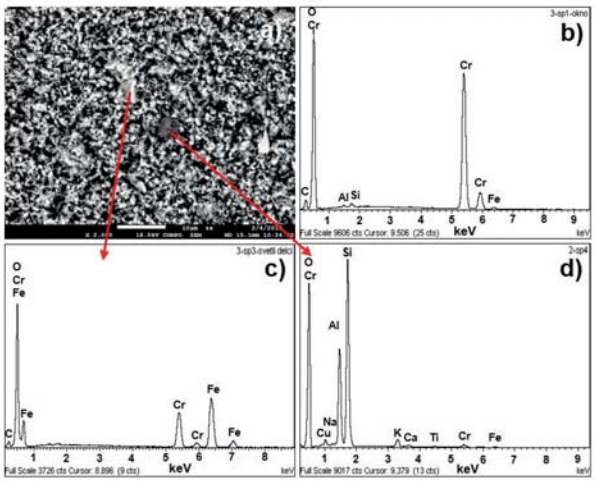

Figure 9: a) SEM/BE image of the Cr_2O_3 powder Cr1, b) EDS analysis of area on SEM image, c) point EDS analysis of lighter secondary phase, and d) points EDS analyses of darker secondary phase.

Table 5: Results of the quantitative ICP-OES analysis of the used Cr_2O_3 powders, i.e., Cr1 and Cr2, for the amount of impurity elements.

Composition	Cr_2O_3 powder	
M(ppm)/MO(wt.%)	Cr1	Cr2
Cr_2O_3	97.08	97.99
Si/SiO_2	10080/1.57	10020/1.49
Al/Al_2O_3	3502/0.12	2801/0.10
Fe/Fe_2O_3	9488/0.92	1944/0.19
Mg/MgO	932/0.10	779/0.09
Ca/CaO	888/0.08	797/0.08
Ti/TiO_2	172/0.02	127/0.01
Na/Na_2O	477/0.04	231/0.02
K/K_2O	870/0.07	351/0.03

These results showed the contamination of both Cr_2O_3 powders used in the preparation of the MLVs, with numerous impurity elements that are known to have an influence on the current-voltage (I-U) characteristics and the stability of the varistor ceramics. Several models are proposed, explaining the voltage stability/instability of the ZnO-based varistor ceramic through the degradation of the electrostatic barriers at the grain boundaries. However, it is common to most of them that the origin of the degradation is assigned to the diffusion of zinc interstitials (Zn_i) from the depletion layer and their chemical interaction with acceptor states at the grain boundaries, i.e., oxygen interstitials (O_i) and zinc vacancies (V_{Zn}), which consequently leads to the degradation and collapse of the electrostatic Schottky barriers [1, 10, 11, 14-16]. Their degradation is typically expressed by a decrease in the nominal (i.e., breakdown) voltage of the varistor ceramics (U_N) due to the reduced breakdown voltage of the grain boundaries (U_{GB}), a decrease in the coefficient of nonlinearity (α) and a significant increase of the leakage current (I_L), as observed in the case of the poor MLVs in this work. Actually, most of the impurity elements detected in the Cr_2O_3 are reported in the literature as having a positive influence in low amounts and some of them are even known as "varistor highlighters", like Al and Si, which are intentionally added to the starting composition in ppm amounts to enhance the performance of the varistor ceramics in the low-current pre-breakdown region or in the high-current "up-turn" region of their I-U curve [2]. They affect the defect equilibria and electronic states at the grain boundaries, and thus the height and stability of the electrostatic Schottky barriers at the grain boundaries, which are responsible for the I-U nonlinearity of varistor ceramics. On the other hand, they can increase the electrical conductivity of the ZnO grains, which has a positive influence on the stability and aging characteristics of varistor ceramics due to lowering the released Ohmic heat under high current loads [1, 10].

The main impurity detected in Cr_2O_3 powders is certainly Si (i.e. SiO_2), as can be seen in Table 5. Studies showed that SiO_2 in low amounts strongly affects the electronic states at the grain boundaries, resulting in an increase of the height of the electronic Schottky barriers and also the coefficient of nonlinearity (α). Also, the increased resistivity of the grain boundaries results in a lower leakage current (I_L). At the same time, SiO_2 also increases the depletion-layer width, leading to the enhancement of the breakdown voltage of the grain boundaries (U_{GB}). However, too much Cr_2O_3 could result in a deterioration of the I-U characteristics, especially once the secondary Zn_2SiO_4 phase starts to form at the grain boundaries [12, 17, 18]. Another impurity element detected in the Cr_2O_3 powders in amounts of several 1000ppm is Al; it is often considered at the main "varistor highlighter" and also generally known as the main donor dopant in ZnO-based ceramics. Numerous studies showed that it enhances the energy stability of the ZnO-based varistor ceramics when added in amounts of several 100 ppm, by increasing the conductivity of the ZnO grains. However, Al is not a grain selective dopant, but also influences the electronic states at the grain boundaries, resulting in an increase of the leakage current (I_L). Also, at higher amounts of Al, which depends on the sintering temperature and time, it starts to incorporate at the interstitial sites in the crystal structure of ZnO, acting as an acceptor and decreasing the conductivity of the ZnO grains. Hence, thorough control of the amount of Al is required, depending on the sintering conditions [11, 19-22]. The amphoteric dopants in ZnO are Na and K. In very low amounts of a few 10 ppm, Na (and K) incorporate at the

interstitial sites of the ZnO crystal lattice and act as donors, increasing the electrical conductivity of the ZnO grains, while at the same time they substitute for the interstitial Zn (Zn_i) in the depletion layer, decreasing its concentration and thus increasing the stability of ZnO varistor ceramics. However, in larger amounts, Na (K) incorporates at the regular sites of Zn in the structure of ZnO (Na_{Zn}') and acts as an acceptor, decreasing the electrical conductivity of the ZnO grains [10, 23, 24]. The positive influence of low levels of doping was also reported for Mg [24, 25] and Ca [24, 26-28]; both of them result in a decrease of the leakage current (I_L), an increase of the breakdown voltage (U_B) and an increase of the coefficient of nonlinearity (α). In the case of Ca it has been reported that it increases the solid solubility of Al in the ZnO, thus enhancing the electrical conductivity of the ZnO grains, while reducing the accumulation of Al at the grain boundaries, which increases their resistivity [28]. If added in too large amounts, each of them results in secondary phases at the grain boundaries of the ZnO, causing deterioration of the I-U characteristics of varistor ceramics; in the case of Mg the Mg-Zn-O periclase solid solution is formed [25], and in the case of Ca the Ca-Bi-O phases [26]. In contrast to other impurity elements found in Cr_2O_3, which have a positive influence, Fe has a negative influence on the I-U characteristics of the varistor ceramics already in low amounts [29-32], decreasing the breakdown voltage (U_B) and the coefficient of nonlinearity (α), and increasing the leakage current (I_L). Peiteado et al. [30] explained such influence of Fe by its incorporation into the $Zn_7Sb_2O_{12}$-type spinel phase at the grain boundaries, which strongly increases the electrical conductivity of otherwise insulating secondary phase, and thus increases the conductivity of varistor ceramics below the breakdown voltage, enhancing their electrical degradation.

Some of the impurity elements are present in the Cr_2O_3 powders in significant amounts of several 1000 ppm, and if present in such amounts in the varistor ceramics, they would likely have a negative influence on the I-U characteristics. However, for the amounts of Cr_2O_3 in the composition of the varistor ceramics, 1000 ppm of the impurity element in Cr_2O_3 means about 4 ppm in the varistor ceramics. Accordingly, most of the impurity elements, which are introduced by Cr_2O_3 into the varistor ceramics of the studied MLV samples, are present in very low amounts. This can have a positive influence on their I-U characteristics, if any. Only Fe is known to have a negative influence and in the I-U characteristics of varistor ceramics, even in very small amounts. In the samples from the series MLV1000-Cr1, the Fe is present in the amount of almost 40 ppm and in the same type MLV samples from the series MLV1000-Cr2 only in the amount of about 8 ppm. Accordingly, too much Fe in the MLV1000-Cr1 samples is the likely reason for their poor I_{MAX} characteristic, when they failed at a current impulse of 900A (Table 1). In the samples MLV1000-Cr2, however, the amount of Fe is below some critical value; therefore, they can have an excellent I_{MAX} of 1400A (Table 2).

In the smaller MLV200 samples, the amount of added Cr_2O_3 is half the amount added in the samples MLV1000-Cr_2. Hence, the amount of impurity elements in the varistor ceramics of MLV200 samples is even lower, only about 2 ppm for 1000 ppm present in Cr_2O_3. Accordingly, impurity elements probably have even less influence on the I-U characteristics of the MLV200 samples than on the MLV1000-Cr2 samples, but in the case of most of them, it is likely a positive one. This indicates that the poor I_{MAX} characteristics of the sample from the MLV200-Cr2 series (Table 3) is likely caused by too much SiO_2 in the starting composition of the varistor ceramics. However, the much better performance of the samples from the series MLV200-Cr2Al (Table 4), having the starting composition of the varistor ceramics corrected with the addition of Al in the optimal amount of several 100 ppm, indicates the positive effect of Al, compensating the negative effect of the excess Si, and thus increasing the I_{MAX} to even 420A.

4 Conclusions

Two types of ZnO-Bi_2O_3-based multilayer varistors (MLVs), declared for different maximum current impulses (I_{MAX}), were studied. Their current-voltage (I-U) and energy characteristics (I_{MAX} test with current impulses 8/20) were analysed in terms of their structure, microstructure, starting composition and presence of the impurity (i.e., trace) elements.

The larger MLV samples, declared for the I_{MAX} 1000A (MLV1000), which were fabricated in two series using Cr_2O_3 from different batches, showed dramatically different current-voltage (I-U) characteristics after I_{MAX} tests. The samples MLV1000 from one series failed already after a current impulse of 900A, while the samples from the other series preserved the I-U characteristics even after a load with a current impulse of 1400A. Detailed analysis of their microstructure, phase composition and internal structure showed nothing significant that could explain such large differences in I_{MAX} between the MLV1000 samples from both series. The compositional analysis showed that the used Cr_2O_3 powders contained a number of impurity elements in amounts from several 1000 ppm (Al, Fe) to even 10,000 ppm (Si), and from a few 100 ppm to 1000 ppm (Mg, Ca, Ti, Na, K). While the amount of most impurity elements was similar in the Cr_2O_3 powders from both series,

the amount of Fe in one powder was almost 5 times higher (9500 ppm) than in the other (1950 ppm). For the amount of Cr_2O_3 in the composition of varistor ceramics, 1000 ppm of the impurity element in the Cr_2O_3 means about 4 ppm in the varistor ceramics. Most of these elements are known to enhance the nonlinear I-U characteristics and the stability of the ZnO-Bi_2O_3-based varistor ceramics when present in such low amounts as introduced by the Cr_2O_3. The exception is Fe, which is known to degrade the I-U characteristics already for very small amounts. The difference in the I_{MAX} of the MLV1000 samples from the two series can be attributed to different content of Fe. In the poor series of MLV1000 samples, the Fe-rich Cr_2O_3 powder resulted in almost 40 ppm of Fe in the varistor ceramics and consequently a degradation of their I-U characteristics even for current impulses below the declared 1000A. For comparison, in the good MLV1000 series, the Fe-low Cr_2O_3 powder introduced less than 10 ppm of Fe to the varistor ceramics.

In the case of smaller MLVs, declared for 200A, with the Fe-low Cr_2O_3 added in half the amount as in the samples MLV1000 and with addition of SiO_2, also significant differences in I_{MAX} characteristics were observed between the two fabrication series, one with and one without the addition of Al. The samples from the series without added Al failed already after a current impulse of 30 A. In contrast, the samples from the other series having a starting composition of the varistor ceramics amended with the addition of several 100ppm of Al endured current impulses with the shape 8/20 even up to 420A without changes in their I-U characteristics and failed only at higher current impulses. Such results indicated that the addition of Al neutralized the negative effect of the too large amount of added SiO_2 and significantly improved the I_{MAX} characteristics of the MLV200 samples.

The results show the importance of controlling the presence of trace elements, the source of which can be the starting raw materials for the preparation of varistor ceramics, or they could be intentionally added in the starting composition, as well as understanding their influence so as to achieve the required MLV properties.

5 Acknowledgments

This work was supported by the European Regional Development Fund and Ministry of Education, Science and Sport of Republic of Slovenia (Project Grants C3330-18-952024).

6 Conflict of Interest

The authors declare no conflict of interest in connection to the work presented.

7 References

1. D. R. Clarke, "Varistor ceramics," *Journal of the American Ceramic Society,* vol. 82, no. 3, pp. 485 - 502, 1999.
2. T. K. Gupta, "Application of zinc oxide varistors," *Journal of the American Ceramic Society,* vol. 73, no. 7, pp. 1817-1840, 1990.
3. "Global Metal Oxide Varistor Market Size - Global Industry Size, Share, Trends, Competitions and Forecast, 2017-2022," 2022.doi: https://www.techsciresearch.com/report/metal-oxide-varistor-market/3674.html
4. D. Szwagierczak, J. Kulawik, and A. Skwarek, "Influence of processing on microstructure and electrical characteristics of multilayer varistors," *Journal of Advanced Ceramics,* vol. 8, no. 3, pp. 408-417, 2019. https://doi.org/10.1007/s40145-019-0323-7
5. L. Wang, G. Tang, and Z.-K. Xu, "Preparation and electrical properties of multilayer ZnO varistors with water-based tape casting," *Ceramics International,* vol. 35, no. 1, pp. 487-492, 2009. https://doi.org/10.1016/j.ceramint.2008.01.011
6. W.-H. Lee, W.-T. Chen, Y.-C. Lee, S.-P. Lin, and T. Yang, "Relationship between Microstructure and Electrical Properties of ZnO-based Multilayer Varistor," *Japanese Journal of Applied Physics,* vol. 45, no. 6A, pp. 5126-5131, 2006. https://doi.org/10.1143/jjap.45.5126
7. S. Hirose, K. Nishita, and H. Niimi, "Influence of distribution of additives on electrical potential barrier at grain boundaries in ZnO-based multilayered chip varistor," *Journal of Applied Physics,* vol. 100, no. 8, 2006. https://doi.org/10.1063/1.2358833
8. (2019). *Multilayer varistors in automotive circuit protection*. Available: https://electronics360.globalspec.com/article/14398/multilayer-varistors-in-automotive-circuit-protection
9. J. Kulawik, D. Szwagierczak, and A. Skwarek, "Electrical and microstructural characterization of doped ZnO based multilayer varistors," *Microelectronics International,* vol. 34, no. 3, pp. 116-120, 2017. https://doi.org/10.1108/mi-02-2017-0009
10. T. K. Gupta and A. C. Miller, "Improved stability of the ZnO varistor via donor and acceptor doping

at the grain boiundary," *Journal of Material Research,* vol. 3, no. 4, pp. 745-751, 1988.
11. T. K. Gupta, "Microstructural engineering through donor and acceptor doping in the grain and grain boundary of a polycristalline semiconducting c eramics," *Journal of Material Research,* vol. 7, no. 12, pp. 3280-3295, 1992.
12. B. Wang, Z. Fang, Z. Fu, and Y. Peng, "Electrical Behavior against Current Impulse in ZnO Varistor Ceramics with SiO_2 Addition," *Journal of Physics: Conference Series,* vol. 1637, no. 1, 2020. https://doi.org/10.1088/1742-6596/1637/1/012026
13. J. Sun, B. Luo, and H. Li, "A Review on the Conventional Capacitors, Supercapacitors, and Emerging Hybrid Ion Capacitors: Past, Present, and Future," *Advanced Energy and Sustainability Research,* vol. 3, no. 6, 2022. https://doi.org/10.1002/aesr.202100191
14. J. He, C. Cheng, and J. Hu, "Electrical degradation of double-Schottky barrier in ZnO varistors," *AIP Advances,* vol. 6, no. 3, 2016. https://doi.org/10.1063/1.4944485
15. T. K. Gupta and W. G. Carlson, "A grain-boundary defect model for stability/instability of a ZnO varistor," *Journal of Materials Science,* vol. 20, pp. 3487-3500, 1985.
16. Y. Huang, M. Guo, and J. Li, "Multiscale defect responses in understanding degradation in zinc oxide varistor ceramics," *Ceramics International,* vol. 46, no. 14, pp. 22134-22139, 2020. https://doi.org/10.1016/j.ceramint.2020.05.286
17. H. Bai *et al.*, "Influence of SiO_2 on electrical properties of the highly nonlinear ZnO-Bi_2O_3-MnO_2 varistors," *Journal of the European Ceramic Society,* vol. 37, no. 13, pp. 3965-3971, 2017. https://doi.org/10.1016/j.jeurceramsoc.2017.05.014
18. Z. H. Wu, J. H. Fang, D. Xu, Q. D. Zhong, and L.-y. Shi, "Effect of SiO_2 addition on the microstructure and electrical properties of ZnO-based varistors," *International Journal of Minerals, Metallurgy, and Materials,* vol. 17, no. 1, pp. 86-91, 2010. https://doi.org/10.1007/s12613-010-0115-0
19. W. Long, J. Hu, J. Liu, J. He, and R. Zong, "The Effect of Aluminum on Electrical Properties of ZnO Varistors," *Journal of the American Ceramic Society,* vol. 93, no. 9, pp. 2441-2444, 2010. https://doi.org/10.1111/j.1551-2916.2010.03787.x
20. Q. Fu, C. Ke, Y. Hu, Z. Zheng, T. Chen, and Y. Xu, "Al-doped ZnO varistors prepared by a two-step doping process," *Advances in Applied Ceramics,* vol. 117, no. 4, pp. 237-242, 2018. https://doi.org/10.1080/17436753.2017.1405556
21. M. Houabes, S. Bernik, C. Talhi, and A. Bui, "The effect of aluminium oxide on the residual voltage of ZnO varistors," *Ceramics International,* vol. 31, no. 6, pp. 783-789, 2005. https://doi.org/10.1016/j.ceramint.2004.09.004
22 S. Bernik and N. Daneu, "Characteristics of .ZnO-based varistor ceramics doped with Al_2O_3," *Journal of the European Ceramic Society,* vol. 27, no. 10, pp. 3161-3170, 2007. https://doi.org/10.1016/j.jeurceramsoc.2007.02.176
23. M. Peiteado, Y. Iglesias, and A. C. Caballero, "Sodium impurities in ZnO–Bi_2O_3–Sb_2O_3 based varistors," *Ceramics International,* vol. 37, no. 3, pp. 819-824, 2011. https://doi.org/10.1016/j.ceramint.2010.10.016
24. E. L. Tikhomirova, O. G. Gromov, and Y. A. Savel'ev, "Effect of Impurities on Varistor Properties of High-Voltage ZnO Ceramics," *Russian Journal of Applied Chemistry,* vol. 94, no. 4, pp. 437-441, 2021. https://doi.org/10.1134/s1070427221040029
25. A. Smith, G. Gasgnier, and P. Abelard, "Voltage-Current Characteristics of ZnO varistors of a Simple Zinc Oxide Varistor Containing Magnesia," *Journal of the American Ceramic Society,* vol. 73, no. 4, pp. 1098-1099, 1990.
26. K. Hembram, T. N. Rao, M. Ramakrishana, R. S. Srinivasa, and A. R. Kulkarni, "Influence of CaO doping on phase, microstructure, electrical and dielectric properties of ZnO varistors," *Journal of Alloys and Compounds,* vol. 817, 2020. https://doi.org/10.1016/j.jallcom.2019.152700
27. H. Wang, H. Zhao, W. Liang, S. Fan, and J. Kang, "Effect of sintering process on the electrical properties and microstructure of Ca-doped ZnO varistor ceramics," *Materials Science in Semiconductor Processing,* vol. 133, 2021. https://doi.org/10.1016/j.mssp.2021.105880
28. H. Zhao, H. Wang, X. Meng, J. Zhao, and Q. Xie, "A method to reduce ZnO grain resistance and improve the intergranular layer resistance by Ca^{2+} and Al^{3+} co-doping," *Materials Science in Semiconductor Processing,* vol. 128, 2021. https://doi.org/10.1016/j.mssp.2021.105768
29. W. Deng, Z. Q. Lei, J. L. Zhao, Y. Q. Lu, and D. K. Xiong, "Effect of Fe_2O_3 Dopant on Electronic Densities and Electrical Properties of ZnO-Based Varistors," *Advanced Materials Research,* vol. 415-417, pp. 1042-1045, 2011. https://doi.org/10.4028/www.scientific.net/AMR.415-417.1042
30. M. Peiteado, A. M. Cruz, Y. Reyes, J. De Frutos, D. G. Calatayud, and T. Jardiel, "Progressive degradation of high voltage ZnO commercial varistors upon Fe_2O_3 doping," *Ceramics International,* vol. 40, no. 8, pp. 13395-13400, 2014. https://doi.org/10.1016/j.ceramint.2014.05.057
31. J. Shen *et al.*, "Effects of Fe and Al co-doping on the leakage current density and clamp voltage ratio of ZnO varistor," *Journal of Alloys and Compounds,* vol. 747, pp. 1018-1026, 2018. https://doi.org/10.1016/j.jallcom.2018.03.106

32. Z. Peng *et al.*, "Influence of Fe_2O_3 doping on microstructural and electrical properties of ZnO–Pr6O11 based varistor ceramic materials," *Journal of Alloys and Compounds,* vol. 508, no. 2, pp. 494-499, 2010.
https://doi.org/10.1016/j.jallcom.2010.08.100

Arrived: 29. 09. 2022
Accepted: 09. 11. 2022

Original scientific paper
https://doi.org/10.33180/InfMIDEM2022.403

Informacije MIDEM
Journal of Microelectronics,
Electronic Components and Materials
Vol. 52, No. 4(2022), 227 – 237

VD-EXCCII Based Mixed Mode Biquadratic Universal Filter Employing Grounded Capacitors

Ramesh Mishra[1], Ganga Ram Mishra[2], Mohammad Faseehuddin[3], Jahariah Sampe[4]

[1]Department of Electronics, Dr. Rammanohar Lohia Avadh University
[2]Department of Physics & Electronics, Dr. Rammanohar Lohia Avadh University
[3]Department of Electronics and Telecommunication, Symbiosis Institute of Technology (SIT), Symbiosis International University (SIU), Lavale, Mulshi, Pune, Maharashtra, India
[4]Institute of Microengineering and Nanoelectronics (IMEN), Universiti Kebangsaan Malaysia (UKM), Level 4 MINES Lab, UKM 43600 Bangi, Selangor, Malaysia

Abstract: A recently developed active building block (ABB), namely Voltage Differencing Extra X current conveyor (VD-EXCCII), is used to design an electronically tunable mixed-mode universal filter. The filter provides low pass (LP), high pass (HP), band pass (BP), band reject (BR), and all pass (AP) responses in voltage-mode (VM), current-mode (CM), trans-impedance-mode (TIM), and trans-admittance-mode (TAM). The filter employs two VD-EXCCIIs, three resistors, and two capacitors. The attractive features of the filters include: (i) ability to operate in all four modes, (ii) use of grounded capacitors, (iii) tunability of Q factor independent of pole frequency, (iv) low output impedance for VM and TIM mode, (v) high output impedance explicit current output for CM and TAM and (vi) no requirement for double/negative input signals (voltage/current) for response realization. The VD-EXCCII and its layout is designed and validated in Cadence virtuoso using 0.18µm process design kit (PDK) at supply voltage of ±1.25 V. The operation of filter is examined at 16.42 MHz frequency. The non-ideal gain and sensitivity analysis is also carried out to study the effect of process and components spread on the filter performance. The obtained results bear a close resemblance with the theoretical findings.

Keywords: Analog signal processing; mixed-mode filter; current conveyor; VD-EXCCII

VD-EXCCII na osnovi mešanega načina bikvadratičnega univerzalnega filtra, ki uporablja ozemljene kondenzatorje

Izvleček: Nedavno razviti aktivni gradnik (ABB), in sicer napetostni diferenčni pretvornik Extra X (VD-EXCCII), se uporablja za zasnovo elektronsko nastavljivega univerzalnega filtra z mešanim načinom delovanja. Filter omogoča odzive nizke prepustnosti (LP), visoke prepustnosti (HP), pasovne prepustnosti (BP), pasovne zavrnitve (BR) in vse prepustnosti (AP) v napetostnem (VM), tokovnem (CM), trans-impedančnem (TIM) in trans-admitančnem (TAM) načinu. Filter uporablja dva VD-EXCCII, tri upore in dva kondenzatorja. Privlačne lastnosti filtrov so: (i) možnost delovanja v vseh štirih načinih, (ii) uporaba ozemljenih kondenzatorjev, (iii) nastavljivost faktorja Q neodvisno od frekvence polov, (iv) nizka izhodna impedanca za način VM in TIM, (v) visoka izhodna impedanca z eksplicitnim izhodnim tokom za CM in TAM ter (vi) ni potrebe po dvojnih/negativnih vhodnih signalih (napetost/tok) za realizacijo odziva. VD-EXCCII in njegova postavitev sta zasnovana in potrjena v Cadence virtuoso z uporabo 0,18µm kompleta za načrtovanje procesov (PDK) pri napajalni napetosti ±1,25 V. Delovanje filtra je preverjeno pri frekvenci 16,42 MHz. Izvedena je tudi analiza neidealnega ojačanja in občutljivosti, da bi preučili vpliv razširjenosti procesa in komponent na delovanje filtra. Dobljeni rezultati so zelo podobni teoretičnim ugotovitvam.

Ključne besede: Obdelava analognih signalov; filter v mešanem načinu; tokovni transporter; VD-EXCCII

** Corresponding Author's e-mail: rameshmishra1985@gmail.com*

How to cite:
R. Mishra et al., "VD-EXCCII Based Mixed Mode Biquadratic Universal Filter EmployingGrounded Capacitors", Inf. Midem-J. Microelectron. Electron. Compon. Mater., Vol. 52, No. 4(2022), pp. 227–237

1 Introduction

Recently, the Current-mode active building blocks (ABBs) are widely used for analog signal processing applications. The CM ABBs show greater linearity, wide bandwidth, simple structure, low power consumption, and enhanced dynamic range [1-6]. The universal frequency filters find a broad application spectrum in communication, control, instrumentation, data acquisition systems (in the analog front-end), biomedical signal processing, oscillator design, etc. [1, 2, 5, 7]. With the advancement of technology, mixed-mode systems are being developed, requiring interaction between CM and VM circuits. This task can be accomplished by TAM and TIM filters that not only perform signal processing, but also provide interfacing between VM and CM systems by acting as a bridge [8, 9]. The development of mixed-mode universal filters that can provide LP, HP, BP, BR, and AP filter functions in CM, VM, TAM, and TIM modes of operation is needed for mixed-signal system implementation.

Several designs of single-input multi-output (SIMO) and multi-input single-output (MISO) mixed-mode filters have been proposed in the literature that employ CM ABBs. A detailed comparison of the MISO filters with the proposed design is presented in Table 1, based on the following important measures of comparison: (i) number of CM-ABBs employed, (ii) the number of passive components needed, (iii) employment of all

Table 1: Comparative study of the state-of-the-art MISO Mixed mode filter designs with the proposed filter

References	Mode of Operation	(i)	(ii)	(iii)	(iv)	(v)	(vi)	(vii)	(viii)	(ix)	(x)	(xi)
[10]	MISO	6-OTA	2C	Yes	N.A.	No	No	No	Yes	Yes	Yes	-
[6]	MISO	7-CCII	2C+8R	No	Yes	No	Yes	No	Yes	Yes	No	-
[11]	MISO	3-CCII	3C+4R+ 2-switch	No	No	No	Yes	No	Yes	Yes	No	-
[12]	MISO	4-OTA	2C	Yes	N.A.	No	No	No	Yes	Yes	Yes	2.25 MHz
[17]	MISO	5-OTA	2C	Yes	N.A.	No	Yes	No	Yes	No	Yes	1.59 MHz
[35]	MISO	2-MOCCCII	2C+2R	No	Yes	Yes	Yes	No	Yes	Yes	Yes	1.27 MHz
[38]	MISO	CFOA	2C+3R	No	No	Yes	No	No	Yes	No	No	12.7MHz
[20]	MISO	4-MOCCCII	2C	Yes	N.A.	No	Yes	Yes	Yes	No	Yes	-
[37]	MISO	1-FDCCII	2C+2R	No	Yes	No	No	No	Yes	Yes	No	10 MHz
[43]	MISO	2-VDTA	2C	Yes	N.A	Yes	No	No	Yes	Yes	Yes	1 MHz
[30]	MISO	1-FDCCII+1-DDCC	2C+6R	No	Yes	Yes	Yes	No	Yes	No	No	1.59 MHz
[29]	MISO	5-DVCC	2C+5R	Yes	Yes	Yes	Yes	No	Yes	Yes	No	1MHz
[45]	MISO	4-CCII	2C+4R	Yes	Yes	Yes	No	No	Yes	Yes	No	31.8 MHz
[26]	MISO	5-OTA	2C	Yes	Yes	Yes	Yes	No	Yes	Yes	Yes	3.390 MHz
[27]	MISO	3-DDCC	2C+4R	No	Yes	No	Yes	No	Yes	Yes	No	3.978 MHz
[45]	MISO	1-EXCCCII	2C	No	N.A.	Yes	No	No	Yes	No	Yes	23 MHz
[47]	MISO	4-ZC-CCTA	2C	No	N.A.	No	Yes	No	Yes	No	Yes	7.5 MHz
[40]	MISO	2-EXCCTA	2C+4R	No	Yes	Yes	Yes	No	Yes	Yes	Yes	7.622 MHz
[42]	MISO	2-VD-DVCC	2C+3R	No	Yes	Yes	Yes	No	Yes	Yes	Yes	5.305 MHz
[44]	MISO	2-VDBA	2C+2R	No	Yes	Yes	No	Yes	No	Yes	Yes	1.52 MHz
[41]	MISO	1-VD-EXCCII	2C+2R	No	Yes	Yes	Yes	No	Yes	Yes	Yes	8.08 MHz
This Works	MISO	2-VD-EXCCII	2C+3R	No	Yes	Yes	Yes	No	Yes	Yes	Yes	16.42 MHz

*Full nomenclature of the mentioned ABBs in Tables 1 in alphabetical order: CCII: Second-generation current conveyor, CFOA: Current feedback operational amplifier, DDCC: Differential difference current conveyor, DVCC: Differential voltage current conveyor, EXCCCII: Extra x current controlled current conveyor, EXCCTA: Extra x Current conveyor transconductance amplifier, FDCCII: Fully differential second-generation current conveyor, MOCCCII: Multi output current controlled current conveyor, OTA: Operational transconductance amplifier, VD-DVCC: Voltage differencing differential voltage current conveyor, VDBA: Voltage differencing buffered amplifier, VDTA: Voltage differencing transconductance amplifier, ZC-CCTA: Z copy-current conveyor transconductance amplifier.
**N.A.-Not applicable

grounded passive components, (iv) no requirement for resistive matching except for obtaining AP response, (v) provision to control quality factor (Q) independent of the centre frequency, (vi) ability to provide all five filter responses in all four modes of operation, (vii) low output impedance for VM and TIM modes, (viii) availability of explicit current output in CM and TAM, (ix) no requirement for double/negative input signals (voltage/current), (x) inbuilt tunability, and (xi) test frequency. The MISO filter structures [3, 6, 8-29] employ ABBs in excess of two. The filter structures in [3, 6, 9, 11, 18, 21, 27, 29-32] require more than five passive components. The filter designs in [3, 6, 9, 11, 18, 21, 27, 30-42] do not employ all grounded passive components. The filters in [3, 6, 9-12, 16, 17, 20, 23, 24, 27, 30, 33, 36-39] do not provide quality factor tuning independent of frequency. The filter structures [6, 8, 10, 12-14, 16, 19, 21, 23, 28, 32, 33, 36-38, 43, 44] do not provide all five filter responses in VM, CM, TAM, and TIM operation. The filter structures [3, 6, 9, 11, 14, 18, 21, 27-34, 37-39] lack inbuilt tunability. The literature survey shows that a limited number of truly mixed-mode filters are available, and additional novel mixed-mode filter structures are needed to fill this technological void.

In this research, Voltage Differencing Extra X current conveyor (VD-EXCCII) is utilized to design mixed-mode filters. The design requires two VD-EXCCIIs, two capacitors, and three resistors. The striking features of the proposed filter are: (i) ability to work in all four modes of operation, (ii) provision for inbuilt tunability, (iii) the filter enjoy low active and passive sensitivities, and (iv) use of all grounded capacitors. Besides these, the filters enjoy all the properties (iv-x) mentioned in Table 2. The design of the VD-EXCCII is done in Cadence Virtuoso using 0.18µm PDK. The simulation results are in close agreement with the theoretical predictions.

2 Voltage differencing extra X current conveyor (VD-EXCCII)

The proposed Voltage Differencing Extra X current conveyor (VD-EXCCII) is derived by connecting extra X second generation current conveyor (EXCCII) [46] and operational transconductance amplifier (OTA). The first stage comprises OTA followed by the CCII with two current input terminals. The developed active element has characteristics of CCII and tunable OTA in one structure. The voltage-current (V-I) characteristics of the developed VD-EXCCII are presented in Equations (2.1-2.4) and the block diagram is presented in Fig. 1.

$$I_W = I_{WC+} = -I_{WC-} = g_m\left(V_P - V_N\right), \tag{2.1}$$

$$V_{XP} = V_{XN} = V_W, \tag{2.2}$$

$$I_{XP} = I_{ZP+} = -I_{ZP-}, \tag{2.3}$$

$$I_{XN} = I_{ZN+} = -I_{ZN-}. \tag{2.4}$$

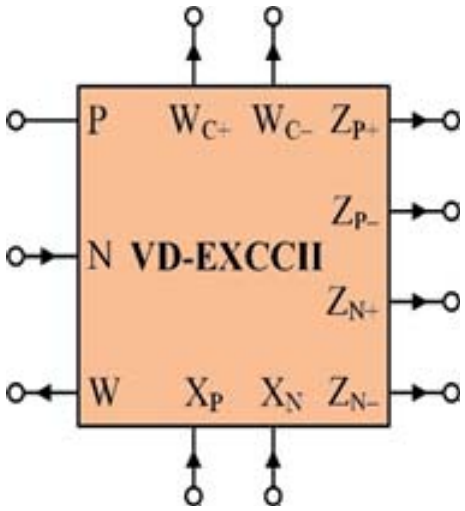

Figure 1: Block Diagram of VD-EXCCII

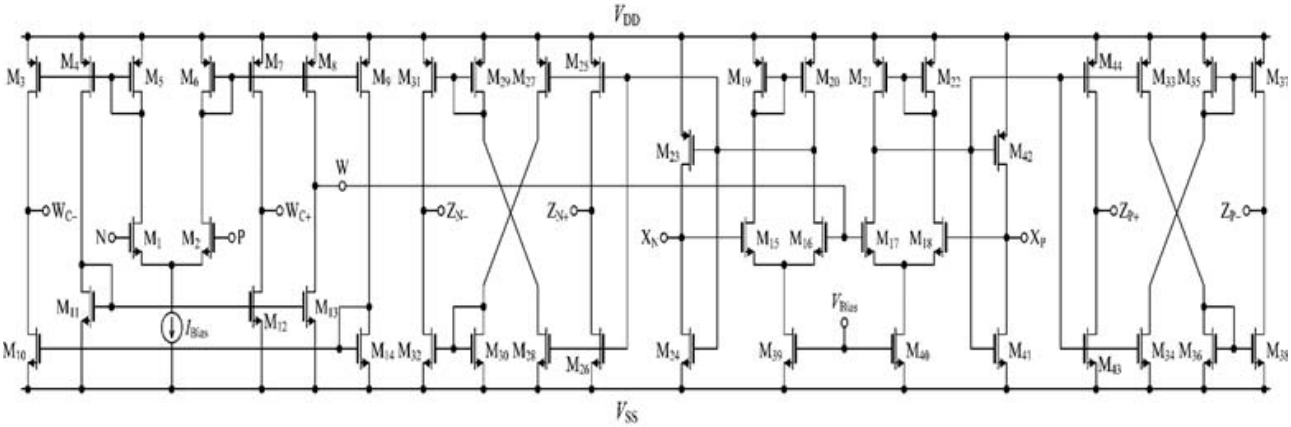

Figure 2: CMOS implementation of VD-EXCCII

The CMOS implementation of VD-EXCCII is given in Figure 2. The first stage consists of OTA MOS transistors (M1-M14). The output current of the OTA depends on the voltage difference ($V_P - V_N$). Assuming that all transistors are operating in saturation region and transistors (M1-M2) have equal width to length ratio, the output current is given by Equation 2.5. The second stage is made up of hybrid voltage and current followers (M15-M44). The voltage developed at node W is transferred to nodes X_P and X_N. In the same way, the input current from X_P node is transferred to Z_{P+} and Z_{P-}. Furthermore, the input current from X_N node is transferred to Z_{N+} and Z_{N-}. The current following in Z_N and Z_P terminals are independent of each other. The class AB output stage is utilized in the output stage as it is suitable for low voltage operation and better dynamic range [2].

$$I_W = I_{WC+} = -I_{WC-} = g_{mi}\left(V_P - V_N\right) = \left(\sqrt{2I_{Bias}K_i}\right)\left(V_P - V_N\right), \quad (2.5)$$

$K_i = \mu C_{ox} W/2L$, (i = 1, 2) is the transconductance parameter, W is the effective channel width, L is the effective length of the channel, C_{ox} is the gate oxide capacitance per unit area and μ is the carrier mobility.

3 Proposed electronically tunable mixed-mode universal filter

The proposed filter, as shown in Fig. 3, requires two VD-EXCCIIs, two capacitors, and three resistors. The filter offers low output impedance for VM and TIM mode of operation. In addition, the CM and TAM responses are available from explicit high impedance terminals. Furthermore, the capacitors are connected to high impedance terminals to absorb the parasitics associated with the terminals. Among the three resistors, two are connected to the low resistance X terminals to accommodate the parasitic resistance. The main drawback of the filter is the use of two floating resistors, but given the advantages of the filter, this can be accommodated. Moreover, floating resistors can be easily implemented in CMOS technology. The important features of the filter include: (i) ability to provide all five filter responses in all four modes of operation, (ii) employment of a minimum number of passive components, (iii) use of grounded capacitors, (iv) no requirement for resistive matching except for AP response, (v) low output impedance in VM and TIM configuration, (vi) no need for capacitive matching, (vii) availability of explicit current output in CM and TAM, (viii) no requirement for double/negative input signals (voltage/current), (xi) independent control of Q and f_0 and (xi) inbuilt tunability. The operation of the filter in all modes is explained below.

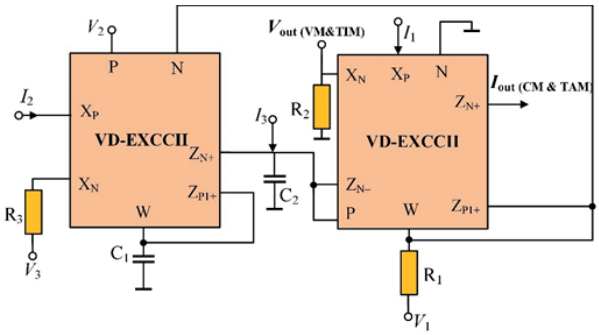

Figure 3: Proposed Mixed-mode Filter

3.1 Operation in VM and TAM mode

In this mode of operation, the inputs currents ($I_1 - I_3$) are set to zero. The filter is excited with input voltages ($V_1 - V_3$) as per the sequence given in Table 2. The transfer functions for VM/TAM and expressions for quality factor and pole frequency are given in Equations (3.1-3.4).

$$V_{out(VM)} = \frac{s^2 C_1 C_2 R_2 R_3 V_1 - sC_1 g_{m1} R_2 R_1 V_3 + R_1 g_{m1} R_2 g_{m2} V_2}{s^2 C_1 C_2 R_2 R_3 + sC_1 g_{m1} R_3 R_1 + R_1 g_{m1} R_2 g_{m2}} \quad (3.1)$$

For all pass response, a simple resistive matching of ($R_3 = R_2$) is required, which is easy to achieve.

$$I_{out\,(\mathrm{TAM})} = \frac{V_{out(VM)}}{R_2} = \\ = \frac{1}{R_2} * \left[\frac{s^2 C_1 C_2 R_2 R_3 V_1 - sC_1 g_{m1} R_2 R_1 V_3 + R_1 g_{m1} R_2 g_{m2} V_2}{s^2 C_1 C_2 R_2 R_3 + sC_1 g_{m1} R_3 R_1 + R_1 g_{m1} R_2 g_{m2}}\right], \quad (3.2)$$

$$f_0 = \frac{1}{2\pi}\sqrt{\frac{g_{m1} g_{m2} R_1}{C_1 C_2 R_3}}, \quad (3.3)$$

$$Q = R_2\sqrt{\frac{C_2 g_{m2}}{C_1 g_{m1} R_1 R_3}}. \quad (3.4)$$

Table 2: Excitation Sequence for VM and TAM

Response	Inputs			Matching Condition	Filter Gain Constants
	V_1	V_2	V_3		
LP	0	1	0	No	1
HP	1	0	0	No	1
BP	0	0	1	No	1
BR	1	0	1	No	1
AP	1	1	1	$R_2 = R_3$	1

3.2 Operation in CM and TIM mode:

In this mode of operation, all input voltages ($V_1 - V_3$) are set to zero. The input currents ($I_1 - I_3$) are applied

according to Table 3. The transfer functions for TIM and CM are given in Equations (3.5) and (3.6).

$$V_{out(TIM)} = R_1\left[\frac{-s^2C_1C_2R_2R_3I_1 + sC_1R_3g_{m1}R_2I_3 - g_{m1}R_2I_2}{s^2C_1C_2R_2R_3 + sC_1g_{m1}R_3R_1 + R_1g_{m1}R_2g_{m2}}\right] \quad (3.5)$$

$$I_{out\,(CM)} = \frac{V_{out(TIM)}}{R_2} = \frac{R_1}{R_2}\left[\frac{-s^2C_1C_2R_2R_3I_1 + sC_1R_3g_{m1}R_2I_3 - g_{m1}R_2I_2}{s^2C_1C_2R_2R_3 + sC_1g_{m1}R_3R_1 + R_1g_{m1}R_2g_{m2}}\right] \quad (3.6)$$

In Equation 3.6 for $R_1 = R_2$ the filter gain constants are $H_{oHP} = 1,\ H_{oLP} = \frac{1}{R_1g_{m2}}, H_{oBP} = 1$ by adjusting these parameters the filter gain can be adjusted.

Table 3: Input current excitation sequence

Response	Inputs			Matching Condition	Filter Gain Constants
	I_1	I_2	I_3		
LP	0	1	0	No	$\frac{1}{R_1g_{m2}}$
HP	1	0	0	No	1
BP	0	0	1	No	1
BR	1	1	0	No	1
AP	1	1	1	$g_{m1}R_2 = 1$, $R_2 = R_1$	1

4 Non-ideal gain and sensitivity analysis

The non-ideal effects that influence the response of the VD-EXCCII are the frequency-dependent non-ideal current ($\alpha_{P/N}$, $\alpha'_{P/N}$), voltage ($\beta_{P/N}$), and transconductance transfer (γ, $\gamma\rangle$) gains. These non-ideal gains result in a change in the current and voltage signals during transfer leading to an undesired response. Taking into account the non-ideal gains, the V-I characteristics of the VD-EXCCII in (3.1-3.4) will be modified as follows: $I_W = 0$, $V_{XP} = \beta_P V_W$, $V_{XN} = \beta_N V_W$, $I_{ZP+} = \alpha_p I_{XP}$, $I_{ZP-} = -\alpha'_p I_{XP}$, $I_{ZN+} = \alpha_N I_{XN}$, $I_{ZN-} = \alpha'_N I_{XN}$, $I_W = I_{WC+} = \gamma g_m(V_P - V_N)$, $I_{WC-} = -\gamma' g_m(V_P - V_N)$, where $\beta_{Pm} = 1 - \varepsilon_{vPm}$, $\beta_{Nm} = 1 - \varepsilon_{vNm}$, $\alpha_{Pm} = 1 - \varepsilon_{iPm}$, $\alpha_{Nm} = 1 - \varepsilon_{iNm}$, $\gamma_m = 1 - \varepsilon_{g_mm}$, and $\gamma'_m = 1 - \varepsilon'_{g_mm}$, for $m = 1, 2$, which refers to the number of VD-EXCCIIs. Here, ε_{vPm}, ε_{vNm}($|\varepsilon_{vPm}|$, $|\varepsilon_{vNm}|$«1) denote voltage tracking error, ε_{iPm}, ε_{iNm} ($|\varepsilon_{iPm}|$, $|\varepsilon_{iNm}|$«1), denote current tracking errors, and ε_{g_mm}, , $\varepsilon\rangle_{g_mm}$ ($|\varepsilon_{g_mm}|$, $|\varepsilon\rangle_{g_mm}|$«1) denote transconductance errors of the VD-EXCCII.

The non-ideal analysis considering the effect of non-ideal current, voltage, and transconductance transfer gains is carried out for (VM, CM, TAM and TIM) configurations to see its effect on the transfer function, f_0, and Q of the proposed filter. The modified expressions of filter transfer functions, f'_0, and Q' are presented in Equations (4.1) to (4.6). The procedure to perform the non-ideal analysis can be found in [42].

$$V'_{out(VM-Mode)} = \left[\frac{s^2C_1C_2R_2R_3V_1 - s\alpha_{N1}\gamma_1g_{m1}R_1R_2C_1V_3 + V_2\alpha_{N1}\beta_{N1}\gamma_1\gamma_2g_{m1}g_{m2}R_1R_2}{s^2C_1C_2R_2R_3 + \alpha'_{N2}\beta_{N2}\gamma_1g_{m1}SC_1R_3R_1 + \alpha_{N1}\beta_{N1}\gamma_1\gamma_2g_{m1}g_{m2}R_1R_2}\right] \quad (4.1)$$

$$I'_{out(TAM-Mode)} = \frac{\alpha_{N2}\beta_{N2}}{R_2}\left[\frac{s^2C_1C_2R_2R_3V_1 - s\alpha_{N1}\gamma_1g_{m1}R_1R_2C_1V_3 + V_2\alpha_{N1}\beta_{N1}\gamma_1\gamma_2g_{m1}g_{m2}R_1R_2}{s^2C_1C_2R_2R_3 + \alpha'_{N2}\beta_{N2}\gamma_1g_{m1}SC_1R_3R_1 + \alpha_{N1}\beta_{N1}\gamma_1\gamma_2g_{m1}g_{m2}R_1R_2}\right] \quad (4.2)$$

$$I'_{out(CM-Mode)} = \frac{\alpha_{N2}\beta_{N2}R_1}{R_2}\left[\frac{-s^2C_1C_2R_2R_3\alpha_{P2}I_1 + sC_1R_3\gamma_1g_{m1}R_2I_3 - \alpha_{P1}\alpha_{N1}\beta_{N1}g_{m1}R_2I_2}{s^2C_1C_2R_2R_3 + \alpha'_{N2}\beta_{N2}\gamma_1g_{m1}SC_1R_3R_1 + \alpha_{N1}\beta_{N1}\gamma_1\gamma_2g_{m1}g_{m2}R_1R_2}\right] \quad (4.3)$$

$$V'_{out(TIM-Mode)} = R_1\left[\frac{-s^2C_1C_2R_2R_3\alpha_{P2}I_1 + sC_1R_3\gamma_1g_{m1}R_2I_3 - \alpha_{P1}\alpha_{N1}\beta_{N1}g_{m1}R_2I_2}{s^2C_1C_2R_2R_3 + \alpha'_{N2}\beta_{N2}\gamma_1g_{m1}SC_1R_3R_1 + \alpha_{N1}\beta_{N1}\gamma_1\gamma_2g_{m1}g_{m2}R_1R_2}\right] \quad (4.4)$$

$$f'_0 = \frac{1}{2\pi}\sqrt{\frac{\alpha_{N1}\beta_{N1}\gamma_1\gamma_2g_{m1}g_{m2}R_1}{C_1C_2R_3}} \quad (4.5)$$

$$Q' = \frac{R_2}{\alpha'_{N2}\beta_{N2}}\sqrt{\frac{\alpha_{N1}\beta_{N1}\gamma_2C_2g_{m2}}{\gamma_1C_1g_{m1}R_1R_3}} \quad (4.6)$$

The sensitivities of ω'_0 and Q' with respect to the non-ideal gains and passive components are given below in Equations (4.7) to (4.9).

$$S^{\omega'_o}_{g_{m1}} = S^{\omega'_o}_{g_{m2}} = S^{\omega'_o}_{R_1} = S^{\omega'_o}_{\alpha_{N1}} = S^{\omega'_o}_{\beta_{N1}} = S^{\omega'_o}_{\gamma_2} = S^{\omega'_o}_{\gamma_1} = -S^{\omega'_o}_{C_1} = -S^{\omega'_o}_{C_2} = -S^{\omega'_o}_{R_3} = \frac{1}{2} \tag{4.7}$$

$$S^{Q'}_{\alpha_{N1}} = S^{Q'}_{\beta_{NI}} = -S^{Q'}_{C_1} = S^{Q'}_{\gamma_2} = S^{Q'}_{g_{m2}} = S^{Q'}_{C_2} = -S^{Q'}_{g_{m1}} = -S^{Q'}_{R_1} = -S^{Q'}_{R_3} = -S^{Q'}_{\gamma_1} = \frac{1}{2}, \tag{4.8}$$

$$S^{Q'}_{R_2} = -S^{Q'}_{\alpha'_{N2}} = -S^{Q'}_{\beta_{N2}} = 1 \tag{4.9}$$

The sensitivities are low and have absolute values not higher than unity.

5 Simulation and validation

To verify the proposed mixed-mode filter, it is designed and simulated in Cadence virtuoso design software. The newly proposed VD-EXCCII is designed in 0.18 µm Silterra Malaysia technology at ±1.25V supply voltage. The widths and lengths of the transistors are given in Table 4. The bias current of the OTA is fixed at 120 µA resulting in a transconductance of 1.0321 µS. The layout of the VD-EXCCII Fig. 4 is drawn using the nhp and php high-performance MOS transistors from the Silterra library. The layout occupies a total area of 54.28*22.80µm^2.

The filter is designed for centre frequency of 16.4263 MHz and a quality factor of one by selecting passive component as $R_1 = R_2 = R_3$ =1 kΩ, $C_1 = C_2$ = 10pF and g_m = 1.0321 µS. All five filter responses in VM, CM, TAM, and TIM modes are presented in Figs. 5-12. The simulated frequency for VM-AP is found to be 15.977 MHz leading to a 2.73% error.

Table 4: Width and Length of the MOS transistors

Transistors	Width (µm)	Length (µm)
M1–M2, M5–M6	1.8	0.36
M3–M4, M7–M9	5.7	0.36
M10–M14	1.8	0.72
M15–M18	3.06	0.36
M19–M22	10	0.36
M23, M25, M27, M33, M42, M44	2.16	0.36
M24, M26, M28, M32, M34, M30, M38, M36, M41, M43	0.72	0.72
M21, M31, M35, M37	1.08	0.72

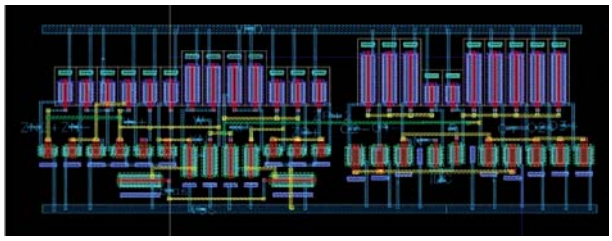

Figure 4: Layout of the VD-EXCCII

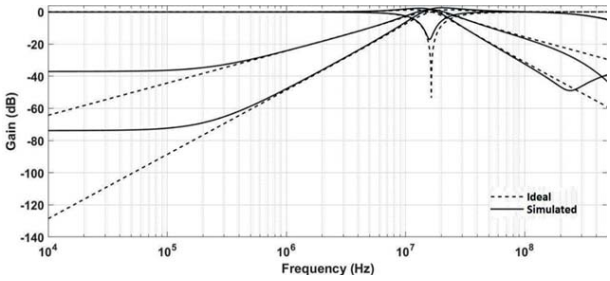

Figure 5: VM MISO configuration: Frequency responses of the LP, BP, HP, and BR filter

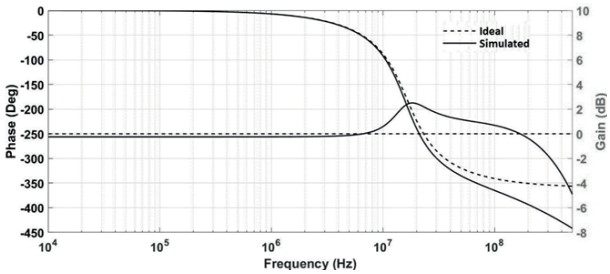

Figure 6: VM MISO configuration: Gain and phase responses of the AP filter

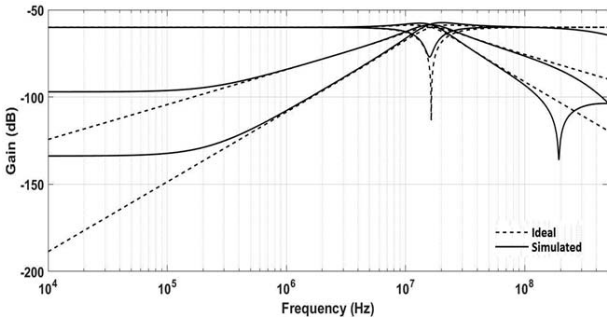

Figure 7: TAM MISO configuration: Frequency responses of the LP, BP, HP, and BR filter

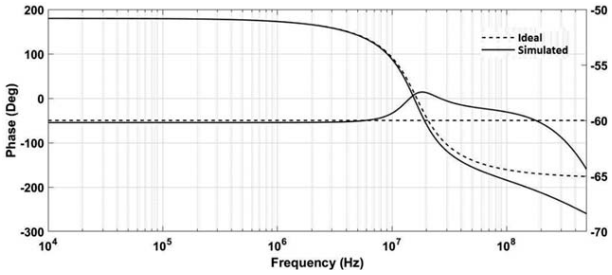

Figure 8: TAM MISO configuration: Gain and phase responses of the AP filter

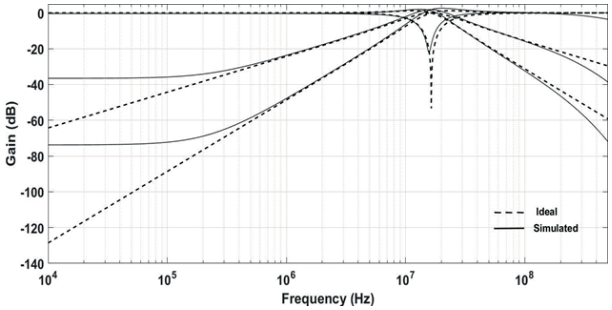

Figure 9: CM MISO configuration: Frequency responses of the LP, BP, HP, and BR filter

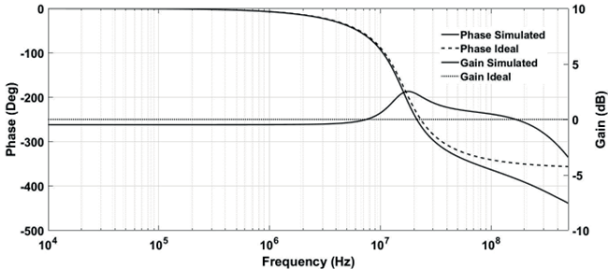

Figure 10: CM MISO configuration: Gain and phase responses of the AP filter

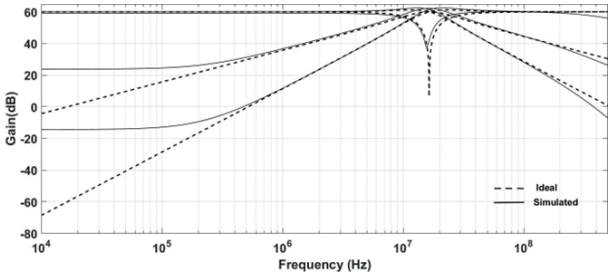

Figure 11: TIM MISO configuration: Frequency responses of the LP, BP, HP, and BR filter

To examine the signal processing capability of the proposed universal filter, the transient analysis is carried out in VM mode for HP, LP, BR, and BP responses. A VM sinusoidal signal of 100 mVp-p and 16.42 MHz frequency is applied at the input and the output is analyzed as presented in Fig. 13. Similarly, a CM sinusoidal signal of 50 µA p-p and 16.42 MHz frequency is applied at the input, and the BP output in CM is observed as shown in Fig. 14. In the presented filter, the quality factor can be set independently of the pole frequency of the filter. The tunability of the quality factor is verified by analysing BP response in VM for different values of resistor R_2as shown in Fig. 15. It can be inferred from the figure that the quality factor of the filter can be tuned independently of the frequency. The frequency tuning is verified by varying the bias current of the OTAs and observing the CM-BP and VM-LP responses. It can be deduced that the frequency can be tuned without disturbing the Quality factor of the filter as presented in Fig. 16-17.

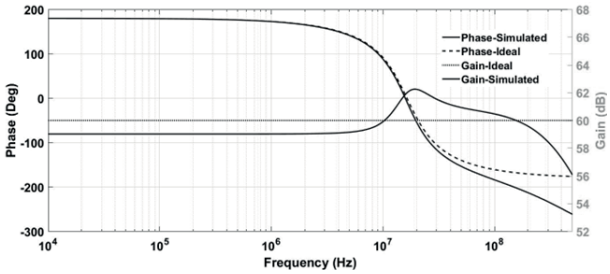

Figure 12: TIM MISO configuration: Gain and phase responses of the AP filter

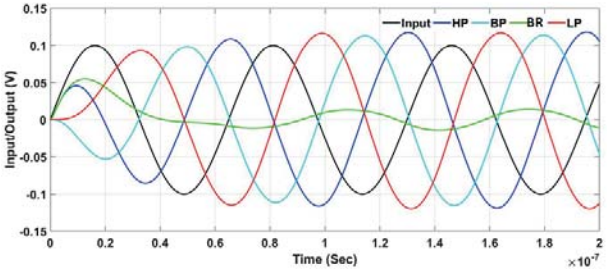

Figure 13: VM MISO configuration: Transient analysis results for BP, HP, LP, and BR filter configurations

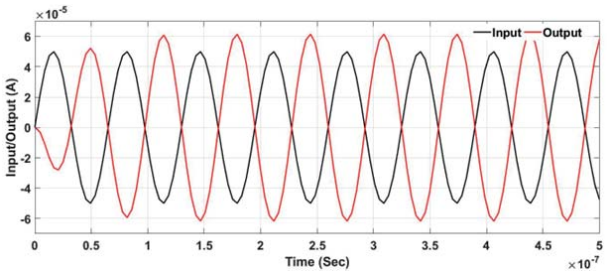

Figure 14: CM MISO configuration: Transient analysis results for BP filter configuration

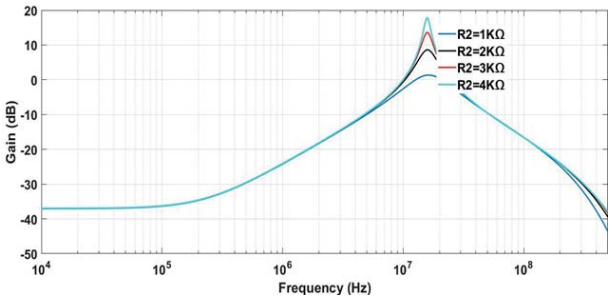

Figure 15: VM MISO configuration: Quality factor tuning for different resistor values in BP filter

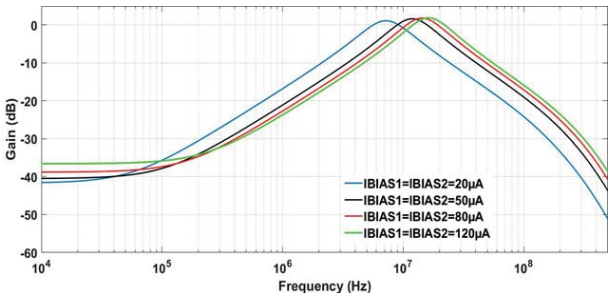

Figure 16: CM MISO configuration: Frequency tuning for different bias current (I_{Bias1} and I_{Bias2}) values in BP filter

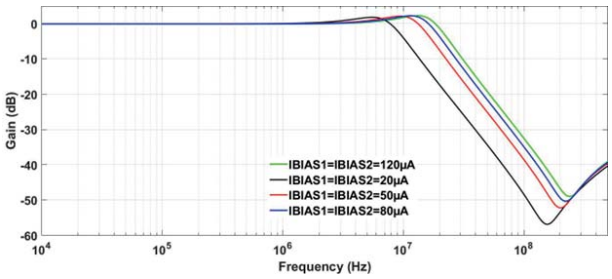

Figure 17: VM MISO configuration: Frequency tuning for different bias current (I_{Bias1} and I_{Bias2}) values in LP filter

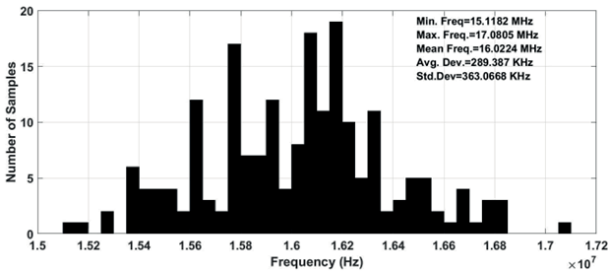

Figure 18: VM MISO configuration: The Monte Carlo analysis result for BP response

To study the effect of process spread on the performance of the designed filter, Monte Carlo analysis is carried out for 200 runs. The Monte Carlo analysis results for VM-BP response are given in Fig. 18 and 19. The results for CM-AP configuration is given in Fig. 20.

The total harmonic distortion (THD) of the filter for VM-BP response is plotted for different input signal values, as shown in Fig. 21. The THD plot for CM-BP and CM-LP is presented in Fig. 22. The THD remains within acceptable limits (≤5%) for the appreciable input range.

The input and output noise of the filter for VM-LP configuration is shown in Fig. 23. The input referred noise magnitude in the pass band of VM-LP is found in the range of 2.914E-08 $V/Hz^{1/2}$. The magnitude of output referred noise is in the range of 3.425E-08 $V/Hz^{1/2}$.

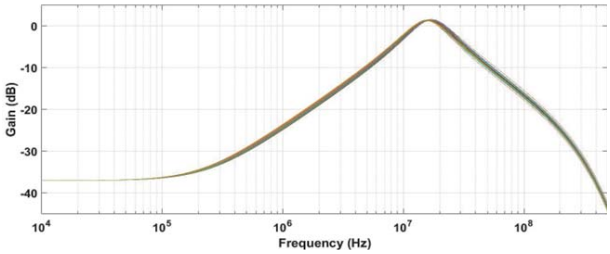

Figure 19: VM MISO configuration: The Monte Carlo analysis result for BP configuration

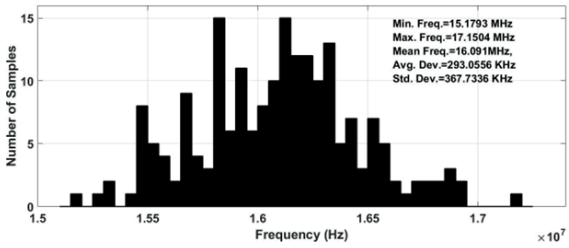

Figure 20: CM MISO configuration: The Monte Carlo analysis result for AP response

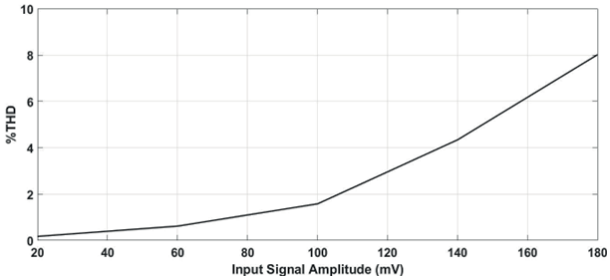

Figure 21: Total harmonic distortion for VM-BP

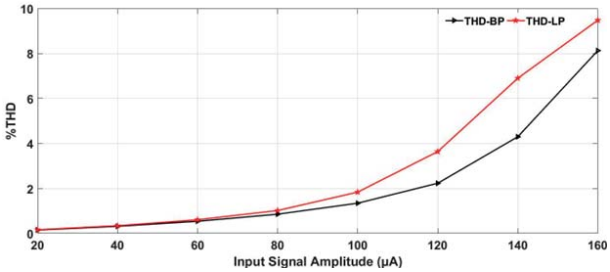

Figure 22: Total harmonic distortion for CM-BP & CM-LP

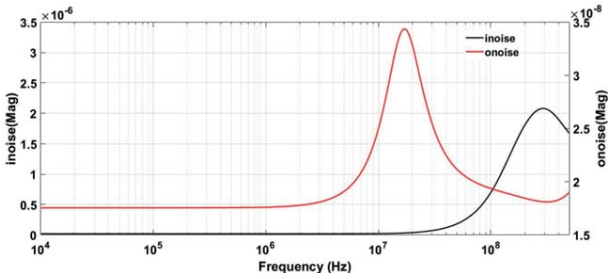

Figure 23: Input and Output referred noise

6. Conclusion

This paper presents a new VD-EXCCII based electronically tunable mixed-mode filter. The filter employs two VD-EXCCIIs, three resistors, and two grounded capacitors. The presented MISO filter has inbuilt tunability and can realize all five filter responses in all four modes of operation (VM, CM, TAM, and TIM). Detailed theoretical analysis and non-ideal gain analysis are done. The VD-EXCCII is designed in Cadence Virtuoso software and extensive simulations are carried out to examine and validate the proposed filter in all four modes of operation. The proposed filter has all the advantages mentioned in Table 2 (iv)-(x). The filter is designed for a frequency of 16.42 MHz at ±1.25 V power supply. The Monte Carlo analysis shows that the frequency deviation is within acceptable limits. Furthermore, the THD is within 5% for a considerable voltage/current input signal range. The simulation results are found consistent with the theoretical predictions.

7 Conflict of interest

Authors declare no conflict of interest

8 Acknowledgement

This work is funded by UKM Internal grant and PAME SDN BHD Industry grant under the grants GUP-2022-069 and RR-2022-001 respectively.

9 References

1. P. A. Mohan, *Current-mode VLSI analog filters: design and applications*: Springer Science & Business Media, 2003.
2. G. Ferri and N. C. Guerrini, *Low-voltage low-power CMOS current conveyors*: Springer Science & Business Media, 2003.
3. R. Senani, "Novel mixed-mode universal biquad configuration," *IEICE Electronics Express,* vol. 2, pp. 548-553, 2005.
4. F. Mohammad, J. Sampe, S. Shireen, and S. H. M. Ali, "Minimum passive components based lossy and lossless inductor simulators employing a new active block," *AEU-International Journal of Electronics and Communications,* vol. 82, pp. 226-240, 2017.
5. R. Raut and M. Swamy, *Modern analog filter analysis and design: a practical approach*: John Wiley & Sons, 2010.
6. M. T. Abuelma'atti and A. Bentrcia, "A novel mixed-mode CCII-based filter," *Active and Passive Electronic Components,* vol. 27, pp. 197-205, 2004.
7. R. Senani, D. Bhaskar, and A. Singh, *Current conveyors: variants, applications and hardware implementations* vol. 560: Springer, 2015.
8. M. T. Abuelma'atti, "A novel mixed-mode current-controlled current-conveyor-based filter," *Active and passive electronic components,* vol. 26, pp. 185-191, 2003.
9. M. T. Abuelma'atti, A. Bentrcia, and S. a. M. Al-Shahrani, "A novel mixed-mode current-conveyor-based filter," *International Journal of Electronics,* vol. 91, pp. 191-197, 2004.
10. M. T. Abuelma'atti and A. Bentrcia, "A novel mixed-mode OTA-C filter," *Frequenz,* vol. 57, pp. 157-159, 2003.
11. N. Pandey, S. K. Paul, A. Bhattacharyya, and J. SB, "A new mixed mode biquad using reduced number of active and passive elements," *IEICE Electronics Express,* vol. 3, pp. 115-121, 2006.
12. M. A. Ibrahim, "Design and analysis of a mixed-mode universal filter using dual-output operational transconductance amplifiers (DO-OTAs)," in *2008 International Conference on Computer and Communication Engineering*, 2008, pp. 915-918.
13. Z. Li, "Mixed-mode universal filter using MCCCII. AEU—Int," *J. Electron. Commun,* vol. 63, pp. 1072-1075, 2009.
14. S. Minaei and M. A. Ibrahim, "A mixed-mode KHN-biquad using DVCC and grounded passive elements suitable for direct cascading," *International Journal of Circuit Theory and Applications,* vol. 37, pp. 793-810, 2009.
15. H.-P. Chen, Y.-Z. Liao, and W.-T. Lee, "Tunable mixed-mode OTA-C universal filter," *Analog Integrated Circuits and Signal Processing,* vol. 58, pp. 135-141, 2009.
16. S. Maheshwari, S. V. Singh, and D. S. Chauhan, "Electronically tunable low-voltage mixed-mode universal biquad filter," *IET circuits, devices & systems,* vol. 5, pp. 149-158, 2011.
17. C.-N. Lee, "Multiple-mode OTA-C universal biquad filters," *Circuits, Systems and Signal Processing,* vol.

29, pp. 263-274, 2010.
18. W.-B. Liao and J.-C. Gu, "SIMO type universal mixed-mode biquadratic filter," 2011.
19. M. Kumngern and S. Junnapiya, "Mixed-mode universal filter using OTAs," in *2012 IEEE International Conference on Cyber Technology in Automation, Control, and Intelligent Systems (CYBER)*, 2012, pp. 119-122.
20. N. Pandey and S. K. Paul, "Mixed mode universal filter," *Journal of Circuits, Systems and Computers,* vol. 22, p. 1250064, 2013.
21. L. Wang, C. Wang, J. Zhang, X. Liang, and S. Jiang, "A new mixed-mode filter based on MDDCCs," in *Seventh International Conference on Graphic and Image Processing (ICGIP 2015)*, 2015, p. 981717.
22. H.-P. Chen and W.-S. Yang, "Electronically tunable current controlled current conveyor transconductance amplifier-based mixed-mode biquadratic filter with resistorless and grounded capacitors," *Applied Sciences,* vol. 7, p. 244, 2017.
23. V. Chamnanphrai and W. Sa-ngiamvibool, "Electronically tunable SIMO mixed-mode universal filter using VDTAs," *Przegląd Elektrotechniczny,* vol. 93, pp. 207-211, 2017.
24. M. Parvizi, A. Taghizadeh, H. Mahmoodian, and Z. D. Kozehkanani, "A Low-Power Mixed-Mode SIMO Universal G m–C Filter," *Journal of Circuits, Systems and Computers,* vol. 26, p. 1750164, 2017.
25. U. Cini and M. Aktan, "Dual-mode OTA based biquadratic filter suitable for current-mode applications," *AEU-International Journal of Electronics and Communications,* vol. 80, pp. 43-47, 2017.
26. D. R. Bhaskar, A. Raj, and P. Kumar, "Mixed-mode universal biquad filter using OTAs," *Journal of Circuits, Systems and Computers,* vol. 29, p. 2050162, 2020.
27. C.-N. Lee and W.-C. Yang, "General Mixed-Mode Single-Output DDCC-based Universal Biquad Filter," *Int. J. Eng. Res,* vol. 9, pp. 744-749, 2020.
28. T. Ettaghzouti, N. Hassen, and K. Besbes, "Novel multi-input single-output mixed-mode universal filter employing second generation current conveyor circuit," *Sensors, Circuits & Instrumentation Systems: Extended Papers,* vol. 6, p. 53, 2017.
29. T. Tsukutani and N. Yabuki, "A DVCC-based mixed-mode biquadratic circuit," *J. Electr. Eng,* vol. 6, pp. 52-56, 2018.
30. C.-N. Lee, "Independently tunable mixed-mode universal biquad filter with versatile input/output functions," *AEU-International Journal of Electronics and Communications,* vol. 70, pp. 1006-1019, 2016.
31. C.-N. Lee, "Mixed-mode universal biquadratic filter with no need of matching conditions," *Journal of Circuits, Systems and Computers,* vol. 25, p. 1650106, 2016.
32. J.-W. Horng, C.-M. Wu, and N. Herencsar, "Current-mode and transimpedance-mode universal biquadratic filter using two current conveyors," 2017.
33. N. A. Shah and M. A. Malik, "Multifunction mixed-mode filter using FTFNs," *Analog Integrated Circuits and Signal Processing,* vol. 47, pp. 339-343, 2006.
34. C.-N. Lee and C.-M. Chang, "Single FDCCII-based mixed-mode biquad filter with eight outputs," *AEU-International Journal of Electronics and Communications,* vol. 63, pp. 736-742, 2009.
35. N. Pandey, S. K. Paul, A. Bhattacharyya, and S. Jain, "Realization of Generalized Mixed Mode Universal Filter Using CCCIIs," *Journal of Active & Passive Electronic Devices,* vol. 5, 2010.
36. S. Singh, S. Maheshwari, and D. Chauhan, "Electronically tunable current/voltage-mode universal biquad filter using CCCCTA," *International J. of Recent Trends in Engineering and Technology,* vol. 3, pp. 71-76, 2010.
37. F. Kaçar, A. Kuntman, and H. Kuntman, "Mixed-mode biquad filter employing single active element," in *2013 IEEE 4th Latin American Symposium on Circuits and Systems (LASCAS)*, 2013, pp. 1-4.
38. E. Yuce, "Fully integrable mixed-mode universal biquad with specific application of the CFOA," *AEU-International Journal of Electronics and Communications,* vol. 64, pp. 304-309, 2010.
39. B. Chaturvedi, J. Mohan, and A. Kumar, "A new versatile universal biquad configuration for emerging signal processing applications," *Journal of Circuits, Systems and Computers,* vol. 27, p. 1850196, 2018.
40. M. I. A. Albrni, F. Mohammad, N. Herencsar, J. Sampe, and S. H. M. Ali, "Novel electronically tunable biquadratic mixed-mode universal filter capable of operating in MISO and SIMO configurations," *Inf. MIDEM,* vol. 50, pp. 189-203, 2020.
41. M. Faseehuddin, N. Herencsar, M. A. Albrni, and J. Sampe, "Electronically tunable mixed-mode universal filter employing a single active block and a minimum number of passive components," *Applied Sciences,* vol. 11, p. 55, 2020.
42. M. Faseehuddin, N. Herencsar, M. A. Albrni, S. Shireen, and J. Sampe, "Electronically tunable mixed mode universal filter employing grounded capacitors utilizing highly versatile VD-DVCC," *Circuit World,* 2021.
43. A. Yeşil and F. Kaçar, "Electronically tunable resistorless mixed mode biquad filters," *Radioengineering,* vol. 22, pp. 1016-1025, 2013.
44. N. Roongmuanpha, M. Faseehuddin, N. Herencsar, and W. Tangsrirat, "Tunable Mixed-Mode Voltage Differencing Buffered Amplifier-Based Universal

Filter with Independently High-Q Factor Controllability," *Applied Sciences,* vol. 11, p. 9606, 2021.
45. T. Ettaghzouti, N. Hassen, and K. Besbes, "A Novel Multi-Input Single-Output Mixed-Mode Universal Filter Employing Second Generation Current Conveyor Circuit," *Sensors, Circuits & Instrumentation Systems: Extended Papers 2017,* vol. 6, p. 53, 2018.
46. S. Maheshwari, "Realization of simple electronic functions using EXCCII," *Journal of Circuits, Systems and Computers,* vol. 26, p. 1750171, 2017.
47. S. V. Singh, R. S. Tomar, and M. Goswami, "A Current Tunable Mixed Mixed Mode ZC-CCTAs Based Resistor Less Universal Filter," Journal of Circuits, Systems and Computers, vol. 30, p. 2150225, 2021. https://doi.org/10.1142/S021812662150225X.

Arrived: 04. 07. 2022
Accepted: 16. 11. 2022

Original scientific paper
https://doi.org/10.33180/InfMIDEM2022.404

Informacije MIDEM
Journal of Microelectronics,
Electronic Components and Materials
Vol. 52, No. 4(2022), 239 – 262

Mixed-mode Universal Filter Using FD-CCCTA and its Extension as Shadow Filter

Divya Singh, Sajal K. Paul*

Department of Electronics Engineering, Indian Institute of Technology (Indian School of Mines), Dhanbad, Jharkhand, India

Abstract: This paper presents a fully differential current conveyor cascaded transconductance amplifier (FD-CCCTA), a modified FD-second generation current conveyor (FD-CCII) version. After that, a novel mixed-mode universal filter (UF) is developed employing only one FD-CCCTA. It results in all the four modes of UFs, namely current mode (CM), voltage mode (VM), transimpedance mode (TIM), and transadmittance mode (TAM). Moreover, this filter topology is extended to two mixed-mode universal shadow filters. The first shadow filter topology realizes the VM and CM universal filters. The second mixed-mode universal shadow filter realizes all four modes. The proposed shadow filters add flexibility in the orthogonal tuning of filter parameters, ω_0 and Q_0. Further, the gain of the shadow filter can be tuned electronically. Matching constraint is not required in any of the filters. The functional verifications have been performed using TSMC 180 nm technology in cadence virtuoso spectre.

Keywords: FD-CCCTA; FD-CCII; mixed-mode; shadow-filter

Univerzalni filter z mešanim načinom uporabe FD-CCCTA in njegova razširitev kot filter v senci

Izvleček: Članek predstavlja popolnoma diferencialni kaskadni transkondukcijski ojačevalnik (FD-CCCTA), modificirano različico tokovnega transporterja FD druge generacije (FD-CCII). Razvit nov univerzalni filter (UF) z mešanim načinom delovanja, ki uporablja samo en FD-CCCTA. Rezultat so vsi štirje načini UF, in sicer tokovni način (CM), napetostni način (VM), transimpedančni način (TIM) in transadmitančni način (TAM). Poleg tega je ta topologija filtra razširjena na dva univerzalna senčna filtra z mešanim načinom delovanja. Prva topologija senčnega filtra izvaja univerzalna filtra VM in CM. Drugi univerzalni filter v senci z mešanim načinom delovanja omogoča vse štiri načine delovanja. Predlagani filtri v senci povečujejo fleksibilnost pri ortogonalnem nastavljanju parametrov filtra, ω_0 in Q_0. Poleg tega je mogoče elektronsko nastaviti ojačenje filtra v senci. Pri nobenem od filtrov ni potrebna omejitev ujemanja. Funkcionalna preverjanja so bila izvedena s 180 nm tehnologijo TSMC v programu cadence virtuoso spectre.

Ključne besede: FD-CCCTA; FD-CCII; mešani način; filter senc

** Corresponding Author's e-mail: divs0508singh@gmail.com*

1 Introduction

Mixed-mode filters with all the responses of current-mode (CM) (both the input and output as a current), voltage- mode (VM) (both the input and output as a voltage), transimpedance-mode (TIM) (input as a current and output as a voltage), and transadmittance-mode (TAM) (input as a voltage and output as a current) are very much desirable in the analog signal processing, communication, and instrumentation [1]. At the same time, TAM and TIM filters play a vital role in the circuits which intends to connect the current mode circuits to the voltage mode circuits and vice-versa. TAM and TIM avoid the unnecessary circuitry requirement during V-I interfacing and the improvement in the effectiveness of the circuit. It concludes that the mixed-mode filters with all the four modes present in the same topology provide ample flexibility for analog circuit design. Few single-input-multiple-output (SIMO) mixed-mode universal filter topologies are available in the literature. SIMO [2] has got

How to cite:
D. Singh et al., "Mixed-mode Universal Filter Using FD-CCCTA and its Extension as Shadow Filter", Inf. Midem-J. Microelectron. Electron. Compon. Mater., Vol. 52, No. 4(2022), pp. 239–262

an advantage over single-input-single-output (SISO), multiple-input-multiple-output (MIMO), and multiple input single output (MISO) because of the availability of all the responses simultaneously. The topology [3] uses two fully differential second-generation current conveyors (FDCCIIs) with floating passive elements as four resistors and two capacitors to realize the UF in VM and TIM while multifunction filters in TAM and CM. It also requires matching components. Another three CC-CCTAs based mixed-mode topology [4] provide LP, BP, and HP responses in CM and TIM, whereas LP, BP, HP, and BR responses in VM, and UF in TAM. In [5], four OTAs are used to realize LP, BP, and HP responses in TAM, TIM, CM, and LP responses in VM. The topology [6] uses six OTAs, one resistor, and two capacitors to realize UF in VM and TIM, whereas realizing BP and HP responses in TAM and BP, HP, and BR responses in CM. It possesses floating passive components and lacks independent tuning of filter parameters. Three differential difference current conveyors (DDCCs), four resistors, and two capacitors with matching components and floating passive elements realize UF in VM and TIM while LP, BP, and HP in TAM and CM in [7]. In [8], three dual voltage current conveyors (DVCCs), six MOSs, and two capacitors are used to realize LP, BP, and HP in CM and TAM, whereas LP, BP in TIM while LP, BP, and BR in VM with matching components requirement and no electronic tunability. Mixed-mode universal filter reported in [9] uses six operational transconductance amplifiers (OTAs). The topology [10] requires three four-terminal floating nullors (FTFNs), three resistors, and two capacitors to realize the low pass (LP), band pass (BP), and high pass (HP) simultaneously in all the modes without independent and electronic tuning. In [11], one FDCCII, three resistors, and two capacitors realize UF in VM and TIM, whereas BP and HP responses in TAM, and BP, HP, and, band reject (BR) responses in CM. It possesses floating passive elements and does not have an electronic tunability feature. Simultaneously three responses (LP, BP, and HP) in all the modes are proposed in [12] with the use of five multiple-output current-controlled conveyors (MCCCIIs) and two capacitors.

Reports of several shadow filters using various building blocks are available in the literature. However, among them, the majority are either in VM [13-20] or CM [21-28] and only one topology [29] is of TAM and TIM. To the best of the authors' knowledge, there is no SIMO mixed-mode universal shadow filter report.

The paper aims to present a novel mixed-mode universal filter employing only one FD-CCCTA. Further, this filter topology is extended to a universal shadow filter for all four modes to enhance the tunability and independent variation of ω and Q and provide tunable gains. The proposed circuit exhibits the following advantages: least number of active building blocks, no floating components, the simultaneous realization of various responses, no need for component matching constraints, and electronic and independent tuning of filter parameters, including gains. Moreover, the proposed circuit is the first SIMO mixed-mode universal shadow filter to the best of the authors' knowledge.

This paper consists of six sections. The introduction is given in Section 1, followed by section 2, which details the active building block FD-CCCTA. Section 3 describes the proposed circuit configuration, and Section 4 describes the non-ideality analysis. Section 5 compares the available literature, followed by Section 6, which discusses the functional verification.

2 Fully differential current conveyor cascaded transconductance amplifier (FD-CCCTA)

FD-CCCTA is a modified version of a fully differential second-generation current conveyor (FD-CCII) [30]. The symbol of FD-CCCTA is shown in Fig. 1, and its CMOS-based internal structure is shown in Fig. 2. It consists of six input terminals in the form of X as a low impedance terminal and Y as a high impedance terminal, while four output terminals in the form of Z and O as high impedance terminals. FD-CCCTA is designed using FD-CCII and transconductance amplifier (TA), where TA is used in the cascaded form, and therefore O terminal can be increased as per the requirement.

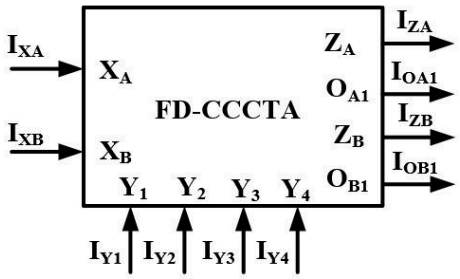

Figure 1: Symbol of FD-CCCTA.

The port relationships of FD-CCCTA can be expressed in matrix form as follows:

$$\begin{bmatrix} I_{Y1} \\ I_{Y2} \\ I_{Y3} \\ I_{Y4} \\ V_{XA} \\ V_{XB} \\ I_{ZA} \\ I_{ZB} \\ I_{OA1} \\ I_{OB1} \end{bmatrix} = \begin{bmatrix} 0 & 0 & 0 & 0 & 0 & 0 & 0 & 0 & 0 & 0 \\ 0 & 0 & 0 & 0 & 0 & 0 & 0 & 0 & 0 & 0 \\ 0 & 0 & 0 & 0 & 0 & 0 & 0 & 0 & 0 & 0 \\ 0 & 0 & 0 & 0 & 0 & 0 & 0 & 0 & 0 & 0 \\ 1 & -1 & 1 & 0 & 0 & 0 & 0 & 0 & 0 & 0 \\ -1 & 1 & 0 & 1 & 0 & 0 & 0 & 0 & 0 & 0 \\ 0 & 0 & 0 & 0 & 1 & 0 & 0 & 0 & 0 & 0 \\ 0 & 0 & 0 & 0 & 0 & 1 & 0 & 0 & 0 & 0 \\ 0 & 0 & 0 & 0 & 0 & 0 & g_{mA1} & 0 & 0 & 0 \\ 0 & 0 & 0 & 0 & 0 & 0 & 0 & g_{mB1} & 0 & 0 \end{bmatrix} \begin{bmatrix} V_{Y1} \\ V_{Y2} \\ V_{Y3} \\ V_{Y4} \\ I_{XA} \\ I_{XB} \\ V_{ZA} \\ V_{ZB} \\ V_{OA1} \\ V_{OB1} \end{bmatrix} \quad (1)$$

Where g_{mA1} and g_{mB1} are the transconductances of the transconductance amplifiers (TAs) connected at the Z_A and Z_B, respectively, can be expressed as:

$$g_{mA1} = \sqrt{\mu_n C_{ox} \left(\frac{W}{L}\right)_{M_{37},\ M_{38}} I_{A1}}, \quad and \ \ g_{mB1} = \sqrt{\mu_n C_{ox} \left(\frac{W}{L}\right)_{M_{41},\ M_{42}} I_{B1}} \quad (2)$$

The aspect ratios used for transistors of Fig. 2 are given in Table 1, and the performance parameters of FD-CCCTA are shown in Table 2.

Table 1: Aspect ratios of MOS Transistors of Fig. 2.

MOS Transistors	W(μm)/L(μm)
$M_{1\text{-}6}$	4.5/0.36
$M_{7,\ 8,\ 9,\ 13}$	36/0.36
$M_{10,\ 11,\ 12,\ 24}$	9/0.36
$M_{14,\ 15,\ 18,\ 19,\ 25,\ 29,\ 30,\ 33,\ 34}$	18/0.18
$M_{16,\ 17,\ 20,\ 21,\ 26,\ 31,\ 32,\ 35,\ 36}$	4.5/0.18
$M_{22,\ 23,\ 27,\ 28}$	0.36/0.36
$M_{37\text{-}44}$	10.8/0.36

Table 2: Performance parameters of FD-CCCTA.

Performance Parameters	Value
Supply Voltage	± 1.2 V
Power Consumption	1.9 mW
Parasitics at Y port (R_Y, C_Y)	2.131 MΩ
Parasitics at X port (R_X)	38.52 Ω
Parasitics at ZA port (R_{ZA}, C_{ZA})	1.22 MΩ, 28 fF
Parasitics at ZB port (R_{ZB}, C_{ZB})	4.4 MΩ, 12 fF
Parasitics at O_1 port (R_{O1}, C_{O1})	2.54 MΩ, 3.42 fF
Parasitics at O_2 port (R_{O2}, C_{O2})	2.3 MΩ, 3.24 fF
Linear variation of I_Z over IX	380 μA to 500 μA
Linear variation of V_X over V_Y	-1.04 V to 1.04 V
Bandwidth of I_Z/I_X	1.4 GHz
Bandwidth of I_{O1}/I_X	73.1 MHz
Bandwidth of I_{O2}/I_X	73.1 MHz

It may be noted in the following section that the mixed-mode filter uses one FD-CCCTA; however, its extended shadow filter uses two FD-CCCTAs. Hence to distinguish the similar mathematical and non-mathematical symbols concerning both the blocks in the shadow filter, superscripts (1) and (2) have been used throughout the paper, such as $g_{mA1}^{(1)}$ and $g_{mB1}^{(1)}$ for the first FD-CCCTA and $g_{mA1}^{(2)}$ and $g_{mB1}^{(2)}$ for second FD-CCCTA.

3 Proposed circuit configuration

The mixed-mode universal filter (also called non-shadow filter) is presented in section 3.1, followed by section 3.2, wherein two mixed-mode shadow filters are discussed.

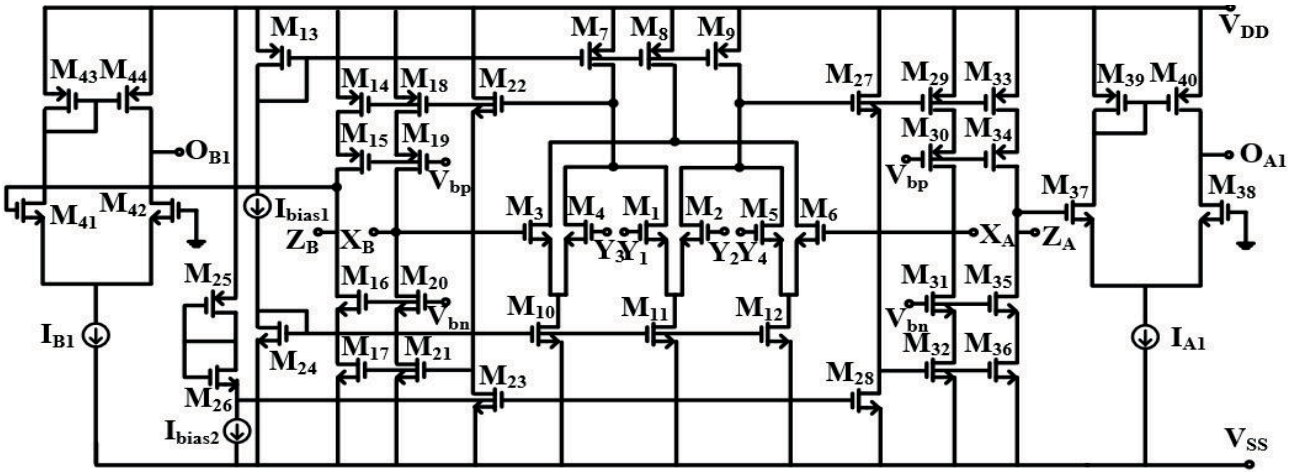

Figure 2: The CMOS-based internal structure of FD-CCCTA.

3.1 Mixed-mode universal filter

The proposed mixed-mode universal filter, depicted in Fig. 3, consists of one FD-CCCTA, three capacitors, and one resistor. The FD-CCCTA being used in the filter is shown in Fig. 2 with the introduction of additional terminals such as $O_{B1c}^{(1)}$, $O_{B1cc}^{(1)}$, and $O_{B1ccc}^{(1)}$, which are copy terminals of the $O_{B1}^{(1)}$. The $O_{B2}^{(1)}$ and $O_{B3}^{(1)}$ are the outputs of the other TAs. These TAs are connected in the cascaded, such as the input of the first TA is connected to the $Z_B^{(1)}$ terminal to get the $O_{B1}^{(1)}$, the input of the second TA is connected to the $O_{B1}^{(1)}$ terminal to get the $O_{B2}^{(1)}$, and similarly, the $O_{B3}^{(1)}$ terminal is obtained. The $-O_{B1}^{(1)}$ and $-O_{B2}^{(1)}$ are 180 degrees phase-shifted of $O_{B1}^{(1)}$ and $O_{B2}^{(1)}$, respectively. At the same time, $O_{B2c}^{(1)}$ and $-O_{B2c}^{(1)}$ are the copies of the $O_{B2}^{(1)}$ and $-O_{B2}^{(1)}$, respectively. Similarly, $O_{B3c}^{(1)}$ and $O_{B3cc}^{(1)}$ are the copies of the $O_{B3}^{(1)}$, while $-O_{B3}^{(1)}$ is 180-degree phase-shifted to $O_{B3}^{(1)}$. Thus, for obtaining the transfer functions in all four modes, such as VM, CM, TAM, and TIM, two input currents, $I_{in1} = I_{in2} = I_{in}$, are used, and a resistor (R_{in}) is used for TAM and TIM.

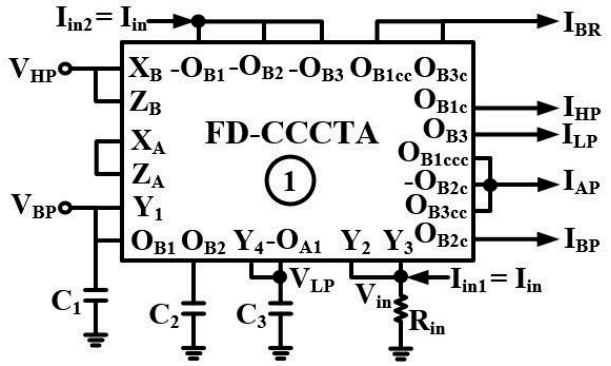

Figure 3: Proposed mixed-mode universal filter.

The routine analysis of the circuit in Fig. 3 results in the following transfers functions:

Voltage Mode (VM) [with $I_{in1} = I_{in2} = 0$, $R_{in} = \infty$ (i.e. Removed)]:

$$\frac{V_{LP}}{V_{in}} = -\frac{g_{mA1}^{(1)} g_{mB1}^{(1)}}{D(s)} \tag{3}$$

$$\frac{V_{BP}}{V_{in}} = \frac{sC_3 g_{mB1}^{(1)}}{D(s)} \tag{4}$$

$$\frac{V_{HP}}{V_{in}} = \frac{s^2 C_1 C_3}{D(s)} \tag{5}$$

The addition of $-V_{HP}$ and V_{LP} results in V_{BR}, while the addition of $-V_{HP}$, V_{BP}, and V_{LP} results in the V_{AP} using another voltage summer (not shown).

$$\frac{V_{BR}}{V_{in}} = -\frac{\left(s^2 C_1 C_3 + g_{mA1}^{(1)} g_{mB1}^{(1)}\right)}{D(s)} \tag{6}$$

$$\frac{V_{AP}}{V_{in}} = -\frac{\left(s^2 C_1 C_3 - sC_3 g_{mB1}^{(1)} + g_{mA1}^{(1)} g_{mB1}^{(1)}\right)}{D(s)} \tag{7}$$

Transimpedance Mode (TIM) [with $V_{in} = 0$, $I_{in2} = 0$]:

$$\frac{V_{LP}}{I_{in}} = -\frac{g_{mA1}^{(1)} g_{mB1}^{(1)} R_{in}}{D(s)} \tag{8}$$

$$\frac{V_{BP}}{I_{in}} = \frac{sC_3 g_{mB1}^{(1)} R_{in}}{D(s)} \tag{9}$$

$$\frac{V_{HP}}{I_{in}} = \frac{s^2 C_1 C_3 R_{in}}{D(s)} \tag{10}$$

The addition of $-V_{HP}$ and V_{LP} results in V_{BR}, while the addition of $-V_{HP}$, V_{BP}, and V_{LP} results in the V_{AP} using another voltage summer (not shown) as follows:

$$\frac{V_{BR}}{I_{in}} = -\frac{\left(s^2 C_1 C_3 + g_{mA1}^{(1)} g_{mB1}^{(1)}\right) R_{in}}{D(s)} \tag{11}$$

$$\frac{V_{AP}}{I_{in}} = -\frac{\left(s^2 C_1 C_3 - sC_3 g_{mB1}^{(1)} + g_{mA1}^{(1)} g_{mB1}^{(1)}\right) R_{in}}{D(s)} \tag{12}$$

Where,

$$D(s) = s^2 C_1 C_3 + sC_3 g_{mB1}^{(1)} + g_{mA1}^{(1)} g_{mB1}^{(1)} \tag{13}$$

The pole frequency (ω_o), quality factor (Q_o) and bandwidth (BW) are:

$$\omega_o = \sqrt{\frac{g_{mA1}^{(1)} g_{mB1}^{(1)}}{C_1 C_3}}, \quad Q_o = \sqrt{\frac{C_1 g_{mB3}^{(1)}}{C_3 g_{mB2}^{(1)}}} \quad and\ BW = \frac{g_{mB2}^{(1)}}{C_1} \tag{14}$$

The sensitivity analysis of ω_o, Q_o and BW using (14) results in:

$$S^{\omega_o}_{g^{(1)}_{mA1}} = S^{\omega_o}_{g^{(1)}_{mB1}} = \frac{1}{2}, S^{\omega_o}_{C_1} = S^{\omega_o}_{C_3} = -\frac{1}{2}$$

$$S^{Q_o}_{g^{(1)}_{mB3}} = S^{Q_o}_{C_1} = \frac{1}{2}, S^{Q_o}_{g^{(1)}_{mB2}} = S^{Q_o}_{C_3} = -\frac{1}{2}$$

$$S^{BW}_{g^{(1)}_{mB2}} = 1, S^{BW}_{C_1} = -1$$

Current Mode (CM) [with $V_{in} = 0$, $I_{in1} = 0$, $R_{in} = 0$]:

$$\frac{I_{LP}}{I_{in}} = \frac{g^{(1)}_{mB2} g^{(1)}_{mB3}}{D(s)} \quad (15)$$

$$\frac{I_{BP}}{I_{in}} = \frac{sC_2 g^{(1)}_{mB2}}{D(s)} \quad (16)$$

$$\frac{I_{HP}}{I_{in}} = \frac{s^2 C_1 C_2}{D(s)} \quad (17)$$

$$\frac{I_{BR}}{I_{in}} = \frac{s^2 C_1 C_2 + g^{(1)}_{mB2} g^{(1)}_{mB3}}{D(s)} \quad (18)$$

$$\frac{I_{AP}}{I_{in}} = \frac{s^2 C_1 C_2 - sC_2 g^{(1)}_{mB2} + g^{(1)}_{mB2} g^{(1)}_{mB3}}{D(s)} \quad (19)$$

Transadmittance Mode (TAM) [with $I_{in1} = 0$]:

$$\frac{I_{LP}}{V_{in}} = \frac{g^{(1)}_{mB2} g^{(1)}_{mB3}}{D(s) * R_{in}} \quad (20)$$

$$\frac{I_{BP}}{V_{in}} = \frac{sC_2 g^{(1)}_{mB2}}{D(s) * R_{in}} \quad (21)$$

$$\frac{I_{HP}}{V_{in}} = \frac{s^2 C_1 C_2}{D(s) * R_{in}} \quad (22)$$

$$\frac{I_{BR}}{V_{in}} = \frac{s^2 C_1 C_2 + g^{(1)}_{mB2} g^{(1)}_{mB3}}{D(s) * R_{in}} \quad (23)$$

$$\frac{I_{AP}}{V_{in}} = \frac{s^2 C_1 C_2 - sC_2 g^{(1)}_{mB2} + g^{(1)}_{mB2} g^{(1)}_{mB3}}{D(s) * R_{in}} \quad (24)$$

Where,

$$D(s) = s^2 C_1 C_2 + sC_2 g^{(1)}_{mB2} + g^{(1)}_{mB2} g^{(1)}_{mB3} \quad (25)$$

The pole frequency (ω_o), quality factor (Q_o) and bandwidth (BW) are:

$$\omega_o = \sqrt{\frac{g^{(1)}_{mB2} g^{(1)}_{mB3}}{C_1 C_2}}, \quad Q_o = \sqrt{\frac{C_1 g^{(1)}_{mB3}}{C_2 g^{(1)}_{mB2}}} \quad (26)$$

$$and\ BW = \frac{g^{(1)}_{mB2}}{C_1}$$

The sensitivity analysis of ω_o, Q_o and BW using (26) results in:

$$S^{\omega_o}_{g^{(1)}_{mB2}} = S^{\omega_o}_{g^{(1)}_{mB3}} = \frac{1}{2}, S^{\omega_o}_{C_1} = S^{\omega_o}_{C_2} = -\frac{1}{2},$$

$$S^{Q_o}_{g^{(1)}_{mB3}} = S^{Q_o}_{C_1} = \frac{1}{2}, S^{Q_o}_{g^{(1)}_{mB2}} = S^{Q_o}_{C_2} = -\frac{1}{2}$$

$$S^{BW}_{g^{(1)}_{mB2}} = 1, S^{BW}_{C_1} = -1$$

The above equation indicates that the ω_o, Q_o, and BW are electronically tunable by bias currents because of $g^{(1)}_{mB2}$ and $g^{(1)}_{mB3}$. Sensitivity of the parameters of eqn. (26) are found within the unity.

3.2 Mixed-mode shadow Filter

Shadow filter also known as frequency agile filter, a recently introduced filters is shown in Fig. 4 [31]. The inclusion of an additional external amplifier in the feedback of the basic filter gives the structure of shadow filter. The introduction of gain (A) of this external amplifier in the filter parameters improves the tunability and eases in frequency agility in comparison of the conventional tuning technique.

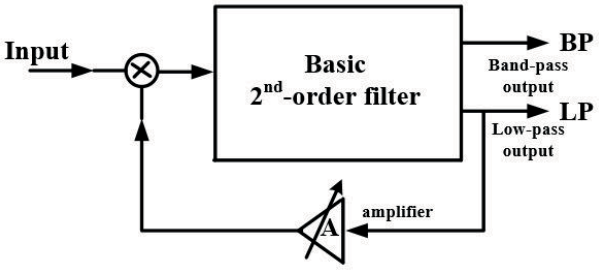

Figure 4: Scheme of the shadow filter [31].

In line with Fig. 4, block diagram for the implementation of mixed-mode shadow filter is shown in Fig. 5. Combination of voltage and current signals at the input as well as at the output form all the modes such as VM, CM, TIM, and TAM. Two amplifiers with gains A_1 and A_2 multiplied with the V_{AP} and I_{BP} are fed-back to the voltage and current input signals, respectively.

In this section, two topologies are proposed for mixed-mode shadow filters using basic mixed mode UF of Fig. 3. The first topology realizes VM and CM universal filters, and the second topology realizes all four modes of

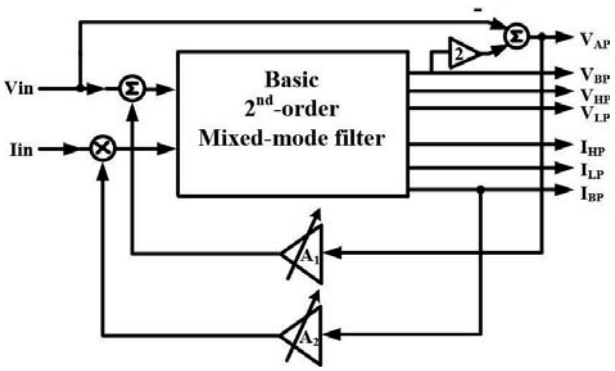

Figure 5: Block diagram for the implementation of mixed-mode shadow filter.

mixed-mode filters. Both the topologies have been implemented on the basis of the structure shown in Fig. 5.

3.2.1 First shadow filter (VM and CM)

The proposed shadow filter in the VM and CM, as shown in Fig. 6, consists of the above mixed-mode universal filter of Fig. 3 along with a second FD-CCCTA block and two variable resistors (R_1 & R_2) consisting of MOSs. V_{BP} is given to $Y_2^{(2)}$ and $Y_4^{(2)}$ terminals for the sake of the VM shadow filter, and I_{BP} is given to the $X_A^{(2)}$ terminal for the CM shadow filter. The second FD-CCCTA in Fig. 6 aims to create two amplifiers, A_1 and A_2, in the feedback loop [32] of the previous mixed-mode filter (Fig. 3) to obtain the VM and CM shadow filters. By routine analysis of Fig. 6, it is shown in eqn. (38) that

$$A_1 = g_{mB}^{(2)} R_1 \text{ and } A_2 = g_{mA}^{(2)} R_2$$

The value of MOS resistors can be adjusted with their respective bias voltages, V_{C1} and V_{C2} [33]. The equation for the resistance is:

$$R = \frac{L}{2\mu C_{ox} W\left(V_{Ci} - V_T\right)} \tag{27}$$

Where L and W are the channel length and channel width, μ is the effective mobility, C_{ox} is the gate oxide capacitance, and V_T is the threshold voltage of the MOS transistor.

The routine analysis of the circuit Fig. 6 results in the following transfer function:

The port relationships of FD-CCCTA suggests:

$$\begin{aligned} &V_{XA} = V_{Y1} - V_{Y2} + V_{Y3} \\ &and\, V_{XB} = -V_{Y1} + V_{Y2} + V_{Y4} \end{aligned} \tag{28}$$

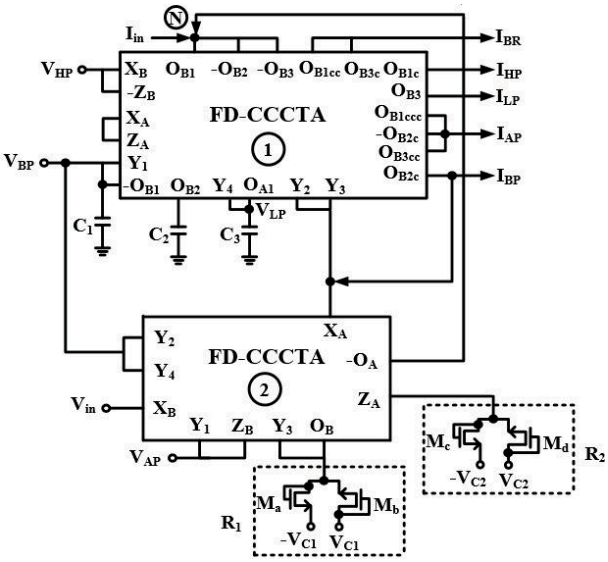

Figure 6: Proposed first shadow filter.

Therefore for FD-CCCTA-1, we get:

$$V_{XA}^{(1)} = V_{BP} \tag{29}$$

$$V_{HP} = -V_{BP} + V_{Y2}^{(1)} + V_{LP} \tag{30}$$

While for FD-CCCTA-2 we get:

$$V_{XA}^{(2)} = V_{AP} - V_{BP} + V_{Y3}^{(2)} \tag{31}$$

$$V_{in} = -V_{AP} + 2V_{BP} \tag{32}$$

Again, the port relationships of FD-CCCTA-1 results:

$$I_{OA1}^{(1)} = g_{mA1}^{(1)} V_{ZA} \; and \; I_{OB1}^{(1)} = g_{mB1}^{(1)} V_{ZB} \tag{33}$$

Which corresponds to:

$$V_{LP} sC_3 = g_{mA1}^{(1)} V_{BP} \; and - V_{BP} sC_1 = g_{mB1}^{(1)} V_{HP} \tag{34}$$

Another port relationships of FD-CCCTA-1 results:

$$I_{OB2}^{(1)} = g_{mB2}^{(1)} V_{OB1} \; and \; I_{OB3}^{(1)} = g_{mB3}^{(1)} V_{OB2} \tag{35}$$

Which corresponds:

$$I_{BP} = -g_{mB2}^{(1)} \frac{I_{HP}}{sC_1} and \; I_{LP} = g_{mB3}^{(1)} \frac{I_{BP}}{sC_2} \tag{36}$$

Whereas, port relationships of FD-CCCTA-2 results:

$$I_{-OA}^{(2)} = -g_{mA}^{(2)} V_{ZA} \; and \; I_{OB}^{(2)} = g_{mB}^{(2)} V_{ZB} \tag{37}$$

Hence, (35) results:

$$I_{-OA}^{(2)} = -g_{mA}^{(2)} R_2 I_{BP} \; and \; \frac{V_{Y3}^{(2)}}{R_1} = g_{mB}^{(2)} V_{AP} \tag{38}$$

It can be written as:

$$I_{-OA}^{(2)} = -A_2 I_{BP} \; and \; V_{Y3}^{(2)} = A_1 V_{AP} \tag{39}$$

Where $A_1 = g_{mB}^{(2)} R_1$ and $A_2 = g_{mA}^{(2)} R_2$ (40)

Eqn. (31) can be rewritten after substituting the value of

$V_{Y3}^{(2)}$ from (39) as

$$V_{XA}^{(2)} = V_{AP}\left(1 + A_1\right) - V_{BP} \tag{41}$$

Now, (28) can be rewritten as:

$$V_{HP} = -V_{BP} + V_{XA}^{(2)} + V_{LP} \tag{42}$$

Therefore,

$$V_{HP} = -V_{BP} + V_{AP}\left(1 + A_1\right) - V_{BP} + V_{LP} \tag{43}$$

Substituting the value of V_{AP} from eqn. (32) into eqn. (43) gives:

$$V_{in}\left(1 + A_1\right) = -V_{HP} + 2V_{BP} A_1 + V_{LP} \tag{44}$$

Whereas for the current mode (CM), the expression of currents at node N is given as:

$$I_{in} = -I_{HP} + I_{BP}\left(1 + A_2\right) + I_{LP} \tag{45}$$

Now the voltage mode transfer functions are obtained by using eqn. (34) and eqn. (44) while, current mode transfer functions are obtained by using eqn. (36) and eqn. (45) as follows:

Voltage mode [with Iin = 0]:

$$\frac{V_{LP}}{V_{in}} = \frac{g_{mA1}^{(1)} g_{mB1}^{(1)}\left(1 + A_1\right)}{D(s)} \tag{46}$$

$$\frac{V_{BP}}{V_{in}} = \frac{sC_3 g_{mB1}^{(1)}\left(1 + A_1\right)}{D(s)} \tag{47}$$

$$\frac{V_{HP}}{V_{in}} = -\frac{s^2 C_1 C_3\left(1 + A_1\right)}{D(s)} \tag{48}$$

$$\frac{V_{AP}}{V_{in}} = -\frac{\left(s^2 C_1 C_3 - 2sC_3 g_{mB1}^{(1)} + g_{mA1}^{(1)} g_{mB1}^{(1)}\right)}{D(s)} \tag{49}$$

By the addition of -V_{HP} and V_{LP} results into V_{BR} using voltage summer.

$$\frac{V_{BR}}{V_{in}} = \frac{\left(s^2 C_1 C_3 + g_{mA1}^{(1)} g_{mB1}^{(1)}\right)\left(1 + A_1\right)}{D(s)} \tag{50}$$

Where,

$$\begin{aligned} A_1 &= g_{mB}^{(2)} R_1 \\ D(s) &= s^2 C_1 C_3 + 2A_1 sC_3 g_{mB1}^{(1)} + g_{mA1}^{(1)} g_{mB1}^{(1)} \end{aligned} \tag{51}$$

The pole frequency (ω_o), quality factor (Q_o) and bandwidth (BW) are:

$$\begin{aligned} &\omega_o = \sqrt{\frac{g_{mA1}^{(1)} g_{mB1}^{(1)}}{C_1 C_3}}, \quad Q_o = \frac{1}{2A_1}\sqrt{\frac{C_1 g_{mA1}^{(1)}}{C_3 g_{mB1}^{(1)}}} \\ &and \; BW = 2A_1 \frac{g_{mB1}^{(1)}}{C_1} \end{aligned} \tag{52}$$

Considering $C_1 = C_3$, eqn. (52) gives:

$$\begin{aligned} &\omega_o = \frac{\sqrt{g_{mA1}^{(1)} g_{mB1}^{(1)}}}{C}, \quad Q_o = \frac{1}{2A_1}\sqrt{\frac{g_{mA1}^{(1)}}{g_{mB1}^{(1)}}} \\ &and \; BW = 2A_1 \frac{g_{mB1}^{(1)}}{C} \end{aligned} \tag{53}$$

The gain of the filter can be expressed as:

$$\begin{aligned} &A_{LP} = A_{HP} = A_{BR} = \left(1 + A_1\right), A_{BP} = \frac{\left(1 + A_1\right)}{2A_1}, \\ &A_{AP} = \frac{1}{A_1} \end{aligned} \tag{54}$$

The sensitivity analysis of ω_o, Q_o and BW using (52) results in:

$$S_{g_{mA1}^{(1)}}^{\omega_o} = S_{g_{mB1}^{(1)}}^{\omega_o} = \frac{1}{2}, S_{C_1}^{\omega_o} = S_{C_3}^{\omega_o} = -\frac{1}{2},$$

$$S_{g_{mA1}^{(1)}}^{Q_o} = S_{C_1}^{Q_o} = \frac{1}{2}, S_{g_{mB1}^{(1)}}^{Q_o} = S_{C_3}^{Q_o} = -\frac{1}{2},$$

$$S_{g_{mB}^{(2)}}^{Q_o} = S_{R_1}^{Q_o} = -$$

$$S_{g_{mB1}^{(1)}}^{BW} = 1, S_{C_1}^{BW} = -1, S_{g_{mB}^{(2)}}^{BW} = S_{R_1}^{BW} = 1$$

The above eqn. (53) indicates that the ω_o, Q_o, and BW are electronically tunable by bias currents because of

$g_{mA1}^{(1)}$, and $g_{mB1}^{(1)}$, and ω_o is independently tunable by C, while Q_o is independently tunable by gain A_1, i.e., $g_{mB}^{(2)}$ as well as R_1. Also, the tuning of gain is obtained by A_1.

Current mode [with Vin = 0]:

$$\frac{I_{LP}}{I_{in}} = \frac{g_{mB2}^{(1)} g_{mB3}^{(1)}}{D(s)} \tag{55}$$

$$\frac{I_{BP}}{I_{in}} = \frac{sC_2 g_{mB2}^{(1)}}{D(s)} \tag{56}$$

$$\frac{I_{HP}}{I_{in}} = -\frac{s^2 C_1 C_2}{D(s)} \tag{57}$$

$$\frac{I_{BR}}{I_{in}} = \frac{s^2 C_1 C_2 + g_{mB2}^{(1)} g_{mB3}^{(1)}}{D(s)} \tag{58}$$

$$\frac{I_{AP}}{I_{in}} = \frac{\left(s^2 C_1 C_2 - sC_2 g_{mB2}^{(1)} + g_{mB2}^{(1)} g_{mB3}^{(1)}\right)}{D(s)} \tag{59}$$

Where,

$$D(s) = s^2 C_1 C_2 + (1 + A_2) sC_2 g_{mB2}^{(1)} + g_{mB2}^{(1)} g_{mB3}^{(1)}$$
$$and\ A_2 = g_{mA}^{(2)} R_2 \tag{60}$$

The pole frequency (ω_o), quality factor (Q_o) and bandwidth (BW) are:

$$\omega_o = \sqrt{\frac{g_{mB2}^{(1)} g_{mB3}^{(1)}}{C_1 C_2}}, \quad Q_o = \frac{1}{(1 + A_2)} \sqrt{\frac{C_1 g_{mB3}^{(1)}}{C_2 g_{mB2}^{(1)}}}$$
$$and\ BW = (1 + A_2) \frac{g_{mB2}^{(1)}}{C_1} \tag{61}$$

Considering, $C_1 = C_2$, eqn. (61) gives:

$$\omega_o = \frac{\sqrt{g_{mB2}^{(1)} g_{mB3}^{(1)}}}{C}, \quad Q_o = \frac{1}{(1 + A_2)} \sqrt{\frac{g_{mB3}^{(1)}}{g_{mB2}^{(1)}}}$$
$$and\ BW = (1 + A_2) \frac{g_{mB2}^{(1)}}{C} \tag{62}$$

The sensitivity analysis of ω_o, Q_o and BW using (61) results in:

$$S_{g_{mB2}^{(1)}}^{\omega_o} = S_{g_{mB3}^{(1)}}^{\omega_o} = \frac{1}{2}, S_{C_1}^{\omega_o} = S_{C_2}^{\omega_o} = -\frac{1}{2},$$

$$S_{g_{mB3}^{(1)}}^{Q_o} = S_{C_1}^{Q_o} = \frac{1}{2}, S_{g_{mB2}^{(1)}}^{Q_o} = S_{C_2}^{Q_o} = -\frac{1}{2},$$

$$S_{g_{mA}^{(2)}}^{Q_o} = S_{R_2}^{Q_o} = -\frac{A_2}{1 + A_2}$$

$$S_{g_{mB2}^{(1)}}^{BW} = 1, S_{C_1}^{BW} = -1, S_{g_{mA}^{(2)}}^{BW} = S_{R_2}^{BW} = \frac{A_2}{1 + A_2}$$

The above equation indicates that the ω_o, Q_o, and BW are electronically tunable by bias currents because of $g_{mB2}^{(1)}$, and $g_{mB3}^{(1)}$, and ω_o is independently tunable by C, while Q_o is independently tunable by gain A_2, i.e., $g_{mA}^{(2)}$ as well as R_2. Sensitivity analysis of all the parameters resulted within the unity.

3.2.2 Second shadow filter (all four modes)

The second shadow filter shown in Fig. 7 realizes all the modes, such as VM, CM, TAM, and TIM. This circuit is a slight alteration of Fig. 6 with the addition of one input resistor (R_{in}) and one more input current such that $I_{in1} = I_{in2} = I_{in}$.

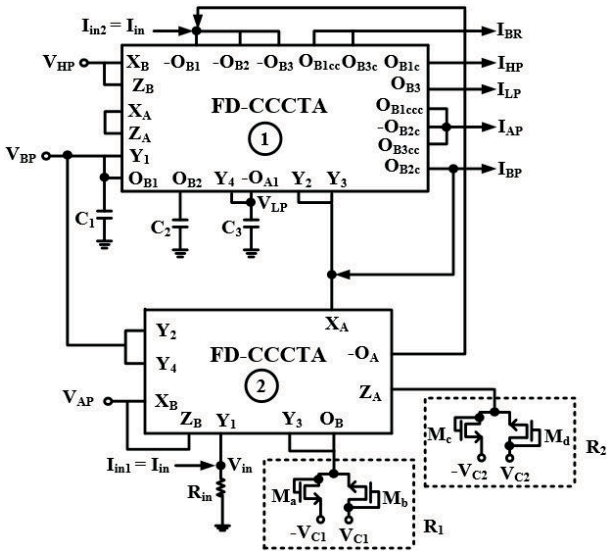

Figure 7: Proposed second mixed mode shadow filter.

The routine analysis of the circuit Fig. 7 in line with Fig. 6 results in the following transfer functions for VM, CM, TIM, and TAM:

Voltage mode (VM) [with $I_{in1} = I_{in2} = 0$, $R_{in} = \infty$ (Removed)]:

$$\frac{V_{LP}}{V_{in}} = -\frac{g_{mA1}^{(1)} g_{mB1}^{(1)} (1 - A_1)}{D(s)} \tag{63}$$

$$\frac{V_{BP}}{V_{in}} = \frac{sC_3 g_{mB1}^{(1)}\left(1-A_1\right)}{D(s)} \tag{64}$$

$$\frac{V_{HP}}{V_{in}} = \frac{s^2 C_1 C_3 \left(1-A_1\right)}{D(s)} \tag{65}$$

$$\frac{V_{AP}}{V_{in}} = -\frac{\left(s^2 C_1 C_3 - sC_3 g_{mB1}^{(1)} + g_{mA1}^{(1)} g_{mB1}^{(1)}\right)}{D(s)} \tag{66}$$

By the addition of V_{HP} and $-V_{LP}$ results into V_{BR} using voltage summer.

$$\frac{V_{BR}}{V_{in}} = \frac{\left(s^2 C_1 C_3 + g_{mA1}^{(1)} g_{mB1}^{(1)}\right)\left(1-A_1\right)}{D(s)} \tag{67}$$

Transimpedance mode (TIM) [with $V_{in} = 0$, $I_{in2} = 0$]:

$$\frac{V_{LP}}{I_{in}} = -\frac{g_{mA1}^{(1)} g_{mB1}^{(1)} R_{in}\left(1-A_1\right)}{D(s)} \tag{68}$$

$$\frac{V_{BP}}{I_{in}} = \frac{sC_3 g_{mB1}^{(1)} R_{in}\left(1-A_1\right)}{D(s)} \tag{69}$$

$$\frac{V_{HP}}{I_{in}} = \frac{s^2 C_1 C_3 R_{in}\left(1-A_1\right)}{D(s)} \tag{70}$$

$$\frac{V_{AP}}{I_{in}} = -\frac{\left(s^2 C_1 C_3 - sC_3 g_{mB1}^{(1)} + g_{mA1}^{(1)} g_{mB1}^{(1)}\right) R_{in}}{D(s)} \tag{71}$$

By the addition of V_{HP} and $-V_{LP}$ results into V_{BR} using voltage summer.

$$\frac{V_{BR}}{I_{in}} = \frac{\left(s^2 C_1 C_3 + g_{mA1}^{(1)} g_{mB1}^{(1)}\right) R_{in}\left(1-A_1\right)}{D(s)} \tag{72}$$

Where,

$$D(s) = s^2 C_1 C_3 + 2\left(1-A_1\right) sC_3 g_{mB1}^{(1)} + g_{mA1}^{(1)} g_{mB1}^{(1)}$$
$$and\ A_1 = g_{mB}^{(2)} R_1 \tag{73}$$

The pole frequency (ω_o), quality factor (Q_o) and bandwidth (BW) are:

$$\omega_o = \sqrt{\frac{g_{mA1}^{(1)} g_{mB1}^{(1)}}{C_1 C_3}}, \quad Q_o = \frac{1}{2\left(1-A_1\right)}\sqrt{\frac{C_1 g_{mA1}^{(1)}}{C_3 g_{mB1}^{(1)}}}$$
$$and\ BW = 2\left(1-A_1\right)\frac{g_{mB1}^{(1)}}{C_1} \tag{74}$$

Considering, $C_1 = C_3$, eqn. (74) gives:

$$\omega_o = \frac{\sqrt{g_{mA1}^{(1)} g_{mB1}^{(1)}}}{C}, \quad Q_o = \frac{1}{2\left(1-A_1\right)}\sqrt{\frac{g_{mA1}^{(1)}}{g_{mB1}^{(1)}}}$$
$$and\ BW = 2\left(1-A_1\right)\frac{g_{mB1}^{(1)}}{C} \tag{75}$$

The gain of the filter can be expressed as:

$$A_{LP} = A_{HP} = A_{BR} = \left(1-A_1\right), A_{BP} = \frac{\left(1-A_1\right)}{2\left(1-A_1\right)},$$
$$and \quad A_{AP} = \frac{1}{2\left(1-A_1\right)} \tag{76}$$

The sensitivity analysis of ω_o, Q_o and BW using (74) results in:

$$S_{g_{mA1}^{(1)}}^{\omega_o} = S_{g_{mB1}^{(1)}}^{\omega_o} = \frac{1}{2}, S_{C_1}^{\omega_o} = S_{C_3}^{\omega_o} = -\frac{1}{2},$$

$$S_{g_{mA1}^{(1)}}^{Q_o} = S_{C_1}^{Q_o} = \frac{1}{2}, S_{g_{mB1}^{(1)}}^{Q_o} = S_{C_3}^{Q_o} = -\frac{1}{2},$$

$$S_{g_{mB}^{(2)}}^{Q_o} = S_{R_1}^{Q_o} = -\frac{\mathrm{A}_1}{1-\mathrm{A}_1}$$

$$S_{g_{mB1}^{(1)}}^{BW} = 1, S_{C_1}^{BW} = -1, S_{g_{mB}^{(2)}}^{BW} = S_{R_1}^{BW} = \frac{\mathrm{A}_1}{1-\mathrm{A}_1}$$

The (73) indicates that the ω_o, Q_o, and BW are electronically tunable by bias currents because of $g_{mA1}^{(1)}$ and $g_{mB1}^{(1)}$. Moreover, ω_o is independently tunable by C, while Q_o is independently tunable by gain A_1, i.e., $g_{mB}^{(2)}$ and R_1. Also, the VM and TIM shadow filter's gain is tunable by A_1 as indicated in (74).

Current mode (CM) [with $V_{in} = 0$, $I_{in1} = 0$, $R_{in} = 0$]:

$$\frac{I_{LP}}{I_{in}} = \frac{g_{mB2}^{(1)} g_{mB3}^{(1)}}{D(s)} \tag{77}$$

$$\frac{I_{BP}}{I_{in}} = \frac{sC_2 g_{mB2}^{(1)}}{D(s)} \tag{78}$$

$$\frac{I_{HP}}{I_{in}} = \frac{s^2 C_1 C_2}{D(s)} \tag{79}$$

$$\frac{I_{BR}}{I_{in}} = \frac{s^2 C_1 C_2 + g_{mB2}^{(1)} g_{mB3}^{(1)}}{D(s)} \tag{80}$$

$$\frac{I_{AP}}{I_{in}} = \frac{\left(s^2 C_1 C_2 - sC_2 g_{mB2}^{(1)} + g_{mB2}^{(1)} g_{mB3}^{(1)}\right)}{D(s)} \quad (81)$$

Transadmittance mode (TAM) [with $I_{in1} = 0$]:

$$\frac{I_{LP}}{V_{in}} = \frac{g_{mB2}^{(1)} g_{mB3}^{(1)}}{D(s) * R_{in}} \quad (82)$$

$$\frac{I_{BP}}{V_{in}} = \frac{sC_2 g_{mB2}^{(1)}}{D(s) * R_{in}} \quad (83)$$

$$\frac{I_{HP}}{V_{in}} = \frac{s^2 C_1 C_2}{D(s) * R_{in}} \quad (84)$$

$$\frac{I_{BR}}{V_{in}} = \frac{s^2 C_1 C_2 + g_{mB2}^{(1)} g_{mB3}^{(1)}}{D(s) * R_{in}} \quad (85)$$

$$\frac{I_{AP}}{V_{in}} = \frac{\left(s^2 C_1 C_2 - sC_2 g_{mB2}^{(1)} + g_{mB2}^{(1)} g_{mB3}^{(1)}\right)}{D(s) * R_{in}} \quad (86)$$

Where,

$$D(s) = s^2 C_1 C_2 + (1 + A_2) sC_2 g_{mB2}^{(1)} + g_{mB2}^{(1)} g_{mB3}^{(1)} \quad and \; A_2 = g_{mA}^{(2)} R_2 \quad (87)$$

The pole frequency (ω_o), quality factor (Q_o) and bandwidth (BW) are:

$$\omega_o = \sqrt{\frac{g_{mB2}^{(1)} g_{mB3}^{(1)}}{C_1 C_2}}, \quad Q_o = \frac{1}{(1 + A_2)} \sqrt{\frac{C_1 g_{mB3}^{(1)}}{C_2 g_{mB2}^{(1)}}} \quad and \; BW = (1 + A_2) \frac{g_{mB2}^{(1)}}{C_1} \quad (88)$$

Considering, $C_1 = C_2$, eqn. (88) gives:

$$\omega_o = \frac{\sqrt{g_{mB2}^{(1)} g_{mB3}^{(1)}}}{C}, \; Q_o = \frac{1}{(1 + A_2)} \sqrt{\frac{g_{mB3}^{(1)}}{g_{mB2}^{(1)}}} \quad and \; BW = (1 + A_2) \frac{g_{mB2}^{(1)}}{C} \quad (89)$$

The sensitivity analysis of ω_o, Q_o and BW using (88) results in:

$$S_{g_{mB2}^{(1)}}^{\omega_o} = S_{g_{mB3}^{(1)}}^{\omega_o} = \frac{1}{2}, S_{C_1}^{\omega_o} = S_{C_2}^{\omega_o} = -\frac{1}{2},$$

$$S_{g_{mB3}^{(1)}}^{Q_o} = S_{C_1}^{Q_o} = \frac{1}{2}, S_{g_{mB2}^{(1)}}^{Q_o} = S_{C_2}^{Q_o} = -\frac{1}{2},$$

$$S_{g_{mA}^{(2)}}^{Q_o} = S_{R_2}^{Q_o} = -\frac{A_2}{1 + A_2}$$

$$S_{g_{mB2}^{(1)}}^{BW} = 1, S_{C_1}^{BW} = -1, S_{g_{mA}^{(2)}}^{BW} = S_{R_2}^{BW} = \frac{A_2}{1 + A_2}$$

The equation (89) indicates that the ω_o, Q_o, and BW are electronically tunable by bias currents because of $g_{mB2}^{(1)}$ and $g_{mB3}^{(1)}$. Moreover, ω_o is independently tunable by C, while Q_o is independently tunable by gain A_2, i.e., $g_{mA}^{(2)}$ and R_2. Sensitivity analysis of all the parameters results within the unity magnitude.

4 Non-ideality analysis

Non-ideal transfer gains and active building block parasitics will have an impact practically. Sections 4.1 discusses the effect due to non-ideal transfer gains. and section 4.2 discusses the effect due to parasitics of FD-CCCTA.

4.1 Non-ideal transfer gain of FD-CCCTA

The port relationship is modified as follows when taking into account the non-idealities of the voltage, current, and transconductance gains of FD-CCCTA:

$$\begin{bmatrix} I_{Y1} \\ I_{Y2} \\ I_{Y3} \\ I_{Y4} \\ V_{XA} \\ V_{XB} \\ I_{ZA} \\ I_{ZB} \\ I_{OA1} \\ I_{OB1} \end{bmatrix} = \begin{bmatrix} 0 & 0 & 0 & 0 & 0 & 0 & 0 & 0 & 0 & 0 \\ 0 & 0 & 0 & 0 & 0 & 0 & 0 & 0 & 0 & 0 \\ 0 & 0 & 0 & 0 & 0 & 0 & 0 & 0 & 0 & 0 \\ 0 & 0 & 0 & 0 & 0 & 0 & 0 & 0 & 0 & 0 \\ \beta_{a1} & -\beta_{a2} & \beta_{a3} & 0 & 0 & 0 & 0 & 0 & 0 & 0 \\ -\beta_{b1} & \beta_{b2} & 0 & \beta_{b3} & 0 & 0 & 0 & 0 & 0 & 0 \\ 0 & 0 & 0 & 0 & \alpha_a & 0 & 0 & 0 & 0 & 0 \\ 0 & 0 & 0 & 0 & 0 & \alpha_b & 0 & 0 & 0 & 0 \\ 0 & 0 & 0 & 0 & 0 & 0 & \gamma_{a1} g_{mA1} & 0 & 0 & 0 \\ 0 & 0 & 0 & 0 & 0 & 0 & 0 & \gamma_{b1} g_{mB1} & 0 & 0 \end{bmatrix} \begin{bmatrix} V_{Y1} \\ V_{Y2} \\ V_{Y3} \\ V_{Y4} \\ I_{XA} \\ I_{XB} \\ V_{ZA} \\ V_{ZB} \\ V_{OA1} \\ V_{OB1} \end{bmatrix} \quad (90)$$

Where β_{ai} (i=1,2,3) is the voltage transfer gain between $Y_{(i)}$ and X_A terminals, β_{bi} (i=1,2,3) is the voltage transfer gain between $Y_{(i)}$ and X_B terminals, is the current transfer gain between I_{ZA} and I_{XA} terminals, α_b is the current transfer gain between I_{ZB} and I_{XB} terminals, γ_{a1} is the transconductance gain between I_{OA1} and V_{OA1}, and γ_{b1} is the transconductance gain between I_{OB1} and V_{OB1}. These gain factors are found unity ideally but they deviate slightly from unity practically. The transfer functions of Fig. 3 after considering the non-idealities are obtained as follows:

Voltage Mode (VM):

$$\frac{V_{LP}}{V_{in}} = -\frac{g_{mA1}^{(1)} g_{mB1}^{(1)} \beta_{a1} \beta_{b2} \gamma_{a1} \gamma_{b1}}{D(s)} \quad (91)$$

$$\frac{V_{BP}}{V_{in}} = \frac{sC_3 g_{mB1}^{(1)} \beta_{b2} \gamma_{B1}}{D(s)} \quad (92)$$

$$\frac{V_{HP}}{V_{in}} = \frac{s^2 C_1 C_3 \beta_{b2}}{D(s)} \quad (93)$$

$$\frac{V_{BR}}{V_{in}} = -\frac{\left(s^2 C_1 C_3 \beta_{b2} + g_{mA1}^{(1)} g_{mB1}^{(1)} \beta_{a1} \beta_{b2} \gamma_{a1} \gamma_{b1}\right)}{D(s)} \quad (94)$$

$$\frac{V_{AP}}{V_{in}} = -\frac{\begin{pmatrix} s^2 C_1 C_3 \beta_{b2} - sC_3 g_{mB1}^{(1)} \beta_{b2} \gamma_{B1} \\ + g_{mA1}^{(1)} g_{mB1}^{(1)} \beta_{a1} \beta_{b2} \gamma_{a1} \gamma_{b1} \end{pmatrix}}{D(s)} \quad (95)$$

Transimpedance Mode (TIM):

$$\frac{V_{LP}}{I_{in}} = -\frac{g_{mA1}^{(1)} g_{mB1}^{(1)} \beta_{a1} \beta_{b2} \gamma_{a1} \gamma_{b1} R_{in}}{D(s)} \quad (96)$$

$$\frac{V_{BP}}{I_{in}} = \frac{sC_3 g_{mB1}^{(1)} \beta_{b2} \gamma_{b1} R_{in}}{D(s)} \quad (97)$$

$$\frac{V_{HP}}{I_{in}} = \frac{s^2 C_1 C_3 \beta_{b2} R_{in}}{D(s)} \quad (98)$$

$$\frac{V_{BR}}{I_{in}} = -\frac{\begin{pmatrix} s^2 C_1 C_3 \beta_{b2} \\ + g_{mA1}^{(1)} g_{mB1}^{(1)} \beta_{a1} \beta_{b2} \gamma_{a1} \gamma_{b1} \end{pmatrix} R_{in}}{D(s)} \quad (99)$$

$$\frac{V_{AP}}{I_{in}} = -\frac{\begin{pmatrix} s^2 C_1 C_3 \beta_{b2} - sC_3 g_{mB1}^{(1)} \beta_{b2} \gamma_{b1} \\ + g_{mA1}^{(1)} g_{mB1}^{(1)} \beta_{a1} \beta_{b2} \gamma_{a1} \gamma_{b1} \end{pmatrix} R_{in}}{D(s)} \quad (100)$$

Where,

$$D(s) = s^2 C_1 C_3 + sC_3 g_{mB1}^{(1)} \beta_{a1} \gamma_{b1} + g_{mA1}^{(1)} g_{mB1}^{(1)} \beta_{a1} \beta_{b2} \gamma_{a1} \gamma_{b1} \quad (101)$$

The pole frequency (ω_o), quality factor (Q_o) and bandwidth (BW) are:

$$\omega_o = \sqrt{\frac{g_{mA1}^{(1)} g_{mB1}^{(1)} \beta_{a1} \beta_{b2} \gamma_{a1} \gamma_{b1}}{C_1 C_3}}, Q_o = \sqrt{\frac{C_1 g_{mA1}^{(1)} \beta_{b2} \gamma_{a1}}{C_3 g_{mB1}^{(1)} \beta_{a1} \gamma_{b1}}} \quad (102)$$

$$and\ BW = \frac{g_{mB1}^{(1)} \beta_{a1} \gamma_{b1}}{C_1}$$

Current Mode (CM):

$$\frac{I_{LP}}{I_{in}} = \frac{g_{mB2}^{(1)} g_{mB3}^{(1)} \gamma_{b2} \gamma_{b3}}{D(s)} \quad (103)$$

$$\frac{I_{BP}}{I_{in}} = \frac{sC_2 g_{mB2}^{(1)} \gamma_{b2}}{D(s)} \quad (104)$$

$$\frac{I_{HP}}{I_{in}} = \frac{s^2 C_1 C_2}{D(s)} \quad (105)$$

$$\frac{I_{BR}}{I_{in}} = \frac{s^2 C_1 C_2 + g_{mB2}^{(1)} g_{mB3}^{(1)} \gamma_{b2} \gamma_{b3}}{D(s)} \quad (106)$$

$$\frac{I_{AP}}{I_{in}} = \frac{s^2 C_1 C_2 - sC_2 g_{mB2}^{(1)} \gamma_{b2} + g_{mB2}^{(1)} g_{mB3}^{(1)} \gamma_{b2} \gamma_{b3}}{D(s)} \quad (107)$$

Transadmittance Mode (TAM) [with $I_{in1} = 0$]:

$$\frac{I_{LP}}{V_{in}} = \frac{g_{mB2}^{(1)} g_{mB3}^{(1)} \gamma_{b2} \gamma_{b3}}{D(s) R_{in}} \quad (108)$$

$$\frac{I_{BP}}{V_{in}} = \frac{sC_2 g_{mB2}^{(1)} \gamma_{b2}}{D(s) R_{in}} \quad (109)$$

$$\frac{I_{HP}}{V_{in}} = \frac{s^2 C_1 C_2}{D(s) R_{in}} \quad (110)$$

$$\frac{I_{BR}}{V_{in}} = \frac{s^2 C_1 C_2 + g_{mB2}^{(1)} g_{mB3}^{(1)} \gamma_{b2} \gamma_{b3}}{D(s) R_{in}} \quad (111)$$

$$\frac{I_{AP}}{V_{in}} = \frac{s^2 C_1 C_2 - sC_2 g_{mB2}^{(1)} \gamma_{b2} + g_{mB2}^{(1)} g_{mB3}^{(1)} \gamma_{b2} \gamma_{b3}}{D(s) R_{in}} \quad (112)$$

Where,

$$D(s) = s^2 C_1 C_2 + sC_2 g_{mB2}^{(1)} \gamma_{b2} + g_{mB2}^{(1)} g_{mB3}^{(1)} \gamma_{b2} \gamma_{b3} \quad (113)$$

The pole frequency (ω_o), quality factor (Q_o) and bandwidth (BW) are:

$$\omega_o = \sqrt{\frac{g_{mB2}^{(1)} g_{mB3}^{(1)} \gamma_{b2} \gamma_{b3}}{C_1 C_2}}, \quad Q_o = \sqrt{\frac{C_1 g_{mB3}^{(1)} \gamma_{b3}}{C_3 g_{mB2}^{(1)} \gamma_{b2}}} \quad (114)$$

$$and\ BW = \frac{g_{mB2}^{(1)} \gamma_{b2}}{C_1}$$

The transfer functions of Fig. 6 after considering non-idealities result:

Voltage mode:

$$\frac{V_{LP}}{V_{in}}=\frac{g_{mA1}^{(1)}g_{mB1}^{(1)}\left(\beta_{a1}+A_1\beta_{a3}\beta_{b1\gamma_{b1}}\right)\beta_{a1}\beta_{b2}\gamma_{a1}\gamma_{b1}}{D(s)} \quad (115)$$

$$\frac{V_{BP}}{V_{in}}=\frac{sC_3g_{mB1}^{(1)}\beta_{b2}\gamma_{B1}\left(\beta_{a1}+A_1\beta_{a3}\beta_{b1}\gamma_{b1}\right)}{D(s)} \quad (116)$$

$$\frac{V_{HP}}{V_{in}}=-\frac{s^2C_1C_3\beta_{b2}\left(\beta_{a1}+A_1\beta_{a3}\beta_{b1\gamma_{b1}}\right)}{D(s)} \quad (117)$$

$$\frac{V_{AP}}{V_{in}}=-\frac{\begin{pmatrix}s^2C_1C_3\beta_{b2}-sC_3g_{mB1}^{(1)}\beta_{b2}\gamma_{B1}\\+g_{mA1}^{(1)}g_{mB1}^{(1)}\beta_{a1}\beta_{b2}\gamma_{a1}\gamma_{b1}\end{pmatrix}}{D(s)} \quad (118)$$

$$\frac{V_{BR}}{V_{in}}=\frac{\begin{pmatrix}s^2C_1C_3\beta_{b2}\\+g_{mA1}^{(1)}g_{mB1}^{(1)}\beta_{a1}\beta_{b2}\gamma_{a1}\gamma_{b1}\end{pmatrix}\begin{pmatrix}\beta_{a1}\\+A_1\beta_{a3}\beta_{b1\gamma_{b1}}\end{pmatrix}}{D(s)} \quad (119)$$

$$\begin{aligned}D(s)=\;&s^2C_1C_3\beta_{b1}+sC_3g_{mB1}^{(1)}\beta_{a1}\gamma_{b1}(-\beta_{b1}^2\\&+\beta_{a1}\beta_{b2}\beta_{b3}+\beta_{a1}\beta_{b3}^2-\beta_{a2}\beta_{b3}\beta_{b1}\\&+\beta_{a3}\beta_{b2}\gamma_{b1}A_1+\beta_{a3}\beta_{b3}\gamma_{b1}A_1)\\&+g_{mA1}^{(1)}g_{mB1}^{(1)}\beta_{a1}\beta_{b2}\gamma_{a1}\gamma_{b1}\end{aligned} \quad (120)$$

The pole frequency (ω_o), quality factor (Q_o) and bandwidth (BW) are:

$$\omega_o=\sqrt{\frac{g_{mA1}^{(1)}g_{mB1}^{(1)}\beta_{a1}\beta_{b2}\gamma_{a1}\gamma_{b1}}{C_1C_3\beta_{b1}}},$$

$$\begin{aligned}Q_o=\;&\frac{1}{(-\beta_{b1}^2+\beta_{a1}\beta_{b2}\beta_{b3}}\sqrt{\frac{C_1g_{mA1}^{(1)}\beta_{b2}\gamma_{a1}}{C_3g_{mB1}^{(1)}\beta_{a1}\beta_{b1}\gamma_{b1}}}\\&+\beta_{a1}\beta_{b3}^2-\beta_{a2}\beta_{b3}\beta_{b1}\\&+\beta_{a3}\beta_{b2}\gamma_{b1}A_1\\&+\beta_{a3}\beta_{b3}\gamma_{b1}A_1)\\&g_{mB1}^{(1)}\beta_{a1}\gamma_{b1}(-\beta_{b1}^2+\beta_{a1}\beta_{b2}\beta_{b3}\\&+\beta_{a1}\beta_{b3}^2-\beta_{a2}\beta_{b3}\beta_{b1}\end{aligned} \quad (121)$$

$$and\ BW=\frac{+\beta_{a3}\beta_{b2}\gamma_{b1}A_1+\beta_{a3}\beta_{b3}\gamma_{b1}A_1)}{C_1\beta_{b1}}$$

Current mode:

$$\frac{I_{LP}}{I_{in}}=\frac{g_{mB2}^{(1)}g_{mB3}^{(1)}\gamma_{b2}\gamma_{b3}}{D(s)} \quad (122)$$

$$\frac{I_{BP}}{I_{in}}=\frac{sC_2g_{mB2}^{(1)}\gamma_{b2}}{D(s)} \quad (123)$$

$$\frac{I_{HP}}{I_{in}}=-\frac{s^2C_1C_2}{D(s)} \quad (124)$$

$$\frac{I_{BR}}{I_{in}}=\frac{s^2C_1C_2+g_{mB2}^{(1)}g_{mB3}^{(1)}\gamma_{b2}\gamma_{b3}}{D(s)} \quad (125)$$

$$\frac{I_{AP}}{I_{in}}=\frac{\left(s^2C_1C_2-sC_2g_{mB2}^{(1)}\gamma_{b2}+g_{mB2}^{(1)}g_{mB3}^{(1)}\gamma_{b2}\gamma_{b3}\right)}{D(s)} \quad (126)$$

Where,

$$\begin{aligned}D(s)=\;&s^2C_1C_2+\left(1+A_2\gamma_{a1}\alpha_a\right)sC_2g_{mB2}^{(1)}\gamma_{b2}\\&+g_{mB2}^{(1)}g_{mB3}^{(1)}\gamma_{b2}\gamma_{b3}\end{aligned} \quad (127)$$

The pole frequency (ω_o), quality factor (Q_o) and bandwidth (BW) are:

$$\omega_o=\sqrt{\frac{g_{mB2}^{(1)}g_{mB3}^{(1)}\gamma_{b2}\gamma_{b3}}{C_1C_2}},$$

$$Q_o=\frac{1}{\left(1+A_2\gamma_{a1}\alpha_a\right)}\sqrt{\frac{C_1g_{mB3}^{(1)}\gamma_{b3}}{C_2g_{mB2}^{(1)}\gamma_{b2}}} \quad (128)$$

$$and\ BW=\left(1+A_2\gamma_{a1}\alpha_a\right)\frac{g_{mB2}^{(1)}\gamma_{b2}}{C_1}$$

The transfer function of Fig. 7 after considering the non-idealities are obtained as:

Voltage mode (VM):

$$\frac{V_{LP}}{V_{in}}=-\frac{g_{mA1}^{(1)}g_{mB1}^{(1)}\begin{pmatrix}\beta_{a1}\\-A_1\beta_{a3}\beta_{b1\gamma_{b1}}\end{pmatrix}\beta_{a1}\beta_{b2}\gamma_{a1}\gamma_{b1}}{D(s)} \quad (129)$$

$$\frac{V_{BP}}{V_{in}}=\frac{sC_3g_{mB1}^{(1)}\beta_{b2}\gamma_{B1}\left(\beta_{a1}-A_1\beta_{a3}\beta_{b1\gamma_{b1}}\right)}{D(s)} \quad (130)$$

$$\frac{V_{HP}}{V_{in}}=\frac{s^2C_1C_3\beta_{b2}\left(\beta_{a1}-A_1\beta_{a3}\beta_{b1\gamma_{b1}}\right)}{D(s)} \quad (131)$$

$$\frac{V_{AP}}{V_{in}}=-\frac{\begin{pmatrix}s^2C_1C_3\beta_{b2}-sC_3g_{mB1}^{(1)}\beta_{b2}\gamma_{B1}\\+g_{mA1}^{(1)}g_{mB1}^{(1)}\beta_{a1}\beta_{b2}\gamma_{a1}\gamma_{b1}\end{pmatrix}}{D(s)} \quad (132)$$

$$\frac{V_{BR}}{V_{in}}=\frac{\begin{pmatrix}s^2C_1C_3\beta_{b2}\\+g_{mA1}^{(1)}g_{mB1}^{(1)}\beta_{a1}\beta_{b2}\gamma_{a1}\gamma_{b1}\end{pmatrix}\begin{pmatrix}\beta_{a1}\\-A_1\beta_{a3}\beta_{b1\gamma_{b1}}\end{pmatrix}}{D(s)} \quad (133)$$

Transimpedance mode (TIM):

$$\frac{V_{LP}}{I_{in}} = -\frac{g_{mA1}^{(1)} g_{mB1}^{(1)} R_{in} \begin{pmatrix} \beta_{a1} \\ -A_1 \beta_{a3} \beta_{b1\gamma_{b1}} \end{pmatrix} \beta_{a1} \beta_{b2} \gamma_{a1} \gamma_{b1}}{D(s)} \quad (134)$$

$$\frac{V_{BP}}{I_{in}} = \frac{sC_3 g_{mB1}^{(1)} R_{in} \beta_{b2} \gamma_{B1} \left(\beta_{a1} - A_1 \beta_{a3} \beta_{b1\gamma_{b1}} \right)}{D(s)} \quad (135)$$

$$\frac{V_{HP}}{I_{in}} = \frac{s^2 C_1 C_3 R_{in} \beta_{b2} \left(\beta_{a1} - A_1 \beta_{a3} \beta_{b1\gamma_{b1}} \right)}{D(s)} \quad (136)$$

$$\frac{V_{AP}}{I_{in}} = -\frac{\begin{pmatrix} s^2 C_1 C_3 \beta_{b2} - sC_3 g_{mB1}^{(1)} \beta_{b2} \gamma_{B1} \\ + g_{mA1}^{(1)} g_{mB1}^{(1)} \beta_{a1} \beta_{b2} \gamma_{a1} \gamma_{b1} \end{pmatrix} R_{in}}{D(s)} \quad (137)$$

$$\frac{V_{BR}}{I_{in}} = \frac{\begin{pmatrix} s^2 C_1 C_3 \beta_{b2} \\ + g_{mA1}^{(1)} g_{mB1}^{(1)} \beta_{a1} \beta_{b2} \gamma_{a1} \gamma_{b1} \end{pmatrix} \begin{pmatrix} \beta_{a1} \\ -A_1 \beta_{a3} \beta_{b1\gamma_{b1}} \end{pmatrix} R_{in}}{D(s)} \quad (138)$$

Where,

$$D(s) = s^2 C_1 C_3 + sC_3 g_{mB1}^{(1)} \beta_{a1} \gamma_{b1} \begin{pmatrix} 1 + \beta_{a2} \\ -\beta_{a3} \beta_{b2} \gamma_{b1} A_1 - \beta_{a3} \beta_{b3} \gamma_{b1} A_1 \end{pmatrix} + g_{mA1}^{(1)} g_{mB1}^{(1)} \beta_{a1} \beta_{b2} \gamma_{a1} \gamma_{b1} \quad (139)$$

The pole frequency (ω_o), quality factor (Q_o) and bandwidth (BW) are:

$$\omega_o = \sqrt{\frac{g_{mA1}^{(1)} g_{mB1}^{(1)} \beta_{a1} \beta_{b2} \gamma_{a1} \gamma_{b1}}{C_1 C_3}},$$

$$Q_o = \frac{1}{\begin{matrix} 1 + \beta_{a2} \\ -\beta_{a3} \beta_{b2} \gamma_{b1} A_1 - \beta_{a3} \beta_{b3} \gamma_{b1} A_1 \end{matrix}} \sqrt{\frac{C_1 g_{mA1}^{(1)} \beta_{b2} \gamma_{a1}}{C_3 g_{mB1}^{(1)} \beta_{a1} \beta_{b1} \gamma_{b1}}} \quad (140)$$

$$BW = \beta_{a1} \gamma_{b1} \begin{pmatrix} 1 + \beta_{a2} \\ -\beta_{a3} \beta_{b2} \gamma_{b1} A_1 - \beta_{a3} \beta_{b3} \gamma_{b1} A_1 \end{pmatrix} \frac{g_{mB1}^{(1)}}{C_1}$$

Current mode (CM):

$$\frac{I_{LP}}{I_{in}} = \frac{g_{mB2}^{(1)} g_{mB3}^{(1)} \gamma_{b2} \gamma_{b3}}{D(s)} \quad (141)$$

$$\frac{I_{BP}}{I_{in}} = \frac{sC_2 g_{mB2}^{(1)} \gamma_{b2}}{D(s)} \quad (142)$$

$$\frac{I_{HP}}{I_{in}} = \frac{s^2 C_1 C_2}{D(s)} \quad (143)$$

$$\frac{I_{BR}}{I_{in}} = \frac{s^2 C_1 C_2 + g_{mB2}^{(1)} g_{mB3}^{(1)} \gamma_{b2} \gamma_{b3}}{D(s)} \quad (144)$$

$$\frac{I_{AP}}{I_{in}} = \frac{\left(s^2 C_1 C_2 - sC_2 g_{mB2}^{(1)} \gamma_{b2} + g_{mB2}^{(1)} g_{mB3}^{(1)} \gamma_{b2} \gamma_{b3} \right)}{D(s)} \quad (145)$$

Transadmittance mode (TAM) [with $I_{in1} = 0$]:

$$\frac{I_{LP}}{V_{in}} = \frac{g_{mB2}^{(1)} g_{mB3}^{(1)} \gamma_{b2} \gamma_{b3}}{D(s) * R_{in}} \quad (146)$$

$$\frac{I_{BP}}{V_{in}} = \frac{sC_2 g_{mB2}^{(1)} \gamma_{b2}}{D(s) * R_{in}} \quad (147)$$

$$\frac{I_{HP}}{V_{in}} = \frac{s^2 C_1 C_2}{D(s) * R_{in}} \quad (148)$$

$$\frac{I_{BR}}{V_{in}} = \frac{s^2 C_1 C_2 + g_{mB2}^{(1)} g_{mB3}^{(1)} \gamma_{b2} \gamma_{b3}}{D(s) * R_{in}} \quad (149)$$

$$\frac{I_{AP}}{V_{in}} = \frac{\left(s^2 C_1 C_2 - sC_2 g_{mB2}^{(1)} \gamma_{b2} + g_{mB2}^{(1)} g_{mB3}^{(1)} \gamma_{b2} \gamma_{b3} \right)}{D(s) * R_{in}} \quad (150)$$

Where,

$$D(s) = s^2 C_1 C_2 + \left(1 + A_2 \gamma_{a1} \alpha_a \right) sC_2 g_{mB2}^{(1)} \gamma_{b2} + g_{mB2}^{(1)} g_{mB3}^{(1)} \gamma_{b2} \gamma_{b3} \quad (151)$$

The pole frequency (ω_o), quality factor (Q_o) and bandwidth (BW) are:

$$\omega_o = \sqrt{\frac{g_{mB2}^{(1)} g_{mB3}^{(1)} \gamma_{b2} \gamma_{b3}}{C_1 C_2}},$$

$$Q_o = \frac{1}{\left(1 + A_2 \gamma_{a1} \alpha_a \right)} \sqrt{\frac{C_1 g_{mB3}^{(1)} \gamma_{b3}}{C_2 g_{mB2}^{(1)} \gamma_{b2}}} \quad (152)$$

$$and\ BW = \left(1 + A_2 \gamma_{a1} \alpha_a \right) \frac{g_{mB2}^{(1)} \gamma_{b2}}{C_1}$$

The effects caused due to non-idealities can be easily observed from the above eqns. (102, 114, 121, 128, 140, 152). However, if transfer gains are close to unity, which is normally the case, then these equations may revert into the ideal forms.

4.2 Effects of parasitics

The non-ideal equivalent circuit of FD-CCCTA is shown in Fig. 8. Series resistance at X_A and X_B terminals are of low value. $(C_{Y1} \| R_{Y1})$, $(C_{Y2} \| R_{Y2})$, $(C_{Y3} \| R_{Y3})$,

$(C_{Y4} \| R_{Y4})$, are at Y_1, Y_2, Y_3, and Y_4 terminals, respectively while $(C_{ZA} \| R_{ZA})$, $(C_{ZB} \| R_{ZB})$, $(C_{OA1} \| R_{OA1})$, $(C_{OB1} \| R_{OB1})$, are at Z_A, Z_B, O_{A1}, and O_{B1} terminals. The values of R_{Y1}, R_{Y2}, R_{Y3}, R_{Y4}, R_{ZA}, R_{ZB}, R_{OA1}, R_{OB1} are high whereas C_{Y1}, C_{Y2}, C_{Y3}, C_{Y4}, C_{ZA}, C_{ZB}, C_{OA1}, C_{OB1} are low.

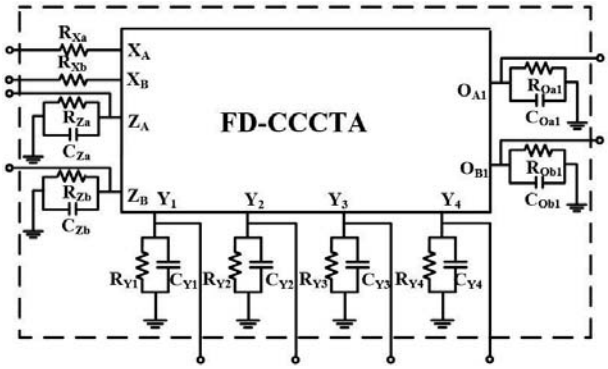

Figure 8: Non-ideal equivalent circuit of FD-CCCTA.

The non-ideal circuit of proposed mixed-mode filter is shown in Fig. 9 where impedances are:

$$Z_1 = \left(C_1' \left\| R_{Y1}^{(1)} \right\| R_{OB1}^{(1)}\right),\ Z_2 = (C_2' \| R_{OB2}^{(1)})$$

$$Z_3 = \left(C_3' \left\| R_{Y4}^{(1)} \right\| R_{OA1}^{(1)}\right),\ Z_4 = (C_{ZB}^{(1)} \| R_{ZB}^{(1)}),$$

$$Z_5 = (C_{ZA}^{(1)} \| R_{ZA}^{(1)})$$

$$Z_{in} = \left(C_{Y2}^{(1)} \left\| C_{Y3}^{(1)} \right\| R_{Y2}^{(1)} \left\| R_{Y3}^{(1)} \right\| R_{in}\right)$$

Where,

$$C_1' = C_1 + C_{OB1}^{(1)} + C_{Y1}^{(1)},\ C_2' = C_2 + C_{OB2}^{(1)},$$

$$C_3' = C_3 + C_{OA1}^{(1)} + C_{Y4}^{(1)}$$

The routine analysis of Fig. 9 results in:

Voltage Mode (VM):

$$\frac{V_{LP}}{V_{in}} = -\frac{g_{mA1}^{(1)} g_{mB1}^{(1)}}{D(s)} \tag{153}$$

$$\frac{V_{BP}}{V_{in}} = \frac{\left(sC_3' + \frac{1}{R_{Y4}} + \frac{1}{R_{OA1}}\right) g_{mB1}^{(1)}}{D(s)} \tag{154}$$

$$\frac{V_{HP}}{V_{in}} = \frac{\left(sC_1' + \frac{1}{R_{Y1}} + \frac{1}{R_{OB1}}\right)\left(sC_3' + \frac{1}{R_{Y4}} + \frac{1}{R_{OA1}}\right)}{D(s)} \tag{155}$$

$$\frac{V_{BR}}{V_{in}} = -\frac{\left(\left(sC_1' + \frac{1}{R_{Y1}} + \frac{1}{R_{OB1}}\right)\left(sC_3' + \frac{1}{R_{Y4}} + \frac{1}{R_{OA1}}\right) + g_{mA1}^{(1)} g_{mB1}^{(1)}\right)}{D(s)} \tag{156}$$

$$\frac{V_{AP}}{V_{in}} = -\frac{\left(\begin{array}{l}\left(sC_1' + \frac{1}{R_{Y1}} + \frac{1}{R_{OB1}}\right)\left(sC_3' + \frac{1}{R_{Y4}} + \frac{1}{R_{OA1}}\right) - \\ \left(sC_3' + \frac{1}{R_{Y4}} + \frac{1}{R_{OA1}}\right) g_{mB1}^{(1)} + g_{mA1}^{(1)} g_{mB1}^{(1)}\end{array}\right)}{D(s)} \tag{157}$$

Transimpedance Mode (TIM):

$$\frac{V_{LP}}{I_{in}} = -\frac{g_{mA1}^{(1)} g_{mB1}^{(1)} R_{in}}{D(s)} \tag{158}$$

$$\frac{V_{BP}}{I_{in}} = \frac{\left(sC_3' + \frac{1}{R_{Y4}} + \frac{1}{R_{OA1}}\right) g_{mB1}^{(1)} R_{in}}{D(s)} \tag{159}$$

$$\frac{V_{HP}}{I_{in}} = \frac{\left(sC_1' + \frac{1}{R_{Y1}} + \frac{1}{R_{OB1}}\right)\left(sC_3' + \frac{1}{R_{Y4}} + \frac{1}{R_{OA1}}\right) R_{in}}{D(s)} \tag{160}$$

$$\frac{V_{BR}}{I_{in}} = -\frac{\left(\left(sC_1' + \frac{1}{R_{Y1}} + \frac{1}{R_{OB1}}\right)\left(sC_3' + \frac{1}{R_{Y4}} + \frac{1}{R_{OA1}}\right) + g_{mA1}^{(1)} g_{mB1}^{(1)}\right) R_{in}}{D(s)} \tag{161}$$

$$\frac{V_{AP}}{I_{in}} = -\frac{\left(\begin{array}{l}\left(sC_1' + \frac{1}{R_{Y1}} + \frac{1}{R_{OB1}}\right)\left(sC_3' + \frac{1}{R_{Y4}} + \frac{1}{R_{OA1}}\right) - \\ \left(sC_3' + \frac{1}{R_{Y4}} + \frac{1}{R_{OA1}}\right) g_{mB1}^{(1)} + g_{mA1}^{(1)} g_{mB1}^{(1)}\end{array}\right) R_{in}}{D(s)} \tag{162}$$

Where,

$$D(s)=\left(sC_1'+\frac{1}{R_{Y1}}+\frac{1}{R_{OB1}}\right)\left(sC_3'+\frac{1}{R_{Y4}}+\frac{1}{R_{OA1}}\right)+\left(sC_3'+\frac{1}{R_{Y4}}+\frac{1}{R_{OA1}}\right)g_{mB1}^{(1)}+g_{mA1}^{(1)}g_{mB1}^{(1)} \quad (163)$$

Current Mode (CM):

$$\frac{I_{LP}}{I_{in}}=\frac{g_{mB2}^{(1)}g_{mB3}^{(1)}}{D(s)} \quad (164)$$

$$\frac{I_{BP}}{I_{in}}=\frac{\left(sC_2'+\frac{1}{R_{OB2}}\right)g_{mB2}^{(1)}}{D(s)} \quad (165)$$

$$\frac{I_{HP}}{I_{in}}=\frac{\left(sC_1'+\frac{1}{R_{Y1}}+\frac{1}{R_{OB1}}\right)\left(sC_2'+\frac{1}{R_{OB2}}\right)}{D(s)} \quad (166)$$

$$\frac{I_{BR}}{I_{in}}=\frac{\left(sC_1'+\frac{1}{R_{Y1}}+\frac{1}{R_{OB1}}\right)\left(sC_2'+\frac{1}{R_{OB2}}\right)+g_{mB2}^{(1)}g_{mB3}^{(1)}}{D(s)} \quad (167)$$

$$\frac{I_{AP}}{I_{in}}=\frac{\left(sC_1'+\frac{1}{R_{Y1}}+\frac{1}{R_{OB1}}\right)\left(sC_2'+\frac{1}{R_{OB2}}\right)-\left(sC_2'+\frac{1}{R_{OB2}}\right)g_{mB2}^{(1)}+g_{mB2}^{(1)}g_{mB3}^{(1)}}{D(s)} \quad (168)$$

Transadmittance Mode (TAM):

$$\frac{I_{LP}}{V_{in}}=\frac{g_{mB2}^{(1)}g_{mB3}^{(1)}}{D(s)*R_{in}} \quad (169)$$

$$\frac{I_{BP}}{V_{in}}=\frac{\left(sC_2'+\frac{1}{R_{OB2}}\right)g_{mB2}^{(1)}}{D(s)*R_{in}} \quad (170)$$

$$\frac{I_{HP}}{V_{in}}=\frac{\left(sC_1'+\frac{1}{R_{Y1}}+\frac{1}{R_{OB1}}\right)\left(sC_2'+\frac{1}{R_{OB2}}\right)}{D(s)*R_{in}} \quad (171)$$

$$\frac{I_{BR}}{V_{in}}=\frac{\left(sC_1'+\frac{1}{R_{Y1}}+\frac{1}{R_{OB1}}\right)\left(sC_2'+\frac{1}{R_{OB2}}\right)+g_{mB2}^{(1)}g_{mB3}^{(1)}}{D(s)*R_{in}} \quad (172)$$

$$\frac{I_{AP}}{V_{in}}=\frac{\left(sC_1'+\frac{1}{R_{Y1}}+\frac{1}{R_{OB1}}\right)\left(sC_2'+\frac{1}{R_{OB2}}\right)-\left(sC_2'+\frac{1}{R_{OB2}}\right)g_{mB2}^{(1)}+g_{mB2}^{(1)}g_{mB3}^{(1)}}{D(s)*R_{in}} \quad (173)$$

Where,

$$D(s)=\left(sC_1'+\frac{1}{R_{Y1}}+\frac{1}{R_{OB1}}\right)\left(sC_2'+\frac{1}{R_{OB2}}\right)+\left(sC_2'+\frac{1}{R_{OB2}}\right)g_{mB2}^{(1)}+g_{mB2}^{(1)}g_{mB3}^{(1)} \quad (174)$$

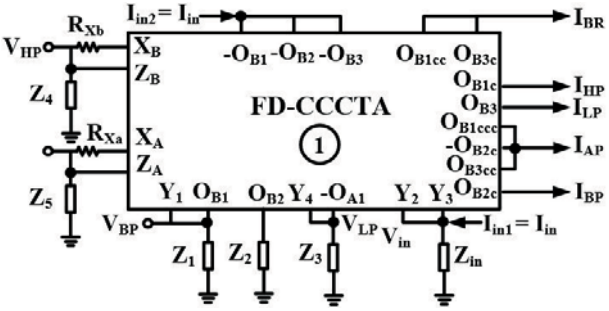

Figure 9: Non-ideal equivalent circuit of Fig. 3 with parasitics.

The non-ideal circuit of proposed mixed-mode first shadow filter (Fig. 6) is shown in Fig. 10, where impedances are:

$$Z_6=\left(C_{Y2}^{(1)}\left\|C_{Y3}^{(1)}\right.\|\left.R_{Y2}^{(1)}\right\|R_{Y3}^{(1)}\right),$$

$$Z_7=\left(C_{Y1}^{(2)}\left\|C_{ZB}^{(2)}\right.\|\left.R_{Y1}^{(2)}\right\|R_{ZB}^{(2)}\right),$$

$$Z_8=\left(C_{Y3}^{(2)}\left\|C_{OB}^{(2)}\right.\|\left.R_{Y3}^{(2)}\right\|R_{OB}^{(2)}\|R_1\right),$$

$$Z_9=(C_{ZA}^{(2)}\left|R_{ZA}^{(2)}\right|R_2),$$

The rest of the impedances are similar to the Fig. 8 The routine analysis of Fig. 10 results VM, and CM expressions due to the effect of parasitics as:

Voltage mode:

$$\frac{V_{LP}}{V_{in}}=\frac{g_{mA1}^{(1)}g_{mB1}^{(1)}\left(1+A_1\right)}{D(s)} \quad (175)$$

$$\frac{V_{BP}}{V_{in}}=\frac{\left(sC_3'+\frac{1}{R_{Y4}}+\frac{1}{R_{OA1}}\right)g_{mB1}^{(1)}\left(1+A_1\right)}{D(s)} \quad (176)$$

$$\left(sC_1'+\frac{1}{R_{Y1}}+\frac{1}{R_{OB1}}\right)$$

$$\frac{V_{HP}}{V_{in}}=-\frac{\left(sC_3'+\frac{1}{R_{Y4}}+\frac{1}{R_{OA1}}\right)\left(1+A_1\right)}{D(s)} \quad (178)$$

$$\frac{V_{AP}}{V_{in}}=-\frac{\left(\begin{array}{c}\left(sC_1'+\frac{1}{R_{Y1}}+\frac{1}{R_{OB1}}\right)\\ \left(sC_3'+\frac{1}{R_{Y4}}+\frac{1}{R_{OA1}}\right)-\\ \left(sC_3'+\frac{1}{R_{Y4}}+\frac{1}{R_{OA1}}\right)g_{mB1}^{(1)}\\ +g_{mA1}^{(1)}g_{mB1}^{(1)}\end{array}\right)}{D(s)} \quad (179)$$

$$\frac{V_{BR}}{V_{in}}=\frac{\left(\begin{array}{c}\left(sC_1'+\frac{1}{R_{Y1}}+\frac{1}{R_{OB1}}\right)\\ \left(sC_3'+\frac{1}{R_{Y4}}+\frac{1}{R_{OA1}}\right)\left(1+A_1\right)\\ +g_{mA1}^{(1)}g_{mB1}^{(1)}\end{array}\right)}{D(s)} \quad (180)$$

Where,

$$A_1=g_{mB}^{(2)}Z_8$$

$$D(s)=\left(sC_1'+\frac{1}{R_{Y1}}+\frac{1}{R_{OB1}}\right)\left(sC_3'+\frac{1}{R_{Y4}}+\frac{1}{R_{OA1}}\right)+2A_1\left(sC_3'+\frac{1}{R_{Y4}}+\frac{1}{R_{OA1}}\right)g_{mB1}^{(1)}+g_{mA1}^{(1)}g_{mB1}^{(1)}-I_{XA}^{(2)}Z_6 \quad (181)$$

Current mode:

$$\frac{I_{LP}}{I_{in}}=\frac{g_{mB2}^{(1)}g_{mB3}^{(1)}}{D(s)} \quad (182)$$

$$\frac{I_{BP}}{I_{in}}=\frac{\left(sC_2'+\frac{1}{R_{OB2}}\right)g_{mB2}^{(1)}}{D(s)} \quad (183)$$

$$\frac{I_{HP}}{I_{in}}=-\frac{\left(sC_1'+\frac{1}{R_{Y1}}+\frac{1}{R_{OB1}}\right)\left(sC_2'+\frac{1}{R_{OB2}}\right)}{D(s)} \quad (184)$$

$$\left(sC_1'+\frac{1}{R_{Y1}}+\frac{1}{R_{OB1}}\right)\left(sC_2'+\frac{1}{R_{OB2}}\right)$$

$$\frac{I_{BR}}{I_{in}}=\frac{+g_{mB2}^{(1)}g_{mB3}^{(1)}}{D(s)} \quad (185)$$

$$\left(sC_1'+\frac{1}{R_{Y1}}+\frac{1}{R_{OB1}}\right)\left(sC_2'+\frac{1}{R_{OB2}}\right)$$

$$\frac{I_{AP}}{I_{in}}=\frac{-\left(sC_2'+\frac{1}{R_{OB2}}\right)g_{mB2}^{(1)}+g_{mB2}^{(1)}g_{mB3}^{(1)}}{D(s)} \quad (186)$$

Where,

$$D(s)=\left(sC_1'+\frac{1}{R_{Y1}}+\frac{1}{R_{OB1}}\right)\left(sC_2'+\frac{1}{R_{OB2}}\right)+\left(1+A_2\right)\left(sC_2'+\frac{1}{R_{OB2}}\right)g_{mB2}^{(1)}+g_{mB2}^{(1)}g_{mB3}^{(1)} \quad (187)$$

$$and\ A_2=g_{mA}^{(2)}Z_9$$

Similarly, the non-ideal circuit of proposed mixed-mode second shadow filter (Fig. 7) is shown in Fig. 11, where impedances are:

$$Z_7=\left(C_{Y1}^{(2)}\parallel R_{Y1}^{(2)}\parallel R_{in}\right),\ Z_{10}=(C_{ZB}^{(2)}\parallel R_{ZB}^{(2)})$$

While rest of the impedances are similar to the Fig. 8 and Fig. 9. The routine analysis of Fig. 11 results VM, TIM, CM, and TAM expressions due to the effect of parasitics as follows:

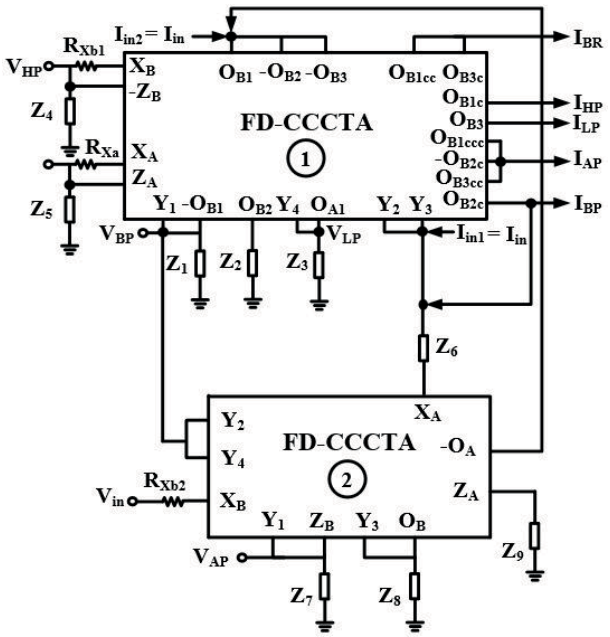

Figure 10: Non-ideal equivalent circuit of Fig. 6 with parasitics.

Voltage mode (VM):

$$\frac{V_{LP}}{V_{in}}=-\frac{g_{mA1}^{(1)}g_{mB1}^{(1)}\left(1-A_1\right)}{D(s)} \quad (188)$$

$$\frac{V_{BP}}{V_{in}}=\frac{\left(sC_3'+\frac{1}{R_{Y4}}+\frac{1}{R_{OA1}}\right)g_{mB1}^{(1)}\left(1-A_1\right)}{D(s)} \quad (189)$$

$$\frac{V_{HP}}{V_{in}}=\frac{\left(sC_3'+\frac{1}{R_{Y4}}+\frac{1}{R_{OA1}}\right)\left(1-A_1\right)}{D(s)} \quad (190)$$

$$\frac{V_{BR}}{V_{in}}=\frac{\left(\begin{array}{c}\left(sC_1'+\frac{1}{R_{Y1}}+\frac{1}{R_{OB1}}\right)\\ \left(sC_3'+\frac{1}{R_{Y4}}+\frac{1}{R_{OA1}}\right)\\ +g_{mA1}^{(1)}g_{mB1}^{(1)}\end{array}\right)\left(1-A_1\right)}{D(s)} \quad (191)$$

$$\frac{V_{AP}}{V_{in}}=-\frac{\left(\begin{array}{c}\left(sC_1'+\frac{1}{R_{Y1}}+\frac{1}{R_{OB1}}\right)\\ \left(sC_3'+\frac{1}{R_{Y4}}+\frac{1}{R_{OA1}}\right)\\ -\left(sC_3'+\frac{1}{R_{Y4}}+\frac{1}{R_{OA1}}\right)g_{mB1}^{(1)}\\ +g_{mA1}^{(1)}g_{mB1}^{(1)}\end{array}\right)}{D(s)} \quad (192)$$

Transimpedance mode (TIM):

$$\frac{V_{LP}}{I_{in}}=-\frac{g_{mA1}^{(1)}g_{mB1}^{(1)}R_{in}\left(1-A_1\right)}{D(s)} \quad (193)$$

$$\frac{V_{BP}}{I_{in}}=\frac{\left(sC_3'+\frac{1}{R_{Y4}}+\frac{1}{R_{OA1}}\right)g_{mB1}^{(1)}R_{in}\left(1-A_1\right)}{D(s)} \quad (194)$$

$$\frac{V_{HP}}{I_{in}}=\frac{\left(sC_1'+\frac{1}{R_{Y1}}+\frac{1}{R_{OB1}}\right)\left(sC_3'+\frac{1}{R_{Y4}}+\frac{1}{R_{OA1}}\right)\left(1-A_1\right)R_{in}}{D(s)} \quad (195)$$

$$\frac{V_{BR}}{I_{in}}=\frac{\left(\begin{array}{c}\left(sC_1'+\frac{1}{R_{Y1}}+\frac{1}{R_{OB1}}\right)\\ \left(sC_3'+\frac{1}{R_{Y4}}+\frac{1}{R_{OA1}}\right)\\ +g_{mA1}^{(1)}g_{mB1}^{(1)}\end{array}\right)R_{in}\left(1-A_1\right)}{D(s)} \quad (196)$$

$$\frac{V_{AP}}{I_{in}}=-\frac{\left(\begin{array}{c}\left(sC_1'+\frac{1}{R_{Y1}}+\frac{1}{R_{OB1}}\right)\\ \left(sC_3'+\frac{1}{R_{Y4}}+\frac{1}{R_{OA1}}\right)-\\ \left(sC_3'+\frac{1}{R_{Y4}}+\frac{1}{R_{OA1}}\right)g_{mB1}^{(1)}\\ +g_{mA1}^{(1)}g_{mB1}^{(1)}\end{array}\right)R_{in}}{D(s)} \quad (197)$$

Where,

$$A_1 = g_{mB}^{(2)} Z_8$$

$$D(s) = \left(sC_1' + \frac{1}{R_{Y1}} + \frac{1}{R_{OB1}}\right)\left(sC_3' + \frac{1}{R_{Y4}} + \frac{1}{R_{OA1}}\right) + 2(1-A_1)\left(sC_3' + \frac{1}{R_{Y4}} + \frac{1}{R_{OA1}}\right) g_{mB1}^{(1)} + g_{mA1}^{(1)} g_{mB1}^{(1)} - I_{XA}^{(2)} Z_6 \quad (198)$$

Current mode (CM):

$$\frac{I_{LP}}{I_{in}} = \frac{g_{mB2}^{(1)} g_{mB3}^{(1)}}{D(s)} \quad (199)$$

$$\frac{I_{BP}}{I_{in}} = \frac{\left(sC_2' + \frac{1}{R_{OB2}}\right) g_{mB2}^{(1)}}{D(s)} \quad (200)$$

$$\frac{I_{HP}}{I_{in}} = \frac{\left(sC_1' + \frac{1}{R_{Y1}} + \frac{1}{R_{OB1}}\right)\left(sC_2' + \frac{1}{R_{OB2}}\right)}{D(s)} \quad (201)$$

$$\frac{I_{BR}}{I_{in}} = \frac{\left(sC_1' + \frac{1}{R_{Y1}} + \frac{1}{R_{OB1}}\right)\left(sC_2' + \frac{1}{R_{OB2}}\right) + g_{mB2}^{(1)} g_{mB3}^{(1)}}{D(s)} \quad (202)$$

$$\frac{I_{AP}}{I_{in}} = \frac{\left(sC_1' + \frac{1}{R_{Y1}} + \frac{1}{R_{OB1}}\right)\left(sC_2' + \frac{1}{R_{OB2}}\right) - \left(sC_2' + \frac{1}{R_{OB2}}\right) g_{mB2}^{(1)} + g_{mB2}^{(1)} g_{mB3}^{(1)}}{D(s)} \quad (203)$$

Transadmittance mode (TAM):

$$\frac{I_{LP}}{V_{in}} = \frac{g_{mB2}^{(1)} g_{mB3}^{(1)}}{D(s) * R_{in}} \quad (204)$$

$$\frac{I_{BP}}{V_{in}} = \frac{\left(sC_2' + \frac{1}{R_{OB2}}\right) g_{mB2}^{(1)}}{D(s) * R_{in}} \quad (205)$$

$$\frac{I_{HP}}{V_{in}} = \frac{\left(sC_1' + \frac{1}{R_{Y1}} + \frac{1}{R_{OB1}}\right)\left(sC_2' + \frac{1}{R_{OB2}}\right)}{D(s) * R_{in}} \quad (206)$$

$$\frac{I_{BR}}{V_{in}} = \frac{\left(sC_1' + \frac{1}{R_{Y1}} + \frac{1}{R_{OB1}}\right)\left(sC_2' + \frac{1}{R_{OB2}}\right) + g_{mB2}^{(1)} g_{mB3}^{(1)}}{D(s) * R_{in}} \quad (207)$$

$$\frac{I_{AP}}{V_{in}} = \frac{\left(sC_1' + \frac{1}{R_{Y1}} + \frac{1}{R_{OB1}}\right)\left(sC_2' + \frac{1}{R_{OB2}}\right) - \left(sC_2' + \frac{1}{R_{OB2}}\right) g_{mB2}^{(1)} + g_{mB2}^{(1)} g_{mB3}^{(1)}}{D(s) * R_{in}} \quad (208)$$

Where,

$$D(s) = \left(sC_1' + \frac{1}{R_{Y1}} + \frac{1}{R_{OB1}}\right)\left(sC_2' + \frac{1}{R_{OB2}}\right) + (1+A_2)\left(sC_2' + \frac{1}{R_{OB2}}\right) g_{mB2}^{(1)} + g_{mB2}^{(1)} g_{mB3}^{(1)} \quad (209)$$

$$and\ A_2 = g_{mA}^{(2)} Z_9$$

The above eqns. (153-209) show the effect of parasitics in the proposed mixed-mode filter, mixed-mode first shadow filter, and mixed-mode second shadow filter. However, the effect of parasitic capacitance can be neglected by suitably choosing the value of C_1, C_2, and

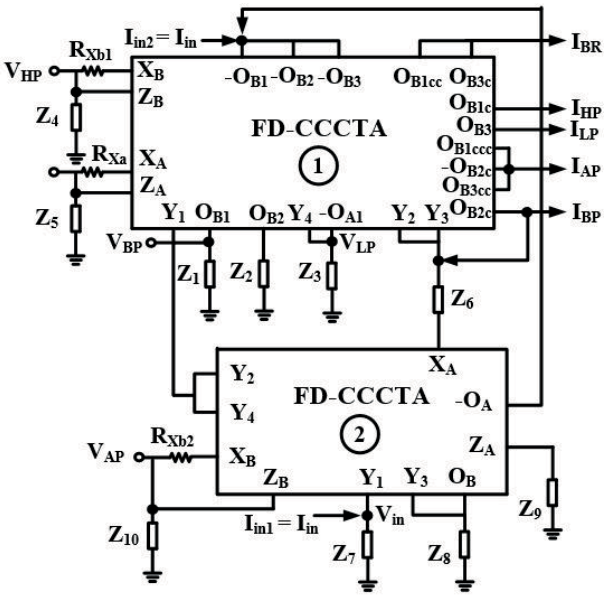

Figure 11: Non-ideal equivalent circuit of Fig. 7 with parasitics.

C_3 . While parasitic resistances, except R_X, can be easily neglected as it is high valued in the order of few MΩ.

5 Comparative analysis

The non-shadow mixed-mode universal filter is compared to state of the art in section 5.1, followed by section 5.2, wherein mixed-mode shadow filters are compared.

5.1 Comparison with the existing SIMO mixed-mode non-shadow universal filters

Table 3 compares the proposed filter with the existing SIMO mixed-mode biquad non-shadow universal filters. All the topologies use more than one active building block except [11] and the proposed one. Moreover, more passive components are used in [3, 7, 10, 11] than in the proposed one. Further, one or more passive components are floating in [3, 6, 7, 10, 11]. The filters [3, 7, 8] require matching components to realize the responses. Additional circuitry is required to obtain the simultaneous responses for the VM in [4, 5, 8, 10, 12], TAM in [3, 5-8, 11], CM in [3-7, 11, 12], and TIM in [4, 5, 12]. Independent tuning of ω_o and Q_o is not possible in [5, 6, 9, 10], and electronic tuning is not possible in [3, 7, 8, 10, 11]. The topologies [3, 6, 9] consume less power than this work. However most of the filters are found to be partially cascadable including the proposed ones, only ref. [8] is fully cascadable.

5.2 Comparison with the existing different modes of shadow filters

Table 4 compares the proposed mixed-mode shadow filters with the existing literature. It is noted that there is no report of any mixed-mode shadow filters realization using the same topology in literature except the proposed one. The topologies [13-20] realize only VM responses. Similarly, topologies [21-28] realize only CM responses, and [29] realizes only TIM and TAM responses. Whereas the proposed mixed-mode shadow filter realizes all the mixed-mode filters without alteration of the topology. The comparison Table 4 is self-explanatory for other parameters and features.

6 Simulated results and discussions

The functionality of the proposed non-shadow and shadow mixed-mode filters is verified through the Cadence virtuoso spectre circuit simulator using TSMC

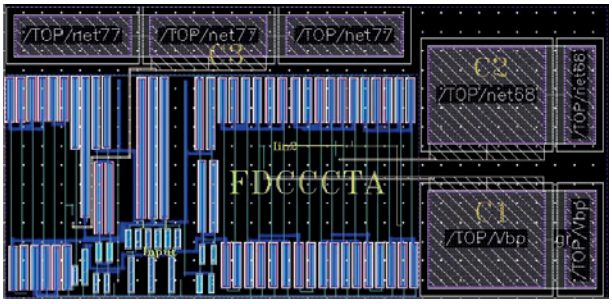

Figure 12: The layout of the proposed mixed-mode universal filter (Fig. 3).

180 nm technology. The DC biasing levels of FD-CCCTA are taken as $V_{DD} = 1.2$ V, $V_{SS} = -1.2$V, $V_{bp} = V_{bn} = 0$, $I_{bias1} = 25$ µA, $I_{bias2} = 20$ µA, and $I_{B1} = I_{A1} = 50$ µA. Table 1 gives the aspect ratios of the transistors. The non-shadow filter of Fig. 3 is implemented with passive components chosen as $C_1 = C_2 = C_3 = 1$ pF, and $R_{in} = 1$ Ω. Fig. 12 shows the layout of the mixed-mode universal filter of Fig. 3, which occupies an area of 158.5 µm x 76.3 µm. For the VM and TIM, the pre-layout and post-layout gain responses of LP, HP, BP, and BR are shown in Fig. 13 (a), and the gain and the phase responses of AP are shown in Fig. 13 (b). Similarly, the responses for CM and TAM are shown in Fig. 14. The calculated pole frequency and the qual-

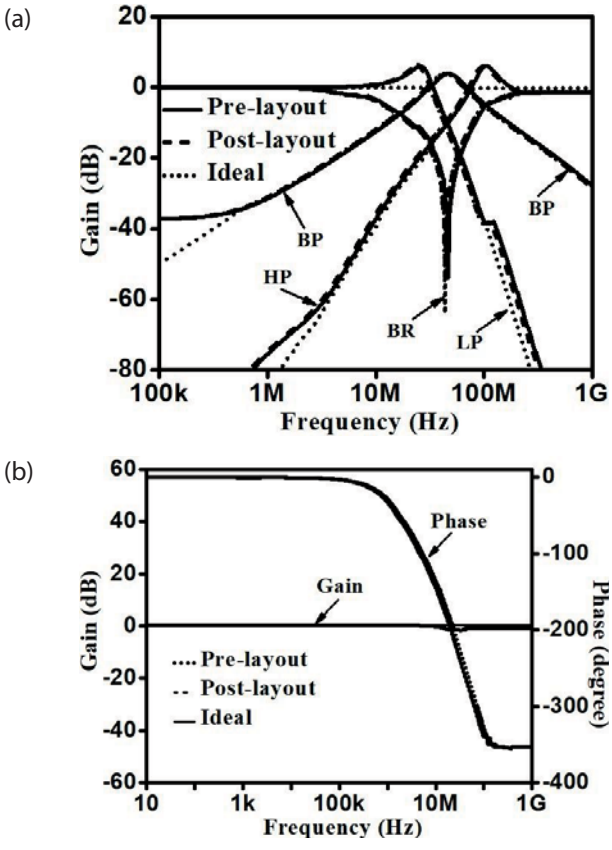

Figure 13: Simulated results of VM and TIM (Fig. 7) (a) gain responses of the LP, HP, BP, and BR (b) gain and phase responses of the AP filter.

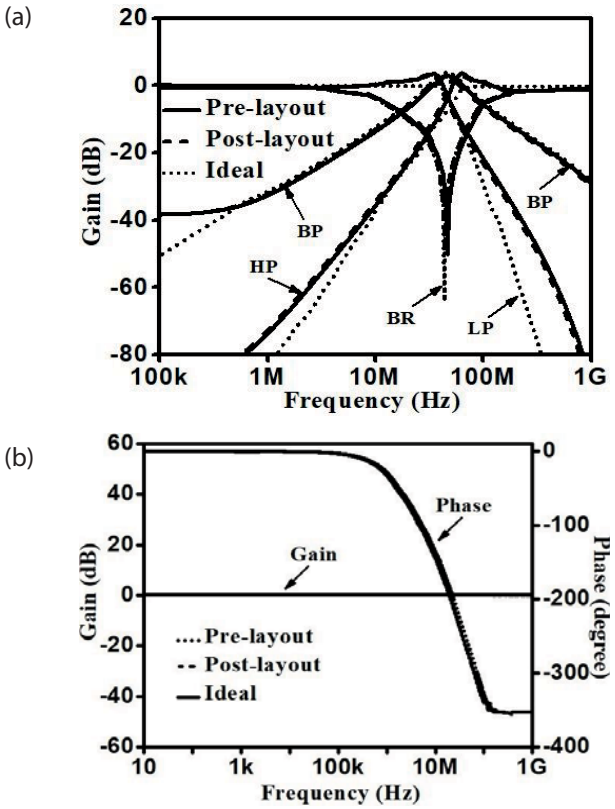

Figure 14: Simulated results of shadow CM and TAM (Fig. 7) (a) gain responses of the LP, HP, BP, BR (b) gain, and phase response of the AP filter.

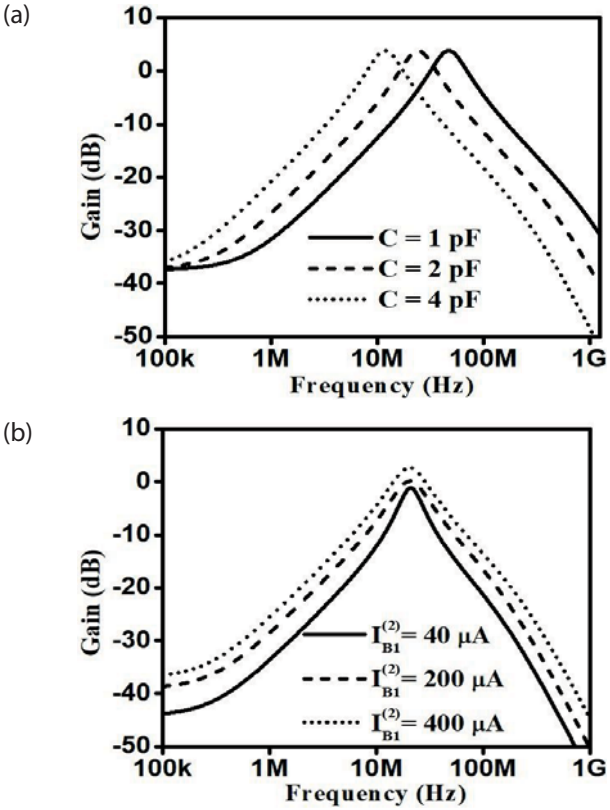

Figure 15: Simulated results of the VM shadow filter (Fig. 6) (a) tuning of fo due to capacitor value C, (b) tunability of Q, and gain due to A_1.

Table 3: Comparative analysis with the existing SIMO mixed-mode universal filters.

Ref.	No. & type of active elements used	No. of passive elements (R/C), All grounded elements (Yes/No)	Matching comp. req.	Simultaneous responses obtained {Input Imp./ Output Imp.}				Independent tuning of ω_o & Q_o	Electronic tuning	Power Cons. (mW)	Fully Cascadable
				VM	TAM	CM	TIM				
3.	2, FDCCII	4/2, No	Yes	UF {H/H}	LP, BP, HP {H/H}	LP, BP, HP, BR {H/H}	UF {H/H}	Yes	No	1.32	No
4.	3, CCCCTA	0/2, Yes	No	LP, BP, HP, BR {H/H}	UF {H/H}	LP, BP, HP {L/H}	LP, BP, HP {L/H}	Yes	Yes	1.99	No
5.	4, OTA	0/2, Yes	No	LP, BP, HP {H/H}	LP, BP, HP {H/H}	LP, BP, HP {H/H}	LP, BP, HP {H/H}	No	Yes	NA	No
6.	6, OTA	1/2, No	No	UF {L/H}	BP, HP {L/H}	BP, HP, BR {H/H}	UF {H/H}	No	Yes	1.57	No
7.	3, DDCC	4/2, No	Yes	UF {H/H}	LP, BP, HP {H/H}	LP, BP, HP {H/H}	UF {H/H}	Yes	No	NA	No
8.	3, DVCC, 6 MOS	0/2, 6 MOSs, Yes	Yes	LP, BP, BR {H/L}	LP, BP, HP {H/H}	LP, BP, HP {L/H}	LP, BP {L/L}	Yes	No	NA	Yes
9.	3, OTA 3, Diff. OTA	0/2, Yes	No	UF {H/H}	UF {H/H}	UF {H/H}	UF {H/H}	No	Yes	0.075	No
10.	3, FTFN	3/2, No	No	LP, BP, HP {L/H}	LP, BP, HP {L/L}	LP, BP, HP {L/L}	LP, BP, HP {L/H}	No	No	NA	No
11.	1, FDCCII	3/2, No	No	UF {L/H}	BP, HP {L/H}	BP, HP, BR {H/H}	UF {H/H}	Yes	No	NA	No
12.	5, MCCCII	0/2, Yes	No	LP, BP, HP {L/H}	LP, BP, HP {H/L}	LP, BP, HP {H/H}	LP, BP, HP {H/H}	Yes	Yes	NA	No
This work	1, FDCCCTA (Fig. 3)	1/3, Yes	No	LP, BP, HP {H/H}	UF {H/H}	UF {H/H}	LP, BP, HP {H/H}	Yes	Yes	1.9	No

Table 4: Comparative analysis with the existing different modes of shadow filters.

Ref.	No. & type of active elements used	No. of passive elements (R/C), All grounded elements (Yes/No)	Simultaneous responses obtained {Input Imp./ Output Imp.}				Independent tuning of w_o & Q_o	Electronic tuning	Power Cons. (mW)	Fully Cascadable
			VM	TAM	CM	TIM				
13.	4, CFOA	7/2, No	HP {H/H}	------	------	------	No	No	NA	No
14.	5, CFOA	9/2, No	BP {H/L}	------	------	------	Yes	No	NA	Yes
*15.	6, CFOA	10/2, No	LP, BP, HP, BR {H/L}	------	------	------	Yes	No	NA	Yes
16.	3, OTRA	11/4, No	LP, BP {H/H}	------	------	------	No	No	NA	No
17.	3, VDDDA	1/2, Yes	UF {H/H}	------	------	------	Yes	Yes	NA	No
18.	4, DDCC	5/2, Yes	LP, BP, HP {H/H}	------	------	------	Yes	No	NA	No
*19.	2, OP-AMP	2/2, No	LP, BP, HP, BR {NA}	------	------	------	NA	NA	NA	No
20.	2, DDCC 1, Amplifier	2/2, Yes	BP {L/H}	------	------	------	Yes	Yes	NA	Yes
21.	2, CDTA 1, CA	0/2, No	------	------	BP {L/H}	------	Yes	Yes	NA	Yes
22.	3, CDTA	1/2, Yes	------	------	LP, BP(C), HP(C) {L/L}	------	Yes	Yes	5.9	No
23.	4, ECCII	2/2, No	------	------	BP {L/L}	------	Yes	No	NA	No
24.	4, OFCC	5/2, Yes	------	------	BP {L/H}	------	Yes	No	NA	Yes
25.	2, CDTA	2/2, No	------	------	BP(C) {H/L}	------	Yes	No	7.79	No
26.	2, CDTA 1, TA	1/2, Yes	------	------	LP(R), BP {L/L}	------	Yes	Yes	21.2	No
27.	3, CC-CDCTA 1, CCII	0/2, No	------	------	UF {L/H}	------	Yes	Yes	2.23	Yes
28.	1, CCCTA, 1, EX-CCCTA	0/2, Yes	------	------	UF {L/H}	------	Yes	Yes	4.1	Yes
*29.	4, OFCC	5/2, No	------	BP{H/H}	------	BP {L/L}	No	No	NA	Yes
This work	2, FDCCCTA (Fig. 6)	0/3, 4 MOSs, Yes	LP, BP, HP, AP {L/H}	------	UF {H/H}	------	Yes	Yes	3.7	No
	2, FDCCCTA (Fig. 7)	1/3, 4 MOSs, Yes	LP, BP, HP, AP {H/H}	UF{H/H}	UF {H/H}	LP, BP, HP, AP {H/H}				No

NOTE: *Different structures are required to obtain each filter response; BP(C), HP(C) & LP (R): Represent the availability of responses through capacitors (C) and resistors (R); hence require additional circuitry for practical implementation; H: High; L: Low.

ity factor are 46.22 MHz and 1, respectively, while the simulated pre-layout and post-layout frequencies are 46.45 MHz and 45.98 MHz, respectively.

The simulation for the mixed-mode shadow filter of Fig. 7 is performed with the same parameters as used for the non-shadow filter along with $I_{B1}^{(2)} = I_{A1}^{(2)} = 40$ µA, $R_1 = R_2 = 1.38$ kΩ. The simulated gain responses of LP, HP, BP, and BR are shown in Fig. 13 (a), and the gain and the phase responses of AP are shown in Fig. 13 (b) for the VM and TIM. Similarly, the responses for CM and TAM are shown in Fig. 14. The simulated f_0 and the Q are 46.41 MHz and 1.1 vis-a-vis the calculated values of 46.41 MHz and 0.95.

The tunability of f_0 along with BW for constant Q can be obtained by varying $C_1 = C_3 = C$. The simulated responses for the mixed-mode shadow filter of Fig. 6, using C = 1 pF, 2 PF, and 4 pF, are shown in Fig. 15 (a). The simulated f_0s are obtained as 46.45 MHz, 23.19 MHz, and 11.75 MHz vis-à-vis the calculated values of 46.22 MHz, 23.11 MHz, and 11.55 MHz, respectively. The simulated BWs are 46.41 MHz, 23.42 MHz, and 11.86 MHz vis-à-vis the calculated BWs are 46.68 MHz, 23.34 MHz, and 11.66 MHz, respectively. Fig. 15 (b) shows the tunability

of the quality factor along with the gain of the BP filter by the variation of gain A_1, i.e., varying $g_{mB}^{(2)}$ in line with (46). The resulted quality factors are 0.8, 1.1, 1.3 and the gains are -1.2 dB, +1.4 dB, +3.7 dB for $I_{B1}^{(2)} = 40\ \mu A, 200\ \mu A, \text{and } 400\ \mu A$, respectively.

The performance of the circuit is affected due to the fabrication process and mismatch deviation which has been analysed for the BP output response. Monte Carlo (MC) simulation for 200 runs is performed by considering the deviation of standard parameters of MOSs. Fig. 16 (a) shows the MC results for the frequency response of BP in VM and TIM while Fig. 16 (b) shows for the same in CM and TAM. Fig. 17 (a) shows the histogram plot of the distribution of samples for center frequency in VM and TIM which results the standard deviation as 2.7 MHz. While, Fig. 17 (b) shows for the CM and TAM which results the standard deviation of 2.9 MHz.

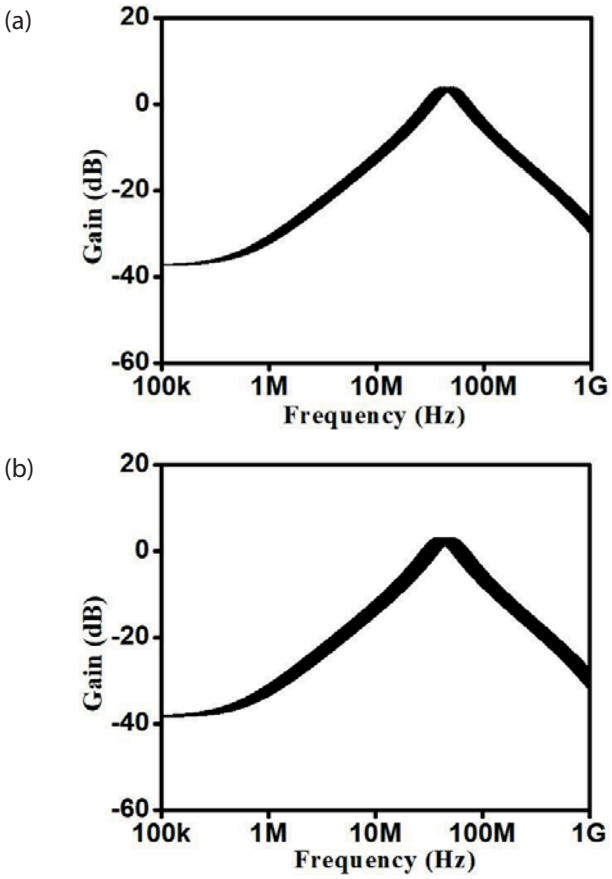

Figure 16: Monte Carlo simulation for 200 runs for BP output response (a) VM and TIM (b) CM and TAM.

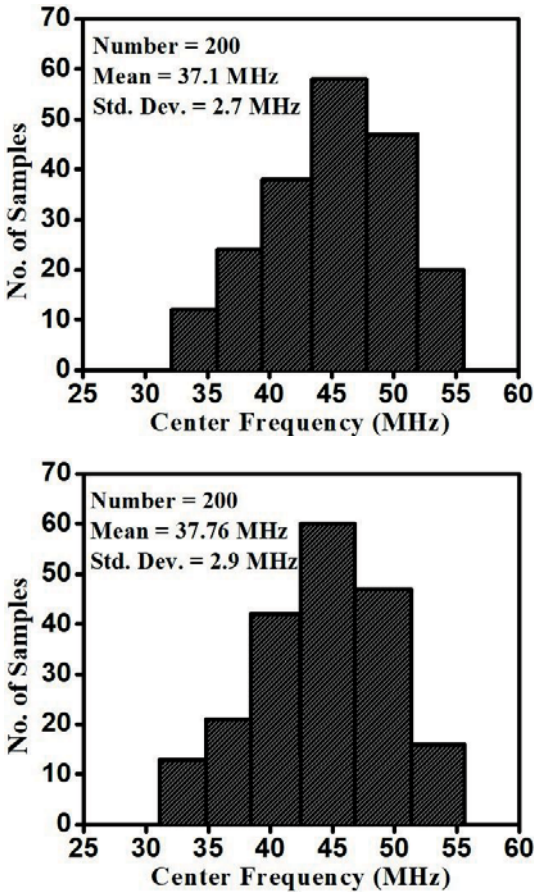

Figure 17: Statistical results of Monte Carlo simulation for BP output response (a) VM and TIM (b) CM and TAM.

The PVT analysis has also been done for the Fast Fast (FF), nominal, and Slow Slow (SS) corners. Voltage has been varied in the range of 1.2 V ± 10 %. Whereas, temperatures have been taken as -40 °C, 27 °C, and 125 °C for the FF, nominal, and SS corners, respectively. Fig. 18 (a) shows for all the three corners which results in the centre frequencies of 53.5 MHz, 46.41 MHz, 40.32 MHz in the FF, nominal, and SS corners, respectively in the VM and TIM mode. While, Fig. 18 (b) shows the similar results in CM and TAM mode which gives the centre frequencies as 55.7 MHz, 46.41 MHz, 39.97 MHz.

The measure of %THD (% total harmonic distortion) for the HP and LP mixed-mode shadow filter as a function of the input signal is shown in Fig. 19. The %THD variation is less than 5% for VM and CM filters up to 600mA and 1000mA, as shown in Fig. 19 (a) and Fig. 19 (b), respectively.

7 Conclusions

This paper presents a novel mixed-mode universal filter using a single active building block, FD-CCCTA, a new

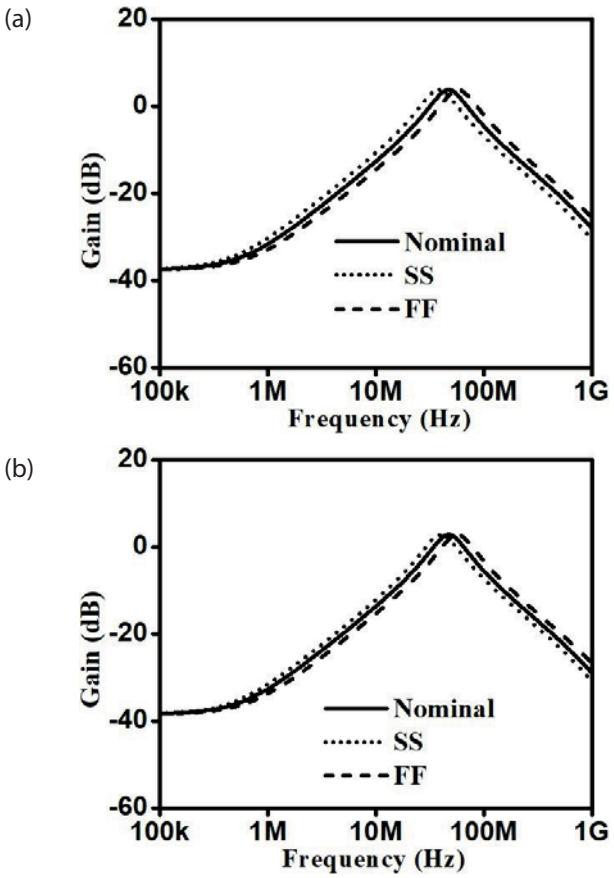

Figure 18: Simulated frequency responses of BP filter in fast, nominal, and slow corners (a) VM and TIM (b) CM and TAM.

variant of FD-CCII, and three capacitors. All the standard responses such as LP, BP, HP, BR, and AP are obtained in all VM, CM, TIM, and TAM modes. It is then extended to shadow filters to add flexibility in the orthogonal tuning of filter parameters, such as pole frequency (ω), quality factor (Q), and the tuning of the filter's gain. The first proposed shadow-filter circuit realizes the VM and CM UFs, while the second shadow filter realizes UFs for all the four modes, such as CM, TAM, VM, and TIM. To the best of the authors' knowledge, there is no reporting of a mixed-mode shadow filter in literature. The theoretical results are verified using TSMC 180 nm technology in Cadence Virtuoso Spectre.

8 Conflict of interest

The authors declare that there is no conflict of interest for this paper. Also, there are no funding supports for this manuscript.

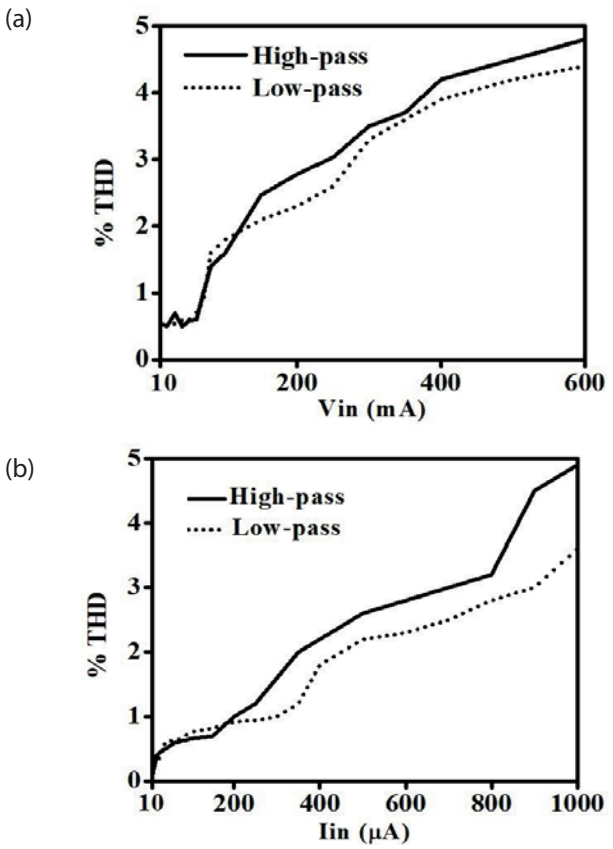

Figure 19: %THD variation of HP and LP Shadow filter (Fig. 6) (a) VM (b) CM.

9 References

1. M. Parvizi, "Design of a new low power MISO multi-mode universal biquad OTA-C filter," Int. J. Elec, vol. 106, no. 3, pp. 440-454, 2018,.
2. M. Kumngern, P. Suwanjan, K. Dejhan, "Electronically tunable voltage-mode universal filter with single-input five output using simple OTAs," Int. J. Elec, vol. 100, no. 8, pp. 1118-1133, 2012.
3. B. Chaturvedi, J. Mohan, A. Kumar, "A new versatile universal biquad configuration for emerging, signal processing applications," J.Circ. Syst. Comp, vol. 27, no. 12, pp. 1-28, 2018..
4. H. P. Chen, W. S. Yang, "Electronically tunable current controlled current conveyor transconductance amplifier-based mixed-mode biquadratic filter resistorless and grounded capacitors," Appl. Sci, vol. 7, pp. 1-22, 2017.
5. M.A. Ibrahim, "Design and analysis of a mixed-mode universal filter using dual-output operational transconductance amplifiers (DO-OTAs). Proceedings of the international conference on computer and communication engineering, pp. 915-918, 2008.
6. M. Kumngern, S. Junnapiya, "Mixed-mode universal filter using OTAs," Proceedings of the 2012 IEEE

international conference on cyber technology in automation, control and intelligent systems, pp. 119-122, 2012.
7. W.B. Liao, J.C. Gu, "SIMO type universal mixed-mode biquadratic filter." Indian Journal of Engineering & Materials Sciences, vol. 18, pp. 443-448.
8. S. Minaei, M.A. Ibrahim, "A mixed-mode KHN-biquad using DVCC and grounded passive elements suitable for direct cascading," Int. J. Circ. Theor. Appl, vol. 37, no. 7, pp. 793-810, 2009.
9. M. Parvizi, A. Taghizadeh, H. Mahmoodian, Z.D. Kozehkanani, "A low-power mixed-mode SIMO universal g_m-C filter," J. Circ. Syst. Comp, vol. 26, no. 10, pp. 1-16, 2017.
10. N.A. Shah, M.A. Malik, "Multifunction mixed-mode filter using FTFNs," Analog Integr. Circ. Sig. Process, vol. 47, pp. 339-343, 2006.
11. C.N. Lee, C.M. Chang, "Single FDCCII-based mixed-mode biquad filter with outputs," AEU-Int. J. Electron. Comm., vol. 63, pp. 736-742, 2009.
12. L. Zhijun, "Mixed-mode universal filter using MC-CCII," AEU-Int. J. Electron. Comm, vol. 63, pp. 1072-1075, 2009.
13. M.T. Abuelma'atti, N. Almutairi, "New CFOA-based shadow bandpass filter," In: 15th international conference on electronics, information, and communications, 2016.
14. M.T. Abuelma'atti, N. Almutairi, "New voltage-mode bandpass shadow filter," In: 13th international multi-conference on systems, signals & devices, pp. 412-415, 2016.
15. M.T. Abuelma'atti, N.R. Almutairi, "New current-feedback operational amplifier based shadow filters," Analog Integr. Circ. Sig. Process, vol. 86, pp. 471-480, 2016.
16. R. Anurag, R. Pandey, N. Pandey, M. Singh, M. Jain, "OTRA based shadow filters," Annual IEEE India Conference, 2016.
17. P. Huaihongthong, A. Chaichana, P. Suwanjan, S. Siripongdee, W. Sunthonkanokpong, P. Supavarasuwat, W. Jaikla, F. Khateb, "Single-input multiple-output voltage-mode shadow filter based on VDDDAs," AEU-Int. J. Electron. Commun, vol. 103, pp. 13-23.
18. F. Khateb, W. Jaikla, T. Kulej, M. Kumngern, D. Kubanek, "Shadow filters based on DDCC," IET Circuits Devices Syst, vol. 11, pp. 631-637, 2017.
19. S.C. Roy, "Shadow filters: a new family of electronically tunable filters," IETE J. Edu, vol. 51, pp. 75-78, 2010.
20. A. Yesil, F. Kacar, "Band-pass filter with high quality factor based on current differencing transconductance amplifier and current amplifier" AEU-Int. J. Electron. Commun, vol. 75, pp. 63-69, 2017.
21. A. Yesil, F. Kacar, S. Minaei, "Electronically controllable bandpass filters with high quality factor and reduced capacitor value: an additional approach" AEU-Int. J. Electron. Commun. vol. 70, pp. 936-943, 2016.
22. M. Atasoyu, H. Kuntman, B. Metin, N. Herencsar, O. Cicekoglu, "Design of current-mode class 1 frequency-agile filter employing CDTAs," European conference on circuit theory and design, 2015.
23. M. Atasoyu, B. Metin, H. Kuntman, N. Herencsar, "New current-mode class 1 frequency-agile filter for multi-protocol GPS application," Elektronika IR Elektrotechnika, vol. 21, pp. 35-39, 2015.
24. D. Nand, N. Pandey, "New configuration for OFCC-based CM SIMO filter and its application as shadow filter," Arab. J. Sci. Eng. Vol. 43, pp. 3011-3022, 2018.
25. N. Pandey, R. Pandey, R. Choudhary, A. Sayal, M. Tripathi, "Realization of CDTA based frequency agile filters," IEEE international conference on signal processing computing and control, 2013.
26. N. Pandey, A. Sayal, R. Choudhary, R. Pandey, "Design of CDTA and VDTA based frequency agile filters," Adv. Electron, pp. 1-14, 2014.
27. D. Singh, S.K. Paul, "Realization of current-mode universal shadow filter," AEU-Int. J. Electron. Commun, vol. 117, pp. 153088, 2020.
28. D. Singh, S.K. Paul, "Improved current-mode biquadratic shadow universal filter," Inf. MIDEM-J. Microelectron. Electron. Compon. Mater, vol. 52, no. 1, pp. 51-66, 2022.
29. D. Nand, N. Pandey, V. Bhanoo, A. Gangal, "Operational floating current conveyor based TAM & TIM shadow filter," Proceedings of 4th international conference on computer and management ICCM, pp. 103-115, 2018.
30. F. Gur, F. Anday, "Simulation of a novel current-mode universal filter using FDCCIIs," Analog Integr. Circ. Sig. Process, vol. 60, pp. 231-236, 2009.
31. Y. Lakys, A. Fabre, "Shadow filters-new family of second order filters," Electron Lett, vol. 46, no. 4, pp. 985-986, 2010.
32. V. Biolkova, D. Biolek, "Shadow filters for orthogonal modification of characteristics frequency and bandwidth," Electronics Letters, vol. 46, no. 12, pp. 830-831, 2010.
33. M. Kumngern, T. Nonthaputha, F. Khateb, "Arbitrary waveform generators using current-controlled current conveyor transconductance amplifier and current conveyor analog switches," J. Circ. Syst. Comp, vol. 28, no. 11, pp. 1950179, 2019.

Arrived: 31. 07. 2022
Accepted: 24. 11. 2022

Original scientific paper
https://doi.org/10.33180/InfMIDEM2022.405

Informacije MIDEM
Journal of Microelectronics,
Electronic Components and Materials
Vol. 52, No. 4(2022), 263 – 269

User Offloading using Hybrid NOMA in Next-generation Heterogeneous Network

Deepa Palani[1], Merline Arulraj[2]

[1]Department of Electronics and Communication Engineering, Sethu Institute of Technology, Virudhunagar District, India
[2]Department of Electronics and Communication Engineering, Sethu Institute of Technology, Virudhunagar District, India

Abstract: Millimeter wave (mmWave) enabled Heterogeneous network (Hetnet) has become ubiquitous because of the great demand of mobile network applications. Non–Orthogonal multiple access (NOMA) bids a desired possible assistance, for example condensed inactivity with great consistency, enhanced spectrum efficiency and considerable affinity. NOMA is envisioned to be used with small cells enabled with mmWave environment. This work proposes an ubiquitous connectivity between users at the cell edge and offloading macro cell so as to provide features the macro cell itself cannot cope with, such as extreme changes in the required user data rate and energy efficiency.The amount of inter-cell and performance is analyzed in the boundary and in the midpoint of the cell. It shows a reduction in outage possibility of 90% for cell center user (CCU) and 48% for cell edge user (CEU). Thereby alleviating dead zones and energy efficient support is shown for transmission using carrier sensing NOMA.

Keywords: Heterogeneous network; millimeter wave; Non-Orthogonal multiple access; Small cells

Uporabniška razbremenitev z uporabo hibridnega NOMA v heterogenem omrežju naslednje generacije

Izvleček: Heterogeno omrežje (Hetnet) z milimetrskim valovanjem (mmWave) je postalo vseprisotno zaradi velikega povpraševanja po mobilnih omrežnih aplikacijah. Neortogonalni večkratni dostop (NOMA) ponuja želeno možno pomoč, na primer zgoščeno neaktivnost z veliko doslednostjo, izboljšano učinkovitostjo spektra in veliko naklonjenostjo. NOMA naj bi se uporabljal z majhnimi celicami, ki jih omogoča okolje mmWave. To delo predlaga vseprisotno povezavo med uporabniki na robu celice in razbremenitev makrocelice, da se zagotovijo funkcije, ki jih makrocelica sama ne more obvladati, kot so ekstremne spremembe zahtevane hitrosti prenosa podatkov uporabnikov in energetske učinkovitosti. Pokaže se zmanjšanje možnosti izpada za 90 % za uporabnika v središču celice (CCU) in 48 % za uporabnika na robu celice (CEU). S tem se ublažijo mrtve cone in prikaže energetsko učinkovita podpora za prenos z uporabo zaznavanja nosilcev NOMA

Ključne besede: Heterogeno omrežje; milimetrski valovi; neortogonalni večkratni dostop; majhne celice

** Corresponding Author's e-mail: venkatdeepa129@gmail.com*

1 Introduction

Fifth generation (5G) cellular networks require up to about a thousand times (1000x) more surface capacity than current long-term networks. In view of its benefits sub-channel allocation is adapted using the orthogonal frequency division multiple access (OFDM) multiplexing technique. [1] Achieving wireless multiple access on OFDM-based systems is implemented in two ways - orthogonal frequency division multiple access (OMA) [2] and non-orthogonal multiple access (NOMA) [3]. By exploiting the multi-user diversity gain, system throughput can be exploited in OMA [4]. It relies on the known channel state information of all sub-channels and accordingly sub-channel allocation is done for only one user. Regardless of the throughput system,

How to cite:
D. Palani et al., "User Offloading using Hybrid NOMA in Next-generation Heterogeneous Network", Inf. Midem-J. Microelectron. Electron. Compon. Mater., Vol. 52, No. 4(2022), pp. 263–269

OMA has a disadvantage when communicating at very high data speeds. It does not allow frequency reuse in a cell [5], since a subcarrier in an OFDMA cell is allocated to only one user, which limits the sum data rate of the cell significantly. Unlike OFDMA, NOMA technique allocates a subcarrier to more than one user at a time in a cell, which ensures higher throughput due to sub-carrier reuse and therefore NOMA is considered as a major enabler for the next-generation heterogeneous networks. [6,7]The convergence of fixed and mobile access networks can be resolved by the NOMA access network. The system should allow the transmission of numerous types of broadband telecommunication traffic since the end user desires wireless broadband access. [8] The congestion is reduced in traditional wireless networks by offloading with small cells in Hetnet.

1.1 Motivation

In order to improve the system performance, it is very stringent to use a single technology, e.g. Connectivity and the data-rate. NOMA utilizes the knowledge of superposition coding and successive interference cancellation in the transmitter and receiver. [9]. NOMA works in conjunction with various radio interface technologies, such as multi-cell scenarios, millimeter wave [10] and reconfigurable antenna systems [11], and other Internet of things platforms. NOMA technology is used with beamforming technology to improve the device to device communication in the small cell environment [12]. NOMA accomplishes this by multiplexing various transmitted signals into a stream of single signals by taking advantage of the power domain area. In view of the user centric point, successive interference cancellation (SIC) is the technique to receive the desired signal information and the remaining signals are disposed to remove interference. The request for execution of SIC is controlled by the expanding user channel state information (CSI) [13], i.e., the user is considered as the strong cell center user with high channel gain, this part is known as a cell center user (CCU), to unravel and offset data of the low-gain users, this part alluded to as a cell edge user (CEU). As of now, the utilization of NOMA in Hetnet includes device- to-device spectrum allocation and power control.Significantly three methodologies are utilized. In the cooperative NOMA near users (i.e CCU) is utilized to assist a distant user (i.e CEU). The second strategy is to introduce fairness among users by using design variables such as weighted sum-rate and the last strategy is to maintain the minimum requirement of the CEU. Therefore NOMA is treated as a transfer to help far users in wireless communication.[14]

Therefore, the first challenge is to obtain the CSI of the co-channel users. There is strong residual interference among NOMA users without the knowledge of CSI of the interference, reliable communications is questionable. The second challenge is to remove the interference from the different signals of the co-channel users. A novel Interference cancellation technique is necessary to feat information of and suppresses the interference from all the overlapping symbols of the co-interference. It is accomplished using spectrum reuse techniques with NOMA known as user-pairing algorithm.The intra-cell interference is reduced and limited by using spectrum reuse techniques with Hybrid NOMA known as user-pairing algorithm. The contributions are as follows,

- The user-pairing algorithm is applied to cancel out co-channel interference thereby achieving increased sum rate
- Analyzing outage probability for the CCU and CEU thereby achieving offloading macrocells.
- A novel interference cancellation is exploited to reduce intracell and intercell interference thereby achieving spectral efficiency.

2 System model

A two-tier hetnet is considered where the macro and small base stations (BSs) are situated in the focal point of the cell and its inclusion region is a circle of range R. The BS serves Cell User equipment's (CUEs) which are consistently circulated in the inclusion region. The precoding can be utilized to control the obstruction caused among the CUEs. The uplink system model for the nth user access is shown in Fig.1, where small cell environment is shown with cluster of users categorized into CCU and CEU. N is the total number of users in the cell, and N ≥ 2M. The total number of antennas employed at the BS is represented as M. User equipment (UE) is attached with a single antenna. The different bandwidths allocated to UE in the OMA and hybrid NOMA schemes are demonstrated in Fig.2. The hybrid NOMA is served for different users irrelevant to position simultaneously in the same frequency. The femtocell user equipments (fCUE)are indicated in sub-channel which is assisted by femto BSs and indicated as macrocell user equipments (mCUE) in sub-channel which are assisted by macro BSs. The channel fading coefficients of UEs are assumed as

$$h_1^f > h_2^f > h_3^f > h_4^f \ldots\ldots\ldots > h_N^f \quad (1)$$

Where $h_1^f \ldots\ldots h_N^f$ represents the channel fading coefficient of strong signals in ascending order. Thus, in the given scenario, the received signals of the cluster group of uplink (UL) users, y, are given by,

$$y = h_{iN}^{f} x_{iN} + \sum_{l=1, l\neq i}^{N} \sqrt{p_l^f x_l^f} + n_{iN} \quad (2)$$

Where

$$x_{iN} = \sqrt{p_{iN}^f x_{iN}^f}$$

is the desired signal term transmitted symbol and power assigned to UE. $\sqrt{p_l^f x_l^f}$ is the interference from the other symbols n_{iN} denoted as the additive white Gaussian noise (AWGN) with variance σ^2.[15]

2.1 Path loss Model

The mmWave propagation environment is modeled by widely adopted distance dependent path loss model and is given as

$$L_{mm}(r) = \rho + 10\alpha \log(r) + \chi_{mm} \quad (3)$$

In the given equation ρ = 32.4 + 20*log* (f_c) where f_c represents the mmWave carrier frequency and the distance is represented as r. χ_{mm} is the shadow fading in mmWave link. The path loss exponent is denoted as α. [16]

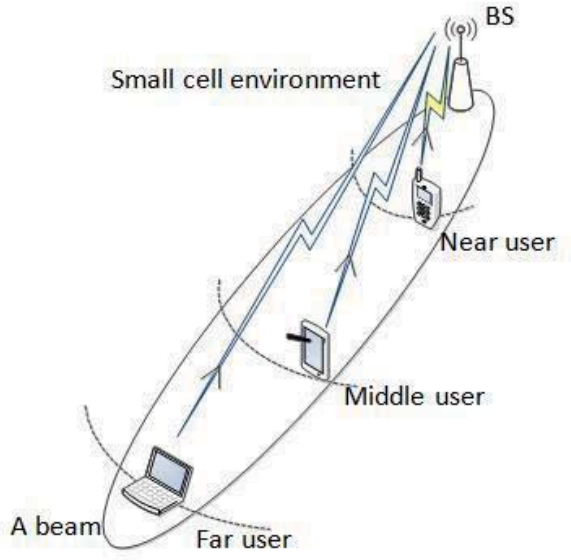

Figure 1: The System model of uplink NOMA-Hetnet

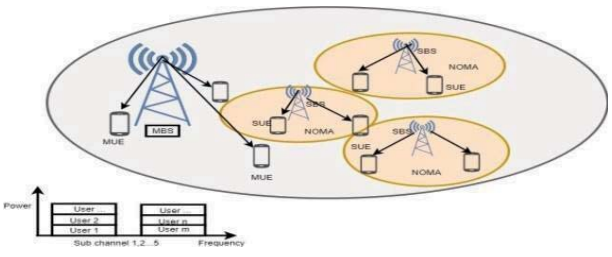

Figure 2: Energy efficient NOMA based HetNets [15]

NOMA uses a successive interference cancellation (SIC) technique to correctly demodulate signals at the receiver since it can allocate a subchannel to several users. The goal of differentiating users is achieved by SIC's ability to remove interference in a certain order based on the power of various users. We presume that every terminal is fully aware of the channel state data (CSI). The uplink channel estimate in time division mode can provide with transmitter-side channel estimation, which can be used to obtain receiver-side channel estimation. Additionally, since one of our optimization goals for the given system is to maximise total harvested energy, we can infer that gathered energy somehow falls below the receiver saturation threshold.

2.2 Performance metrics

The performance of mmWave enabled Hetnet is analyzed based on the metrics as Signal to Interference plus Noise Ratio (SINR), followed by Sum-Rate of an UE and Energy efficiency. Successive detection is carried out in descending order; The SINR is given as

$$SINR_{iN} = \frac{p_{iN}^f x_{iN}^f \left|h_{iN}^f\right|^2 L_{mm}(r)}{\left|h_{lN}^f\right|^2 \sum_{l=i+1}^{N} p_{lN}^f + \sigma^2} \quad (4)$$

The achievable rate of NOMA UL user is denoted as

$$R_{iN} = B \log_2 \left(1 + \frac{p_{iN}^f x_{iN}^f \left|h_{iN}^f\right|^2 L_{mm}(r)}{\left|h_{lN}^f\right|^2 \sum_{l=i+1}^{N} p_{lN}^f + \sigma^2}\right) \quad (5)$$

where B is the bandwidth of mmWave enabled hetnets. The conventional OMA sum rate is obtained as

$$R_{iN} = B/N \log_2 \left(1 + \frac{p_{iN}^f x_{iN}^f \left|h_{iN}^f\right|^2 L_{mm}(r)}{\left|h_{lN}^f\right|^2 \sum_{l=i+1}^{N} p_{lN}^f + \sigma^2}\right) \quad (6)$$

The important parameter metric is energy efficiency (EE) of the Hetnet. The objective is to target the decreased power consumption so as to increase the overall EE of a network.EE is maximized by optimizing the power allocation coefficients.

$$EE = \frac{Acheivable\ data\ rate(bps)}{Total\ power\ consumption\left(\frac{Joule}{s}\right)} \quad (7)$$

Total Power consumption is derived as

$$P_{Total}^f = \frac{1}{\varepsilon_p} \sum \beta_{iN}^f p_{iN}^f + \sum P_{st}^f \quad (8)$$

The first component represented the dynamic power of femto BS which constituted the dissipation of power amplifiers. The term $\varepsilon_p \in \{0,1\}$ denoted the power amplifier efficiency of the femto BS. β_{iN}^f is the fair power allocation ratio. The second component represents static power which is consumed by the transmitted signals and operating components.

3 Hybrid NOMA user-pairing algorithm

Multiple users are supported by NOMA simultaneously in the same frequency in hybrid NOMA. Hybrid NOMA is a combined technique of OMA and NOMA,the users per carrier is increased indefinitely without compromising sum rate. A user-pairing primarily based totally suboptimal scheme. It is a proposed hybrid NOMA where different access schemes are combined with NOMA to facilitate the deployment. A user-pairing algorithm for Hybrid NOMA is served in different time slots to offload macrocell and to assure the quantity of accessed users.

Hybrid NOMA user-pairing algorithm is derived to perform multiplexing of more than two users in the same frequency carrier to accommodate more users in hetnet. The user-pairing is done for two scenarios based on the distances of UEs. The user is considered as strong and weak according to the cell position.

Near users is a strong one whereas far users are weaker. In order to offload the macro cell, small cells are assigned to provide ubiquitous connectivity using a user-pairing algorithm.

This work aims to maximise the system's overall energy efficiency while reducing the system's energy consumption. As a result, this formula expresses the link between the system sum rate and overall power consumption. We also take the base station with the energy harvesting unit into account when allocating the subchannel and power resource.

Hybrid NOMA User-Pairing Algorithm	
Initialize	a) Set of users $Ui = \{1,2,3....N\}$ b) Set of sub-channels $S = \{1,2,3.....K\}$ c) Set the sub-channel power allocation coefficient β_{iN}^f d) Set of power values
Ensure	The number of split sub-channels k, the user-pairing strategy a) Near-Far user pairing (N-F) b) Near-near, far-far user pairing (N-N, F-F)
Sort	Sort transmission powers in ascending order. Assume P1< P2< ::: <Pn.
Order	Channel conditions as $\left\|h_1^f\right\|^2 > \left\|h_2^f\right\|^2 > \left\|h_3^f\right\|^2 > \left\|h_4^f\right\|^2$
Choose	Power allocation coefficient $\beta_{iN}^f = 1 \forall Ui$
Obtain	Sum Rate
	End if

Here the far user is given the higher fraction of power whereas the near users are given lower fraction of power. But the cumulative result should not be exceeded 1. For example $\beta_{i1}^f = 0.75 and\ \beta_{i2}^f = 0.25$ for two users are assigned. The higher fraction of power is given to the far users. The distances are assumed for far user is d_1=1000 *meters* and near user is d_2=500 *meters*.

4 Results and discussion

Simulation results are furnished to assess the overall performance of hybrid NOMA Hetnet.The overall performance of user-pairing hybrid NOMA schemes has been explored in which we have CCU and CEU ,i.e three UEs in a cell. The parameters are listed in table 1.

Table 1: Evaluation Parameters

Parameter	Default Value
Macro Transmit Power	46 dBm
Femto Transmit Power	18 dBm
Macrocell radius	500 m
Femtocell radius	50 m
Number of fCUE in each femtocell	3
Number of mCUE in macrocell	3
Shadowing standard deviation	10 dB
System Bandwidth	100 MHz
mmWave carrier frequency	28 GHz
Noise power spectral density	-174 dBm/Hz

The transmit power of macrocells and femtocells and their coverage radius are listed. The total number of macro CUEs and femto CUEs are listed as well. However we have evaluated the scenario by increasing the number of UEs.

The proposed user-pairing algorithm offloading CEUs and fair power allocation solutions is evaluated through hybrid NOMA user-pairing algorithm and compared with the OMA strategies. Fig. 3, is portrayed

sum capacity in terms of their transmit Signal to noise Ratio (SNR). It is clear from Fig. 3 that hybrid NOMA scheme provides better sum-rate when compared to other schemes in perfect SIC mode. This performance is due to their distinct channel conditions, when the near strongest user (CCU) is paired with the far weak user (CEU), an achievable good sum rate is arrived. The improvement is not significant when pairing near-near and far-far, but still the sum rate performance is better compared to TDMA. The Single carrier NOMA (SC-NOMA) is not up to the level when compared to TDMA and hybrid NOMA. This is due to the overloading of users in the same carrier.

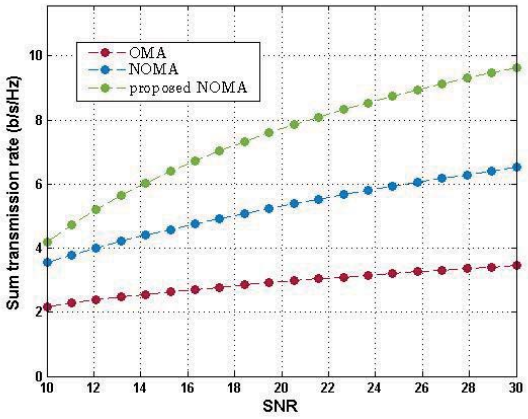

Figure 3: Sum rate comparison between proposed hybrid NOMA scheme with OMA schemes

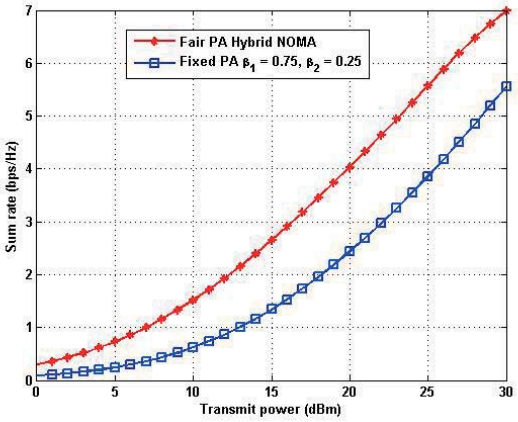

Figure 4: Sum rate comparison between proposed hybrid NOMA scheme with fixed power allocation.

Power allocation factor is the next important parameter that has the peculiar impact in the design performance of hybrid NOMA; hence evaluation is based on the distance between near user and BSs respectively. In Fig. 4 increasing transmitted power produces better sum rate capacity in the midst of lower SNRs. Thereby near user's power to far users' powers raises interference, for this reason fixed power allocation cannot be

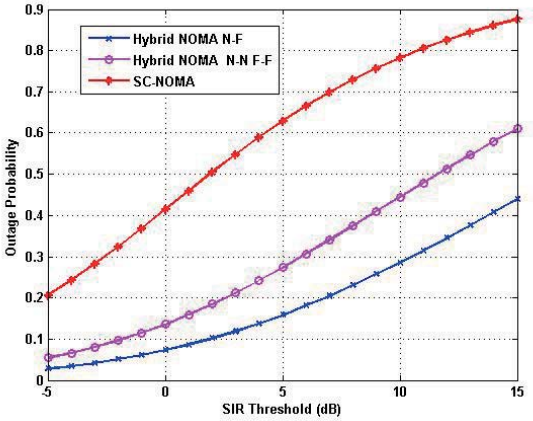

Figure 5: Outage Probability Vs SIR threshold

increased arbitrarily. An unconstraint maximization problem is used to find the optimal power-splitting ratio that returns the maximum instantaneous system throughput.

Fig. 5 shows that outage is increased when the Signal to Interference Ratio (SIR)increases. When the distance increases, the outage probability is also increased for the multiple input multiple output (MIMO)-NOMA system. The greater the distance leads to greater interference.To examine the impact on outage performance, the transmit SNR of the two users is set to be equal and varied from 0 to 60 dB. The figure shows that, at a power ratio of 15 dB, both users' outage performance achieves an interference-limited floor at a transmit SNR of roughly 15 dB, and that additional increases in transmit SNR have no effect on the users' outage probability performance.

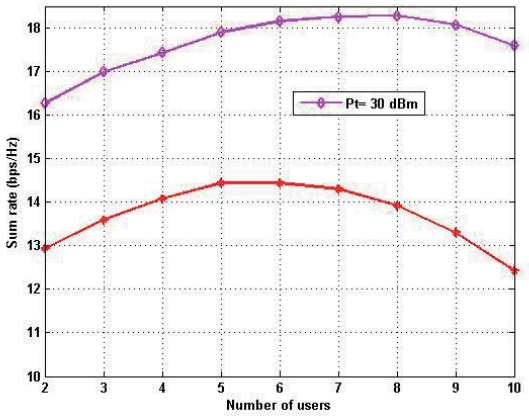

Figure 6: Sum rate comparison vs Number of users

Fig.6 is a sum rate comparison when the number of users increased. This sum rate is the outcome of user-pairing algorithm. It can be compared for individual CCU, CEU and middle users. The first user's signal becomes much stronger than the second user's signal

as the power ratio between the users rises, and many of the first user's symbol estimates are highly likely to be accurate.

The cluster comparison is given in Fig.7.Hybrid NOMA is a beneficial strategy for uplink transmission in future wireless communications since it can solve a significant issue with OMA-based techniques, which is to not allow frequency reuse inside one cell. The impact of power allocation on NOMA communications led to the development of the unique hybrid NOMA technique which can take use of both the near-far effect and frequency reuse.

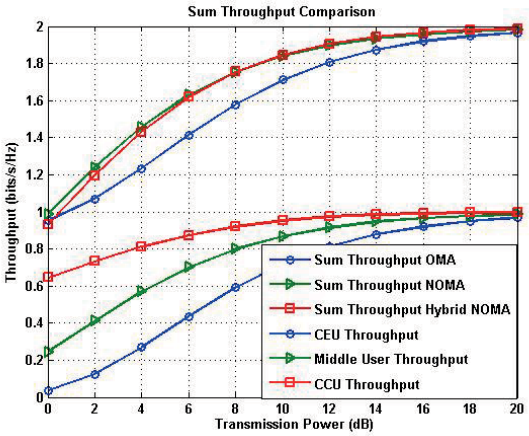

Figure 7: Throughput Comparison between proposed hybrid NOMA schemes with fixed power allocation.

Table 2: Data rate comparison between NOMA and OMA

	Distance	50m	100m	150m
NOMA	mCUE Data rate	2.2 Mbit/s	2 Mbit/s	1.8 Mbit/s
	f CUE Data rate	1.4 Mbit/s	1.2 Mbit/s	1 Mbit/s
OMA	mCUE Data rate	1.8 Mbit/s	1.5 Mbit/s	1.2 Mbit/s
	f CUE Data rate	1 Mbit/s	0.8 Mbit/s	0.4 Mbit/s

Table 2 provides various user data rate experience, which are taken into account. As the average distance increases between users, it can be observed that the performance of OMA declines linearly. Due to lower average SNR, the second and third users achieve less bits per symbol. This is a result of significant user interference. The performance steadily improves as the power ratio rises, although it is still significantly inferior to OMA.

Figure 8 shows the average EE comparison between OMA and NOMA schemes.The performance advantage over Hybrid NOMA grows as the power ratio rises. This is because Hybrid NOMA enables simultaneous access by allusers to a subcarrier. While the feasible bits/symbol for the near and far users are lowered due to the reduced average received SNR, other users' co-channel interference is also reduced.However, the poorest user's energy efficiency decreases to roughly 1.8Mbits/joule when OMA is used.We can see the superiority in attaining EE while using user-pairing scheme.

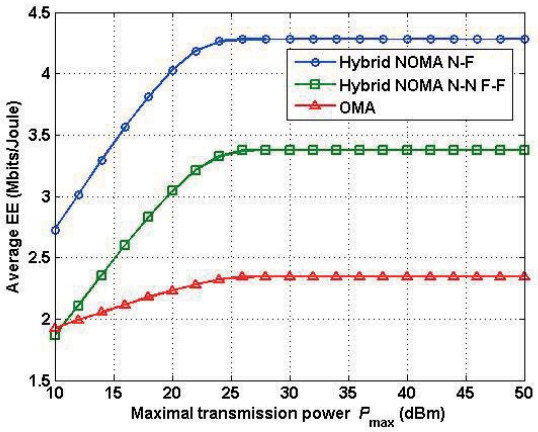

Figure 8: Average EE between proposed hybrid NOMA scheme with OMA.

5 Conclusion

Millimeter wave (mmWave) enabled Heterogeneous network (Hetnet) has offered ubiquitous connectivity with the aid of Hybrid NOMA user pairing algorithm because of the great demand. Hybrid NOMA is envisioned with superior performance with small cells enabled with mmWave environment. This proposed work outage performance is shown and offloading macro cells such as extreme changes in the required user data rate and energy efficiency.The congestion is reduced in traditional wireless networks by offloading with small cells in Hetnet. The outage performance is analyzed for the alluded users particularly in the cell edge weak users. It shows a decrease in outage probability of 90% for near users i.e cell center user (CCU) and 48% for far usersi.e cell edge user (CEU). Thereby alleviating dead zones and energy efficient support is shown for transmission using carrier sensing NOMA. A major enabler for handling the enormous number of Internet of devices that will be deployed in the factory of the future is widely recognized as being NOMA.

6 References

1. NTT DOCOMO, "5G Concept and Technologies", http:5gworkshop.hhi.fraunhofer.de/wp-content/

uploads/2020/12/Globecom-2020-WS-on-5G-New-Air-Interface-NTT-DOCOMO.pdf, December 2020.
2. B. Clerckx, Y. Mao, et al, (2021) "Is NOMA efficient in multi-antenna networks? A critical look at next generation multiple access techniques," IEEE Open Journal of the Communications Society, vol. 2, pp. 1310–1343, 2021.
3. L. Sala¨un, M. Coupechoux, and C. S. Chen, (2020) "Joint subcarrier and power allocation in NOMA: Optimal and approximate algorithms," IEEE Transactions on Signal Processing, vol. 68, pp. 2215–2230, 2020.
4. SepehrRezvani, Eduard A. Jorswieck, et al,(2021) Optimal SIC Ordering and Power Allocation in Downlink Multi-Cell NOMA Systems" IEEE Access, rXiv:2102.05015 [cs.IT]
5. O. Maraqa, A. S. Rajasekaran, S. Al-Ahmadi, H. Yanikomeroglu, and S. M. Sait, (2020) "A survey of rate-optimal power domain NOMA with enabling technologies of future wireless networks," IEEE Communications Surveys & Tutorials, vol. 22, no. 4, pp. 2192–2235, 2020.
6. Tabassum, Hina&Hossain, Ekram&Hossain, Md. (2016). Modeling and Analysis of Uplink Non-Orthogonal Multiple Access (NOMA) in Large-Scale Cellular Networks Using Poisson Cluster Processes. IEEE Transactions on Communications. PP. 10.1109/TCOMM.2017.2699180.
7. Zeng, Ming &Yadav, Animesh&Dobre, Octavia &Tsiropoulos, Georgios& Poor, H. Vincent. (2017). On the Sum Rate of MIMO-NOMA and MIMO-OMA Systems. IEEE Wireless Communications Letters. PP. 1-1. 10.1109/LWC.2017.2712149.
8. Batagelj Boštjan, Pavlovič, Leon, Naglič, Luka, Tomažič, Sašo. (2011) Convergence of fixed and mobile networks by radio over fibre technology. Inf. MIDEM, jun. 2011, Vol. 41, no. 2, pp. 144-149. http://www.midem-drustvo.si/Journal%20papers/MIDEM_41(2011)2p144.pdf.
9. S. Zhang et al., "A Dynamic Power Allocation Scheme in Power-Domain NOMA using Actor-Critic Reinforcement Learning," 2018 IEEE/CIC International Conference on Communications in China (ICCC), 2018, pp. 719-723, https://doi.org/10.1109/ICCChina.2018.8641248.
10. N. C. Luong, D. T. Hoang, S. Gong, D. Niyato, P. Wang, Y. Liang, and D. I. Kim, "Applications of deep reinforcement learning in communications and networking: A survey," IEEE Communications Surveys & Tutorials, vol. 21, no. 4, pp. 3133–3174, 4th Quarter 2019.
11. Y. Sun, J. Zhou, Q. Cao, and S. Li, "Precoder design in statistical CSI aided non-orthogonal multiple access," IEEE Access, vol. 6, pp. 16 484–16 492, Feb. 2018.
12. Y. Liu, Z. Ding, M. Elkashlan, and J. Yuan, "Non-orthogonal multiple access in large-scale underlay cognitive radio networks," IEEE Trans. Veh. Technol., vol. 65, no. 12, pp. 10 152–10 157, 2016
13. V.-D. Nguyen, H. D. Tuan, T. Q. Duong, O.-S. Shin, and H. V. Poor, "Joint fractional time allocation and beamforming for downlink multiuser MISO systems," IEEE Commun. Lett., vol. 21, no. 12, pp. 2650–2653, 2017.
14. Q. Zhang, Q. Li, and J. Qin, "Robust beamforming for nonorthogonal multiple-access systems in MISO channels," IEEE Transactions on Vehicular Technology, vol. 65, no. 12, pp. 10 231–10 236, Dec.
15. Zhang, Haijun et al. "Energy Efficient Resource Management in SWIPT Enabled Heterogeneous Networks With NOMA." IEEE Transactions on Wireless Communications 19 (2020): 835-845.
16. Samuel Amalorpava Mary Rajee and ArulrajMerline. Machine intelligence technique for blockage effects in next-generation heterogeneous networks. Radioengineering, 29(3), 2020

Arrived: 27. 06.2 022
Accepted: 23. 11. 2022

Informacije MIDEM
Journal of Microelectronics,
Electronic Components and Materials
Vol. 52, No. 4(2022), 271 – 272

Dobitnika uglednih mednarodnih nagrad
Winners of Prestigious International Awards

Profesorica dr. Barbara Malič, predsednica Društva MIDEM, in profesor dr. Marko Topič, častni predsednik Društva MIDEM, sta v letu 2022 prejela ugledni mednarodni nagradi za izjemne prispevke in vrhunske dosežke na strokovnih področjih, ki jih pokriva naše društvo.

V imenu Društva MIDEM jima iskreno čestitamo in želimo veliko novih raziskovalnih izzivov in uspehov!

prof. dr. Janez Krč
podpredsednik Društva MIDEM

Professor Dr. Barbara Malič, President of the MIDEM Society, and Professor Dr. Marko Topič, Honorary President of the MIDEM Society, received in 2022 prestigious international awards for outstanding contributions and achievements in the fields of expertise covered by our Society.

On behalf of the MIDEM Society, we congratulate them and wish them many new research challenges and successes!

Prof. Dr. Janez Krč
Vice-President of the MIDEM Society

PROF. DR. BARBARA MALIČ, DOBITNICA NAGRADE ZDRUŽENJA IEEE ZA PODROČJE FEROELEKTRIKOV


IEEE

IEEE Ultrasonics, Ferroelectrics, and Frequency Control Society

2022 IEEE Ferroelectrics Recognition Award

is presented to

Barbara Malič

For her outstanding contributions to the elucidation of the relationships between chemical and physical properties in ferroelectric ceramics

FOUNDED NEW YORK 1884

Mark Schafer
2022-2023 President
UFFC-S

Shujun Zhang
Vice President for Ferroelectrics
UFFC-S

UFFC

Vodja Odseka za elektronsko keramiko Instituta „Jožef Stefan", prof. Barbara Malič, je dobitnica nagrade IEEE Ferroelectrics Recognition Award za leto 2022, ki jo podeljuje odbor za feroelektrike pri društvu Ultrasonics, Ferroelectrics and Frequency Control Society (UFFC-S) v okviru zveze IEEE za dosežke na področju raziskav feroelektrikov. Prof. Malič je nagrado prejela za izjemen prispevek k razjasnitvi odnosov med kemijskimi in fizikalnimi lastnostmi feroelektrične keramike. V raziskavah feroelektrične keramike na osnovi svinčevih perovskitov in okolju prijaznejših alkalijskih niobatov se je posvečala razumevanju kemijskih procesov, ki potekajo med sintezo in sintranjem keramike, in so osnova za načrtovanje mikrostrukture in posledično njihovih funkcijskih lastnosti. Nagrada je veliko priznanje raziskovalnemu delu prof. Malič in potrditev odličnosti raziskav feroelektrikov, ki Odsek za elektronsko keramiko že vrsto let uvrščajo med najpomembnejše raziskovalne skupine tega področja.

PROF. DR. BARBARA MALIČ, WINNER OF THE IEEE PRIZE FOR FERROELECTRICS

Prof. Barbara Malič, head of the Electron Ceramics Department at the Jožef Stefan Institute, is the recipient of the 2022 IEEE Ferroelectrics Recognition Award, presented by the Ferroelectrics Committee of the Ultrasonics, Ferroelectrics and Frequency Control Society (UFFC-S) IEEE for achievements in the field of ferroelectrics research. Prof. Malič received the award for her outstanding contribution to elucidating the relationships between the chemical and physical properties of ferroelectric ceramics. In her research on ferroelectric ceramics based on lead perovskites and the more environmentally friendly alkali niobates, she focused on understanding the chemical processes that occur during the synthesis and sintering of the ceramics and form the basis for the design of their microstructure and consequently their functional properties. The award is a great recognition of Prof. Malič's research work and a confirmation of the excellence of ferroelectrics research, which has made the Electron Ceramics Department one of the most important research groups in this field for many years.

PROF. DR. MARKO TOPIČ, DOBITNIK EVROPSKE BECQUERELOVE NAGRADE ZA PODROČJE FOTOVOLTAIKE

Profesor dr. Marko Topič s Fakultete za elektrotehniko Univerze v Ljubljani je letošnji dobitnik prestižne evropske nagrade "European Becquerel Prize for Outstanding Merits in Photovoltaics" za izjemne prispevke na področju fotovoltaike. Ti vključujejo njegovo akademsko in znanstvenoraziskovalno delo z razvojem številnih optičnih in električnih simulatorjev ter merilnih sistemov, ki jih uporabljajo številni laboratoriji in industrija, njegovo izjemno angažiranost pri oblikovanju močne fotovoltaične skupnosti v Evropi in po svetu ter njegovo delo v vlogi predsednika Evropske tehnološke in inovacijske platforme za fotovoltaiko (ETIP-PV.eu). Profesor Topič si ves čas svojega delovanja prizadeva za spodbujanje izmenjave znanja in ljudi, podpira prisotnost industrijskega PV-sektorja v EU ter zagotavlja pomoč številnim znanstvenikom in inženirjem, dejavnim tako v akademskih krogih kot v fotovoltaični industriji. Uradna podelitev nagrade je bila na 8. svetovni konferenci o fotovoltaični pretvorbi energije (WCPEC-8) 26. septembra 2022 v Milanu.

PROF. DR. MARKO TOPIČ, WINNER OF THE EUROPEAN BECQUEREL PRIZE FOR PHOTOVOLTAICS

Professor Dr. Marko Topič from the Faculty of Electrical Engineering, University of Ljubljana, is this year's recipient of the prestigious "European Becquerel Prize for Outstanding Merits in Photovoltaics" for his exceptional contributions to the field of photovoltaics. These include his academic and research work in developing a number of optical and electrical simulators and measurement systems used by many laboratories and industries, his great commitment to building a strong community of photovoltaic researchers in Europe and worldwide, and his work as Chair of the European Technology and Innovation Platform for Photovoltaics (ETIP-PV.eu). The official award ceremony took place at the 8th World Conference on Photovoltaic Energy Conversion (WCPEC-8) on 26 th September 2022 in Milan.

Informacije MIDEM
Journal of Microelectronics,
Electronic Components and Materials
Vol. 52, No. 4(2022), 273 – 273

MIDEM 2023

58th INTERNATIONAL CONFERENCE ON MICROELECTRONICS, DEVICES AND MATERIALS WITH THE WORKSHOP ON CHEMICAL SENSORS: MATERIALS AND APPLICATIONS

September 27th – September 29th, 2023
Slovenia

Announcement and Call for Papers

Chairs:

Prof. Dr. Danjela Kuščer
Assist. Prof. Dr. Kristina Žagar Soderžnik

IMPORTANT DATES

Abstract submission deadline:
May 15, 2023

Acceptance notification:
June 26, 2023

Full paper submission deadline:
July 31, 2023

Invited and accepted papers will be published in the Conference Proceedings.

Detailed and updated information about the MIDEM Conferences, as well as for paper preparation can be found on

http://www.midem-drustvo.si//

MIDEM

GENERAL INFORMATION

The 58th International Conference on Microelectronics, Devices and Materials with the Workshop on Chemical sensors: materials and applications continues a successful tradition of the annual international conferences organised by the MIDEM Society, the Society for Microelectronics, Electronic Components and Materials. The conference will be held from **SEPTEMBER 27th – 29th, 2023**.

Topics of interest include but are not limited to:

- Chemical sensors,
- Novel monolithic and hybrid circuit processing techniques
- New device and circuit design,
- Process and device modelling,
- Semiconductor physics,
- Sensors and actuators,
- Electromechanical devices, microsystems and nanosystems,
- Nanoelectronics,
- Optoelectronics,
- Photovoltaic devices,
- Electronic materials science and technology,
- New electronic materials and applications,
- Materials characterization techniques,
- Reliability and failure analysis,
- Education in microelectronics, devices and materials.

ORGANIZER:
MIDEM Society - Society for Microelectronics, Electronic Components and Materials, Slovenia

CO-ORGANIZER:
Republic of Slovenia, Ministry of Economic Development and Technology
European Union, European Regional Development fund

CONFERENCE SPONSORS: UL FE, UL FS, IJS, IMAPS, Slovenia Chapter; IEEE, Slovenia Section

Boards of MIDEM *Society* | *Organi društva* MIDEM

MIDEM *Executive Board* | *Izvršilni odbor* MIDEM

Supervisory Board | *Nadzorni odbor*

Court of honour | *Častno razsodišče*

Informacije MIDEM
Journal of Microelectronics, Electronic Components and Materials
ISSN 0352-9045

Publisher / Založnik:
MIDEM Society / Društvo MIDEM
Society for Microelectronics, Electronic Components and Materials, Ljubljana, Slovenia
Strokovno društvo za mikroelektroniko, elektronske sestavne dele in materiale, Ljubljana, Slovenija

www.midem-drustvo.si